LASER DIRECT WRITING OF MICROCHANNELS FOR ARTIFICIAL LUNGS

by

Dong Hyuck Kam

A dissertation submitted in partial fulfillment
of the requirements for the degree of
Doctor of Philosophy
(Mechanical Engineering)
in The University of Michigan
2009

Doctoral Committee:

Professor Jyotirmoy Mazumder, Chair
Professor Joseph L. Bull
Professor Shuichi Takayama
Professor Margaret S. Wooldridge
Gyu Cheon Cho, IMRA America, INC.

To my family

ACKNOWLDEGEMENTS

First and foremost, I wish to express my deepest thanks to my advisor, Professor Jyoti Mazumder, for his inspiration, encouragement and support for my doctoral studies. His guidance throughout my entire studies enabled these works.

I appreciate my dissertation committee, Professor Joseph L. Bull, Professor Shuichi Takayama, Professor Margaret S. Wooldridge, and Dr. Gyu Cho. Their insights and critiques helped improve this dissertation.

Also, I would like to express thanks to IMRA America for all the support for femtosecond laser studies. I would like to take time to thank Dr. Lawrence Shah for all his help during the studies.

Finally, I would like to thank my sister and good friends for their constant encouragement and support. I would like to thank my parents for their unconditional love and endless support throughout my life.

TABLE OF CONTENTS

LIST OF FIGURES

LIST OF TABLES

CHAPTER I

INTRODUCTION

We will explore the application of laser micromachining for construction of artificial vascular networks for use in artificial lungs. In this chapter we have addressed background, motivations, research objectives, and dissertation outline.

1.1 BACKGROUND AND MOTIVATIONS

Currently, the only treatment for patients with end-stage lung disease is lung transplantation. However, a critical donor lung shortage limits opportunities for such transplantation. At end of 2005, 3,139 patients in the USA were recorded to be on waiting lists for lung transplantation. Of these, about 56% had waited more than 2 years [1]. Unfortunately, the current generation of lung assist devices is not adequate or efficient enough to serve as a bridge to lung transplantation or as a temporally or permanent replacement of a lung.

Extracorporeal membrane oxygenation (ECMO) [2-8] has been accepted as a standard treatment to newborn and pediatric patients with acute, reversible pulmonary failure with full respiratory support. However, its use as a bridge to recovery or transplant is considered as a contraindication due to technical complexities and associated risks. The complicated extracorporeal circuit of ECMO requires labor intensive clinical

management, large priming volume, massive anticoagulation, multiple transfusions, and is vulnerable to complications. Various types of lung-assist devices have been invented and developed as a bridge between transplant or rescue therapy and is much simpler and safer than ECMO.

Interventional lung assistance (ILA) [3, 5-11] has shown promising results in treatment of acute lung failures including acute respiratory distress syndrome (ARDS), trauma, lung infection, and airway obstruction. Such lung assist devices have low impedance and are driven by arterial pressure through an arteriovenous shunt. While the devices allow complete CO_2 removal, their oxygen supply is limited due to arterial oxygen saturation. Hence, the use of ILA as a bridge to transplant seems beneficial only when high CO_2 levels are the main concern, such as ventilation-refractroy hypercapnia [5].

Intravascular lung assist devices, such as the Hattler catheter [2, 5, 12-15], have been studied and developed as an alternative treatment of acute lung failure. This type of lung assist device is placed within the vena cava or right atrium, and the gas exchange is intrinsically limited by surface area. Currently, the devices are intended for partial respiratory support, up to 50% basal requirement; however, it is not expected to serve as long-term support or as a bridge to transplant.

Total artificial lungs (TAL) [2-5, 16-23] have been developed with goal of complete respiratory support for up to several months as a bridge to transplant or recovery. The devices are designed to have low impedance, and thus driven by the right ventricle connecting to the pulmonary circulation. The Biolung (MC3 Inc, Ann Arbor, MI) is near clinical trials. The device has demonstrated its feasibility and safety in a series of animal

tests, with a maximum of 30 days survival of sheep so far. For longer use and clinical trials, however, Biolung must improve biocompatibility and control of the coagulation.

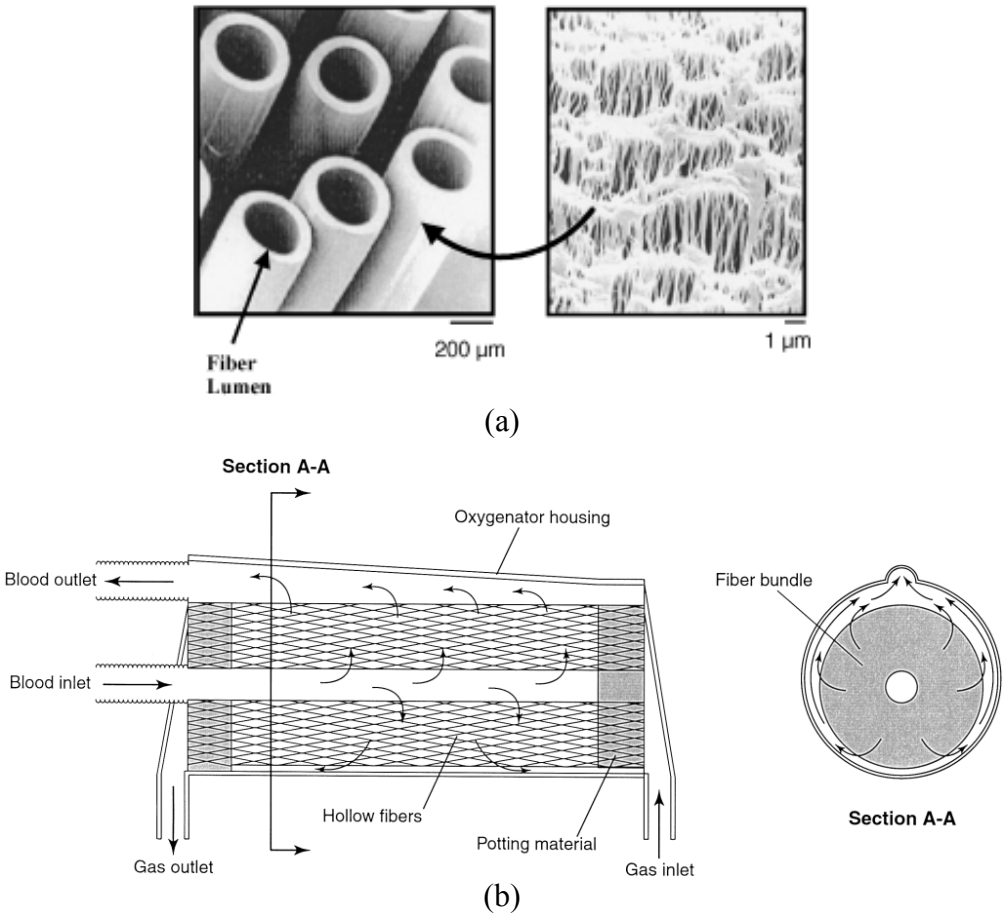

Figure 1-1: (a) Microporous hollow fiber membrane [24] (b) The Biolung prototype (MC3 Inc, Ann Arbor, MI) [2]

Current gas exchanger modules of the lung assist devices are composed of bundles of micro-porous hollow fiber membranes as shown in figure 1-1. Structurally, the inefficiency of current hollow fiber gas exchangers is attributable to their non-physiological features. Long diffusion length of the hollow fiber makes the device rather large and quality of life gets affected. Also, non-physiological flow of blood into the fiber

bundles results in high risk of blood damage and blood activation [2, 25]. Therefore, advance of the gas exchanger must be a substantial impact on artificial lung developments.

In design of gas exchanger modules, it is necessary to maximize the gas exchange efficiency while minimizing the following: flow resistance, adverse reactions of blood cells (blood activation and blood damage), and priming volume [2, 25]. However, it is challenging to balance the tradeoffs between such gas exchange requirement and hematologic / hemodynamic compatibilities [2]: shorter diffusion length or larger surface area increases gas exchange, but it also results in increase of the flow resistance and the risk of adverse reactions of blood cells including activations of inflammatory systems / coagulation.

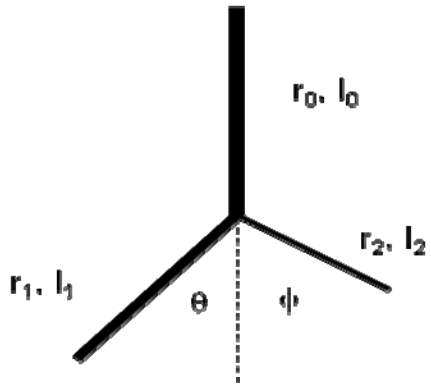

Figure 1-2: Schematic of bifurcation

1.1.1 Murray's law

The lung-like features are essential to the design of an artificial lung to enhance the gas exchange performance while maintaining the blood flow condition biocompatible. The remarkable gas exchange performance of the natural lung comes from dense

networks of micron-sized capillaries and their intimate contact with gas flows through myriads of tiny gas sacs. The tree-like branching structures in natural lung is optimized by the principle of minimum work: the transport system involves translational flow and transmural diffusion, and the work associated with flow and the diffusion is inversely proportional to the vessel size. Thus, the trade-off between the pressure drop and the diffusion distance of the blood vessel is well balanced and the blood flow evenly distributes with uniform shear stress. This optimal vascular architecture is formulated as Murray's law [26]. For a bifurcation as illustrated in Figure 1-2, Murray's law states that the radius of parent vessel (r_0) and the radius of daughter vessel (r_1 and r_2), and the branching angles (θ, ϕ) have following relationships

$$r_0^3 = r_1^3 + r_2^3 \qquad (1-1)$$

$$\cos\theta = \frac{r_0^4 + r_1^4 - r_2^4}{2r_0^2 r_1^2} \qquad (1-2\text{a})$$

$$\cos\phi = \frac{r_0^4 + r_2^4 - r_1^4}{2r_0^2 r_2^2} \qquad (1-2\text{b})$$

And human vascular networks consist of 15 branching levels, with diameters ranging from ~20 μm up to several millimeters [27].

1.1.2 Microchannel branching networks

In order to create efficient gas exchange and biocompatible blood flow condition in the gas exchanger, we seek to replicate the natural pulmonary vascular network. In this

study, multi-depth microchannel branching networks are proposed as gas exchanger to mimic the natural vascular structure. The branching networks are designed to simulate physiological blood flow for efficient gas exchange while minimizing flow resistance and adverse effect of shear stress on blood cells. The network bifurcates according to Murray's law and thus the channels become shallower and narrower at each bifurcation as illustrated in figure 1-3: blood flows along microchannels and gas transfers through a permeable membrane on top of the channels.

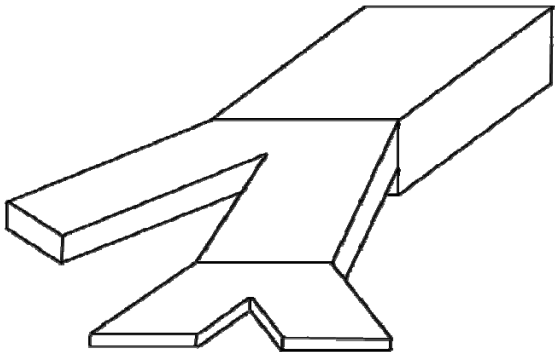

Figure 1-3: Schematic of multi-depth microchannel network

The Murray's law is derived for channels with circular cross-section. However, this principle can be applied to non-circular cross-sections using the hydraulic diameter. For channels with the near-rectangular cross-section, the aspect ratio is set to be constant. So, the characteristic length is proportional to the hydraulic diameter. Here, the depth is chosen to be the characteristic size of the channel. For the length of each branch, the ratio of the length to the characteristic size is approximately constant. In addition, all paths from inlet to outlet of the manifold are designed to have the same length to achieve the same pressure drop. By satisfying this requirement, blood flow can be evenly dispersed

into every branching channel without bubble clotting. Applying symmetric bifurcation in the branching structure, the same path length design is easily achieved. For symmetric bifurcation, $r_1 = r_2$, the Murray's law reduce to

$$r_0 = \sqrt[3]{2} r_1 = \sqrt[3]{2} r_2 \qquad (1-3)$$

$$\cos\theta = \cos\phi = \sqrt[3]{4}/2 \qquad (1-4)$$

1.1.3 Laser direct writing vs. photolithography

In the development of such microchannel branching networks, a wide range of microchannel size with reasonable surface quality and resolution is necessary to realize various designs. The current phase of our artificial lung development requires multi-level structures with depths ranging from 20 μm to several hundreds of micron. Additionally, the surface roughness should be minimized to reduce any adverse effect of the channel surface on blood cell damage / activation resulting in blood clotting or clogging [2, 25].

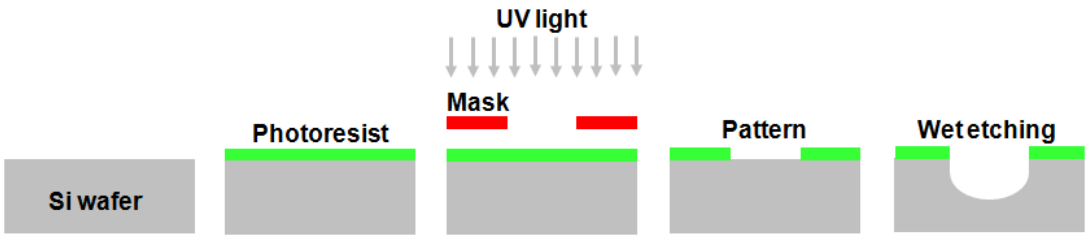

Figure 1-4: Fabrication of a microchannel with photolithography and etching

A similar concept of microchannel networks has been employed in the field of the tissue engineering. Artificial networks on biocompatible or biodegradable polymers have

been developed and studied to supply oxygen and nutrients to engineered organs such as liver, kidney and heart [28-31]. The studies on developing artificial networks have used photolithography and etching based techniques, which has multi-step procedures as illustrated in figure 1-4. However, the lithographic techniques generally limit their designs of microchannel networks to single-depth planar geometries. The uniform depth of the microchannels results in non-physiological flow patterns and high flow resistance. It is possible to build multi-depth networks using the lithographic techniques; however, the mask based lithographic techniques are inefficient in terms of cost and time in development of such microchannel networks, and it is difficult to lithographically vary the depth of such multi-depth structures. Therefore, the microfabrication techniques based on photolithography and etching are not well suited for development and production of multi-depth branching networks as gas exchangers for artificial lungs.

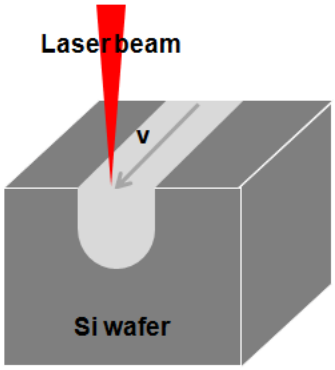

Figure 1-5: Laser direct writing of a microchannel into silicon wafer. V: the scan speed

Alternatively, the microchannel branching networks can be fabricated with laser direct writing. Figure 1-5 illustrates the laser direct writing of a microchannel into silicon

wafer. The laser technique has advantages over the photolithography and etching techniques in the development of such microfluidic structures; the maskless laser process provides simple, fast, and inexpensive solutions to the mask based photolithography technique; flexibility of laser direct writing facilitates creating a multi-depth structure of the branching network; and redesign is easy with programmable motion stage. Therefore, in this study, the multi-depth networks are fabricated on to silicon with laser direct writing.

Silicon wafer is chosen as target substrate because of its utility and versatility in bio-technology as well as the semiconductor industry. Thus, laser machined silicon structures can be compatible with well established processing techniques of silicon wafers. Actual microchannels are created from polydimethylsiloxane (PDMS) using the laser machined silicon as molds. PDMS is one of most commonly used materials in the fabrication of microfluidic devices because it is optically transparent, non-toxic, gas-permeable, and electrically and thermally insulating [32]. The procedure of molding PDMS onto microchannels is described in chapter 4.2.

Depending on the materials to be fabricated and desired applications, a variety of lasers, from nanosecond lasers to femtosecond lasers or from IR lasers to UV lasers [33-39], can be used for the laser direct writing. Here, a nanosecond IR laser and a femtosecond IR laser are studied in the fabrication of microchannels onto silicon wafer.

1.1.4 Nanosecond ablation

Creating wide range of microchannel depth with reasonable surface quality is challenging in IR nanosecond ablation of silicon because strong thermal reaction to the intense laser pulses causes surface roughness. In the study of nanosecond ablation,

methods in improving the quality of nanosecond laser ablated silicon surfaces are presented. And influences of operating parameters, such as the pulse energy, the focal position, the transverse speed, and the number of passes, on the depth and the surface morphology of micro-channels are investigated. Then, combination of laser processing parameters is optimized to create wide range of microchannel sizes with reasonable surface quality.

1.1.5 Femtosecond ablation

Femtosecond lasers have proven to be more precise than nanosecond lasers because the pulse duration is smaller than the characteristic thermalization time and thus related thermal effects are minimized [41-43]. The machined quality and the resolution of such ultrashort laser pulses have been proven in many “proof of concept” demonstrations [35-38, 41-43]. Due to their relatively high cost, however, the low productivity of fs pulses has limited its contribution in practical applications. In the majority of applications including, macroscopic material removal as well as microscopic precision is required. In the femtosecond study, investigations on the effect of transverse speed, number of passes, average power, and focal position are conducted to achieve wide range of microchannel size with reasonable surface quality. In parallel with the experiments, a numerical model for simulating femtosecond laser interaction with silicon is developed. The energy transport in femtosecond laser material interaction includes two characteristic mechanisms: free electron generation and electron-phonon interaction before thermal equilibrium. Modeling of the mechanisms has been well established individually. So, in this study, we will integrate models and discuss the simulation results.

1.1.6 Characterization of microchannels

Blood flow and gas exchange in microchannel branching networks are characterized by both experiments and numerical simulations. In vitro test, the concept of the gas exchanger composed of microchannel is demonstrated. Numerical simulations are conducted to demonstrate the benefit of multi-depth branching structures designed using Murray's law.

1.2 RESEARCH OBJECTIVES

The overarching goal of the research is to develop fundamental understanding and methodologies for Total Implantable Lungs to improve the quality of life for people with lungs disease. The specific objectives of this study are to (a) develop laser direct writing as a fabrication tool in the development of gas exchnagers for artificial lungs, (b) demonstrate the utility of the laser technique for fabricating various microchannel networks, (c) understand the important processing physics of femtosecond ablation of silicon, (d) test the performance of microchannel networks as gas exchangers and (e) demonstrate the benefit of biological principles applied to the gas exchangers. The proposed tasks can be summarized as follows:

1) **Improve the quality of laser ablation of silicon**: A chemical wet etching in a mixture of HF and HNO_3 solution is introduced as post process to clean up the debris buildup during laser ablation of silicon. The improvement of laser machined surface is illustrated. And the effect of etching time on channel depth and surface roughness is quantified.

2) **Determine the optimal conditions of laser processing to realize various designs of blood oxygenators in artificial lung development**: Achieving the necessary feature depth with rapid processing speed and sufficient surface smoothness requires efficient energy transfer from laser to target. The laser energy transfer can be manipulated with processing parameters. Thus, for both nanosecond and femtosecond ablations, optimal combinations of the processing parameters need to be determined to reduce the processing time, to expand the machining range, and to improve the surface quality.

3) **Understand the femtosecond laser-silicon interaction**: The free electron generation followed by the thermalization process is characterized in a numerical modeling of femtosecond laser interaction with silicon. The energy transport in femtosecond laser material interaction includes two characteristic mechanisms: free electron generation and electron-phonon interaction before thermal equilibrium.

4) **Characterization of laser machined microchannel networks and validation of biological principle used in the network design:** In vitro blood flow / oxygen transfer in microchannel networks are tested. And numerical simulations are carried out to demonstrate the benefit of multi-depth branching structures following Murray's law. In the simulation, the shear thinning non-Newtonian characteristic of the blood viscosity and the oxygen-hemoglobin binding are taken into account.

1.3 DISSERTATION OUTLINE

The remainder of this dissertation is divided into three chapters. In Chapter 2, IR nanosecond ablation of silicon is studied. A chemical wet etching as post process is

introduced to smooth the roughness due to strong thermal reaction of silicon to nanosecond pulses. In order to control the size and to make smooth surfaces for resulting structures, investigations on the effect of laser processing parameters are conducted. And combinations of the parameters are optimized to fabricate wide range of microchannel depth with reasonably smooth surface. The procedure to create multi-depth microchannel networks into silicon with nanosecond ablation followed by wet etching is explained. In Chapter 3, IR femtosecond ablation of silicon is studied. Like done in the nanosecond study, influences of operating parameters, such as the pulse energy, the focal position, the transverse speed, and the number of passes, on the depth and the surface morphology of micro-channels are investigated. To increase the processing speed and to expand the machining range, an optimal processing condition is found. As a demonstration, a 9-generational multi-depth branching network is machined into silicon with femtosecond pulses. A numerical modeling of the femtosecond pulse interaction with silicon is carried out to understand the physical processes involved in femtoescond ablation of silicon. In Chapter 4, the blood flow and the oxygen transfer in the microchannel networks are characterized with both experiments and numerical simulations. The numerical simulations are focused on to demonstrate the benefit of Murray's law applied to gas exchangers.

CHAPTER II

NANOSECOND PULSED ABLATION

2.1 INTRODUCTION

This chapter describes laser direct writing of multi-depth microchannel branching networks into silicon wafer using infrared (IR) nanosecond laser. A variety of lasers can be used for fabrication of microfluidic structures: from nanosecond lasers to ultrashort (femtosecond or picoseconds) lasers as well as from IR lasers to ultraviolet (UV) lasers, depending on the materials to be fabricated and desired applications [33-40]. Although the use of ultrashort pulse lasers or UV lasers is known to be more adequate for micromachining than IR nanosecond lasers due to minimal peripheral thermal damage and associated debris [36-38, 41-43], IR nanosecond lasers remain more commonly available. Therefore, it is useful to develop a process to fabricate microfluidic structures into silicon with IR nanosecond laser pulses. In addition, silicon wafer used as a target substrate in present study is known as a difficult material to fabricate in laser machining. Several different strategies are used to fabricate silicon structures. Femtosecond or UV lasers have most commonly been used for fabricating silicon structures [44-46]. Otherwise, chlorine-assisted laser ablation of silicon has been reported [47]. However, femtosecond lasers have been reported to have relatively low productivity compared with their related costs, although they improve machined surface quality and resolution

significantly. UV lasers require specially designed optics and expensive maintenance with less reliability. Chlorine-assisted laser machining needs a complicated chlorine gas circulating system. Therefore, direct laser writing of silicon using a commonly available IR nanosecond laser would have significant advantage.

Nanosecond laser ablation of silicon presents a substantial challenge since strong thermal reaction of irradiated silicon causes significant roughness of the laser ablated surface as presented in figure 2-1. Explosive boiling for each pulse and overlap of the pulses are not only two main processes in nanosecond laser ablation, but also the two main reasons for the roughness problem. Solidified molten material and splashed debris in the craters created by the laser pulses initiates the surface roughness. And the overlapping of the pulses aggravates the surface roughness. In addition, to increase the ablation depth, more laser energy transfer to target surface is required resulting in the increase of the surface roughness.

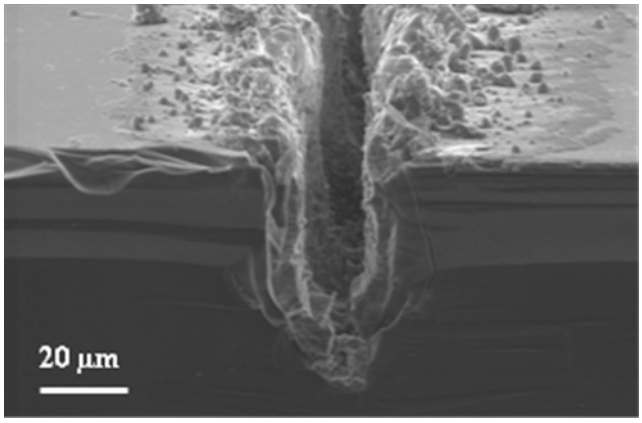

Figure 2-1: SEM image of micorchannels created by a series of 200 ns pulses with the pulse energies of 146 µJ

With the help of a chemical wet etching as post-processing [33], laser direct writing

(LDW) with IR nanosecond pulses has proven to be a useful tool to create multi-depth microfluidic structures into silicon wafer [34]. However, as shown in figure 2-2, the surface quality is not good enough for LDW's application to the development of the gas exchanger for artificial lungs. Thus, further study is required for IR nanosecond ablation of silicon.

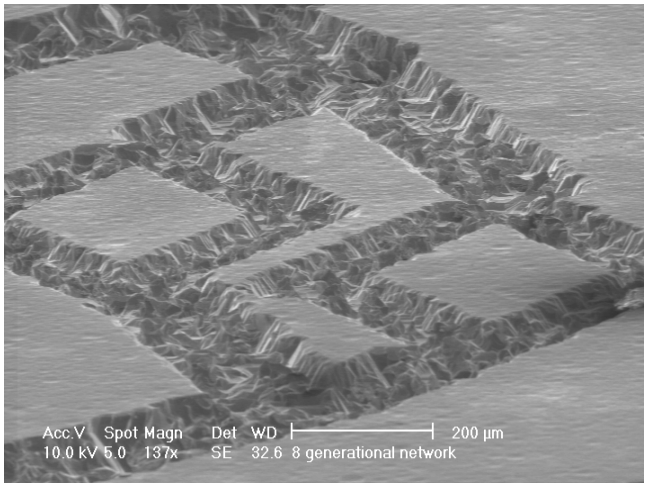

Figure 2-2: SEM image of microchannel on <100> N-type silicon created by nanosecond Nd:YAG laser followed by wet etching with 30 % KOH at 70 °C for 10 min after 40 % HF for 10 min

In this study, methods to improve the quality of nanosecond laser ablated silicon surfaces are presented. Modified assist gas, injected in a cutting direction instead of a conventional coaxial gas stream, is introduced to eject molten mass out of the microchannels (see figure 2.8). A chemical wet etching with a solution of HF and HNO_3 is applied as post processing not only to remove the debris build-up consisting of solidified molten material but also to smooth laser ablated surfaces. To control the channel depth while maintaining smooth surface, the effect of processing parameters,

such as the scan speed / the number of scan passes / the average power / the focal position / etching time, is investigated. Then, the processing parameters are optimally combined to create wide range of microchannel size with reasonable surface quality. Based on the result, combinations of laser parameters are selected to fabricate multi-depth microchannel branching networks.

2.2 EXPERIMENTAL

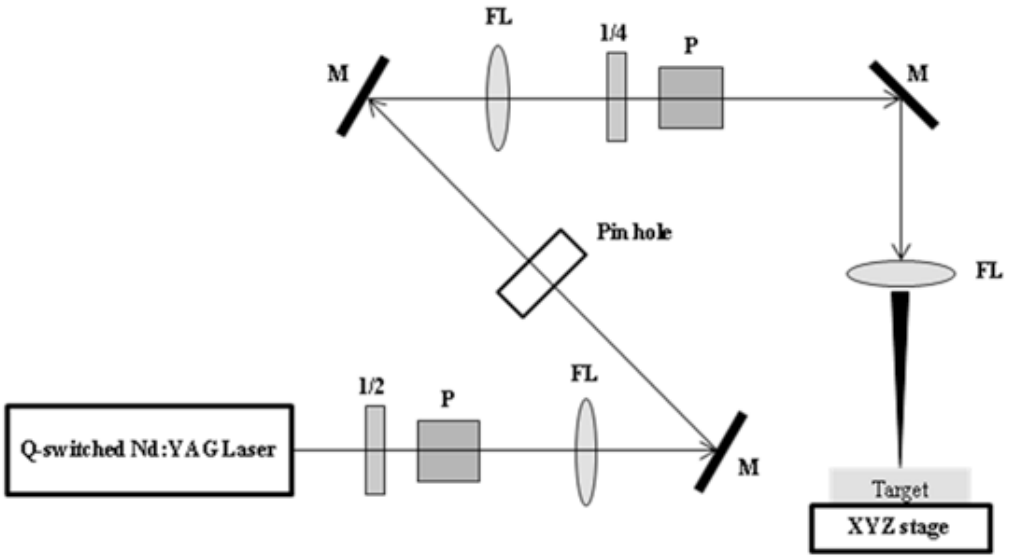

Figure 2-3: Experimental system schematic: polarizer (P), half-wave plate (1/2), quarter-wave plate (1/4), focal lens (FL), and mirror (M)

The schematic of the laser machining setup is shown in figure 2-3. A Q-switched Nd:YAG laser (TRW DP-11) operating at 1064nm is used as the nanosecond ablation laser. The laser is set to a repetition rate of 500 Hz and a pulse width of 100 μs (duty cycle of 5%). The 100 μs pulses are modulated to produce a series of 200 ns pulses with

10 μs interval as shown in figure 2-4. The average power of the incident beam on the silicon sample is controlled using a combination of a half-wave plate and a polarizer in beam delivery. A quarter-wave plate and a polarizer are used to circularly polarize the beam at target. Programmable X-Y-Z stages are used to control the position and the motion of laser beam spots.

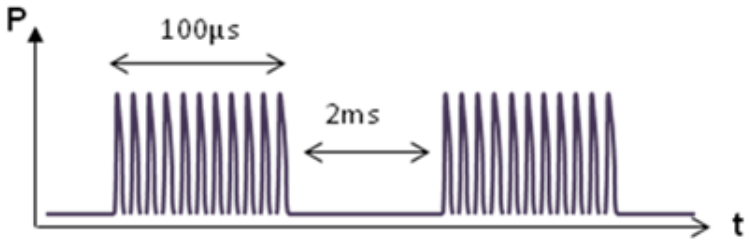

Figure 2-4: Temporal profile after modulation. 100μs pulses consist of 11 pulses with 200ns pulse width.

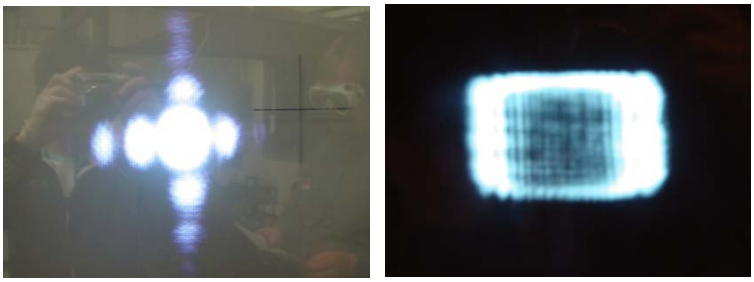

Figure 2-5: Far field and near field beam shape of TRW DP-11

2.2.1 Beam shape and spot size

Figure 2-5 shows near-field and far-field beam shape. At focus (far-field), the beam shape at a bright central spot with a symmetric diffraction is near Gaussian. A pin-hole is used to filter the diffraction spots surrounding the bright central lobe. The beam spot size of full width $1/e^2$ maximum ($FW1/e^2M$) is determined from curve fitting of power

variation with partial beam screening at focus as illustrated in figure 2-6. Integrating Gaussian intensity profile, the power measured in the power meter, *p(y)*, is written in terms of the position of the knife edge, y

$$p(y) = \int_{-\infty}^{\infty}\int_{-\infty}^{y} \frac{2P}{\pi w^2} \exp[-2\left(\frac{x^2 + y^2}{w^2}\right)]dxdy = \frac{P}{2}\left[1 + Erf(\frac{y}{w})\right] \qquad (2 - 1)$$

where P is the total power of the laser beam, w is the beam spot radius of full width $1/e^2$ maximum ($FW1/e^2M$) of Gaussian beam, and *Erf* is the error function. Using 100 mm focal length objective, 15 μm beam spot radius gives the best fit to a series of data points as presented in figure 2-7. The spatial beam profile does not change with the total power of the laser beam, so the same spot sizes are obtained for 335 and 799 mW total powers. In this measurement, the beam is used without modulation to reduce peak intensity so that it would not damage the knife edge.

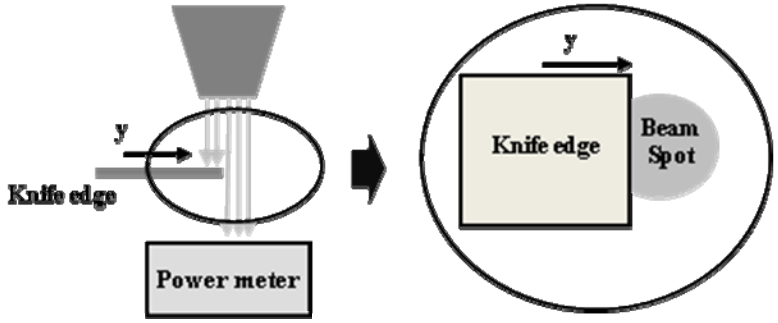

Figure 2-6: Schematic of beam spot size measurement for Gaussian beam profile using a knife edge and power meter

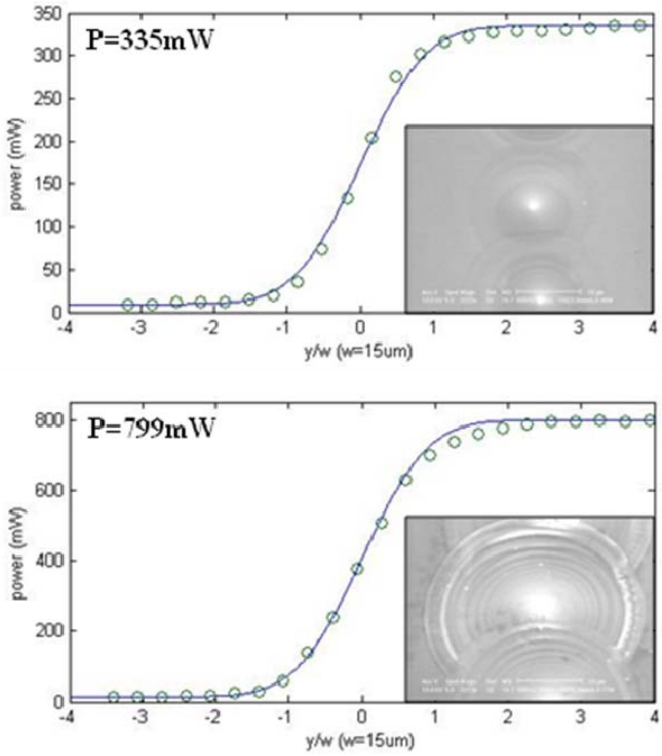

Figure 2-7: Curve fittings and SEM images of craters created by total power of 335 mW and 799 mW

2.2.2 The effect of modified assist gas

Generally, coaxial assist gas is injected in order to eject molten material and get increased penetration depth in laser cutting or drilling processes. However, silicon wafers are fragile, brittle and typically very thin, so the injection of assist gas in the coaxial direction of the nozzle is not applicable to laser machining of micro-channels on silicon wafers [33]. In this study as illustrated in figure 2-8, gas is injected in the axial direction of micro-channel at 45° from the coaxial direction in nanosecond ablation of silicon wafer. Argon gas is used to reduce the oxidization of silicon during laser ablation. Figure 2-9 shows the morphology of laser-irradiated surfaces without gas injection (a) and with

Argon gas injection (b). Both microchannels are produced with 200 ns pulses, a fluence of ~35 J/cm^2, and a scanning speed of 8 mm/s. The Argon gas injection is effective to eject molten material out of the micro-channel. The material escape in nanosecond laser ablation without assist gas relies on evaporation and splash of molten material due to explosive boiling. Thus, resulting ashes, which is cleaned before taking the SEM image in figure 2-9(a), is scattered around the ablated channel. In addition, solidification of the remaining molten material inside the channel blocks the transfer of laser energy to the target surface. Figure 2-9(c) presents material removal rate versus fluence in each process. However, material removal rate of the ablation with the gas injection is measured lower than that of another process. This is because most of ejected molten material by the gas ejection is re-solidified around the ablated channel instead of the channel interior as shown in figure 2-9(b). In other words, the hump on the edge of the ablated channel is created because the gas flow increases the cooling rate of the molten material.

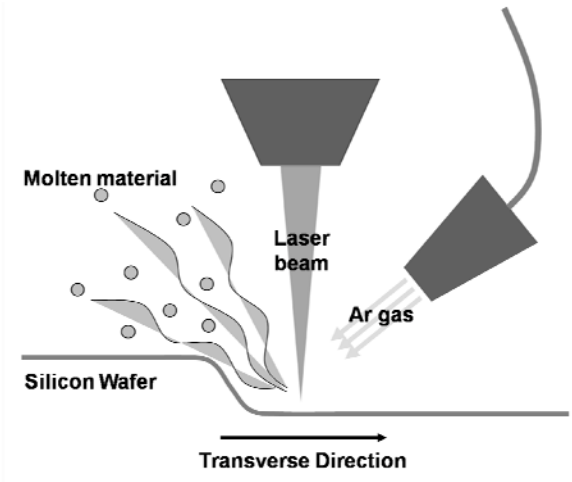

Figure 2-8: Schematic sketch to illustrate the role of argon gas injection in the axial direction of a microchannel

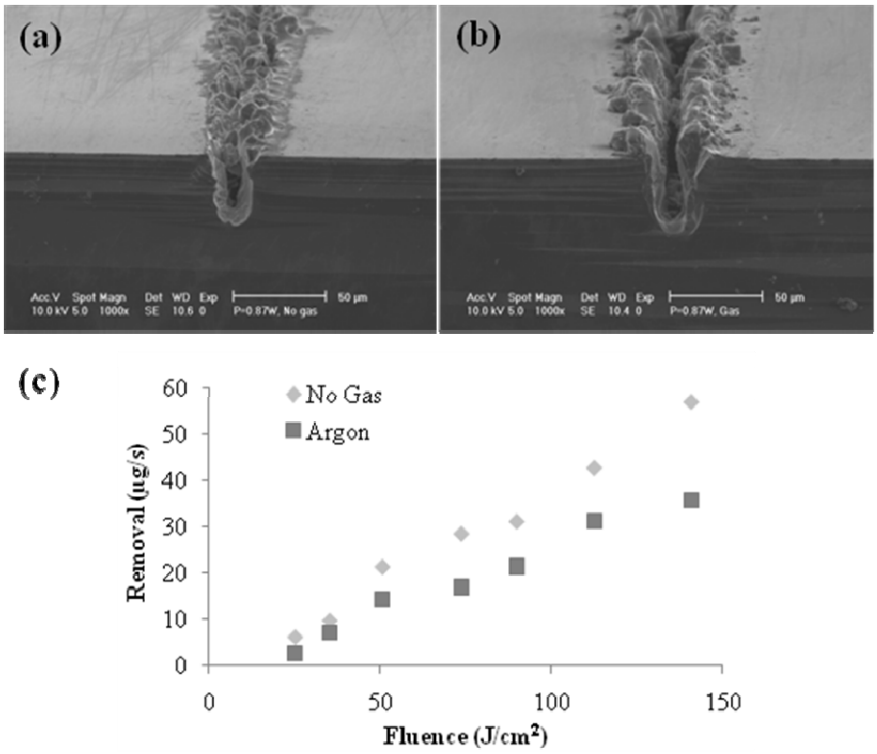

Figure 2-9: The SEM images of laser machined microchannels (a) without gas injection and (b) with Argon gas injection in axial direction. (c) The material removal rate vs. fluence in both cases. The channels were created with single pass at a speed of 8 mm/s.

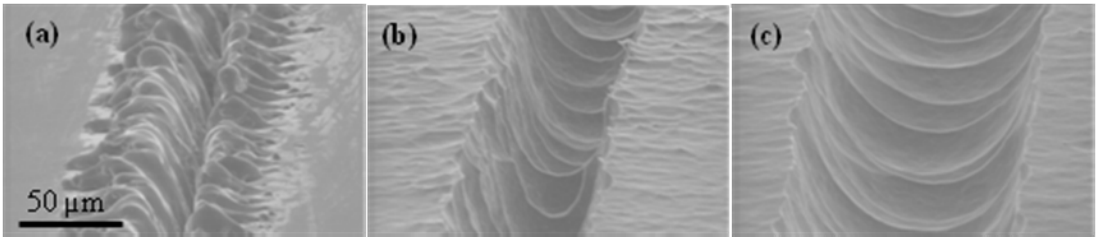

Figure 2-10: SEM images of laser machined micro channels on bare silicon wafer after chemical wet etching as a post process: (a) 30 % KOH etching for 10 min. (b) 49 % HF and 69 % HNO_3 etching for 2 min. after 30 % KOH etching for 10 min. and (c) 49 % HF and 69 % HNO_3 etching for 4 min. after 30 % KOH etching for 10 min.

2.2.3 Chemical wet etching in HF and HNO_3 solution

In order to solve the roughness problem due to the debris buildup composed of the solidified molten material, a chemical wet etching in a 49 % HF and 69 % HNO_3 solution with a ratio of 10:1 is applied after cleaning the surface with 30 % KOH for 10 min as a post processing step.

Figure 2-10 shows the change of surface morphology of a micro-channel on a bare silicon wafer with increasing etching time. After dipping the laser ablated sample in 30% KOH solution for 10 min at room temperature splashed ash and particles are removed. However, the hump of molten mass on the edge of channel is not etched at all. After further etching in the solution of 49% HF and 69% HNO3 for 2 min, as shown in the second SEM image of figure 2-10, the hump is etched out leaving good edge quality. Since the etching rate is proportional to the area in contact with the etchant, the hump having a larger surface area to volume ratio than other features disappears faster. The etching by the HF and HNO_3 solution is observed to occur in any normal direction of the surface without preference to the crystalline structure of silicon. As the etching time increases, the width of the channel increases. However, variation in the depth is insignificant because the etching occurs in the non-patterned surface outside the channel as well as the bottom of the channel. The periodic ruffling pattern on the bottom of the channel after wet etching develops because the channel is created by periodic laser pulses. The etching rate of HF and HNO3 solution decreases with time because the etchant neutralizes as it reacts with both large non-patterned large area of the silicon and the narrow laser-ablated-region. The etching rate depends on the amount of solution and total area of silicon pieces so that a qualitative profile of the temporal etching rate is not measured.

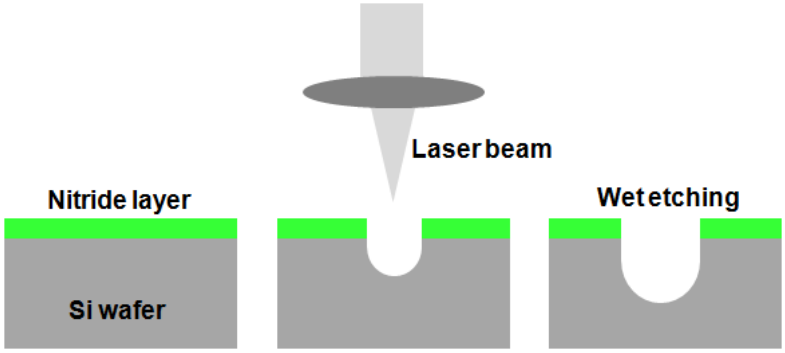

Figure 2-11: Laser ablation of nitride coated silicon wafer and wet etching

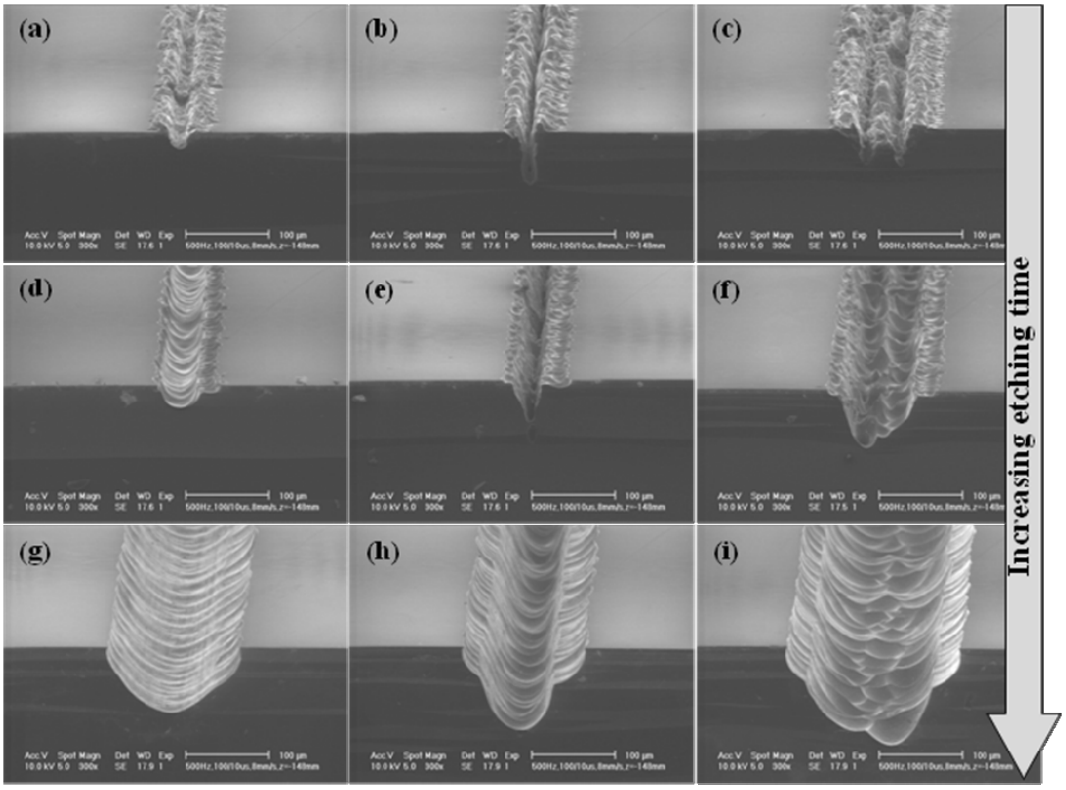

Figure 2-12: SEM images of laser machined micro channels on a nitride coated silicon wafer after chemical wet etching as a post process: (a, b, c) 30% KOH etching for 10 min. (d, e, f) 49% HF and 69% HNO3 etching for 10 sec. after 30% KOH etching for 10 min. (g, h, i) 49% HF and 69% HNO3 etching for 30sec. after 30% KOH etching for 10 min.

The roughness of the non-patterned area of bare silicon wafer after the etching process as shown in figure 2-10 (b, c) prevents the area from adhering closely to a top sealing film. Instead of the bare silicon, nitride coated silicon wafers are used to protect the non-patterned polished silicon surface from chemical etching as illustrated in figure 2-11. In addition, the chemical etching is limited to the laser ablated area so that the required amount of the hazardous etching solution is reduced. Figure 2-12 shows how the surface morphology of the micro-channels on the nitride coated silicon changes with increasing etching time. To observe how the smooth surface evolves out of the laser-machined rough surface with increasing etching time, three micro-channels with different cross-sectional shapes are created by different overlaps of the laser beam. Different initial surface profiles of the micro-channels result in different surface morphologies after the chemical etching. However, initial difference in the depth and width of the channels remains constant since the etching is applied at a same rate. The secondary etching on the edge of the micro-channels shows up because the accumulation of hot molten material on the edge of the channel destroys the nitride coating in the area. This secondary etching results in lower resolution of the micro-channel structures.

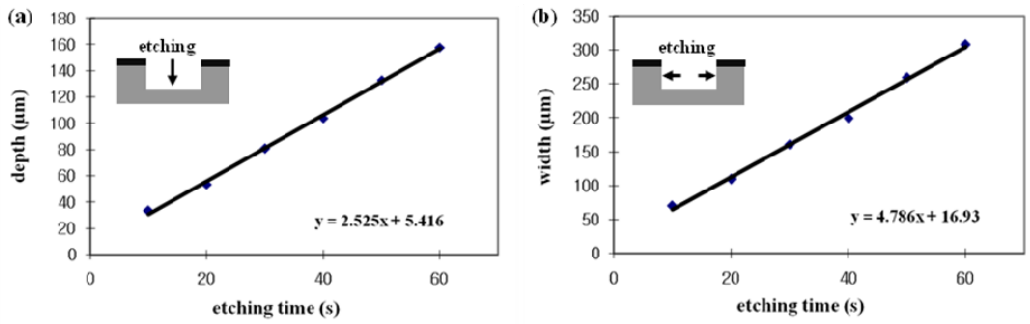

Figure 2-13: The depth (a) and the width (b) of a microchannel on nitride coated silicon wafer vs. etching time.

Figure 2-13 shows the dependence of channel depth and width on the etching time. The etching rate of the width of channels is about twice of that of the depth as etching occurs in the two opposite wall directions of a channel. In the graphs of figure 2-13, initial width and depth is not measured because it is difficult to define the boundary of the channels without etching.

2.3 PROCESSING PARAMETER OPTIMIZATION

The surface quality of nanosecond ablated microchannel on silicon is much improved with the chemical etching as post process. Thus, IR nanosecond pulses become more applicable in fabrication of microchannels into silicon. However, further study is required for the nanosecond pulses to be used in development of branching vascular networks for artificial lungs. In the development, the main issue is how to create a wide range of feature sizes with reasonable surface smoothness. In order to control the size and to make smooth surfaces for resulting structures, investigations on the effect of processing parameters, such as the scan speed / the number of scan passes / the average power / the focal position / the etching time, are carried out. Then, processing conditions are optimized and applied to fabricate multi-depth mcrochannel networks. Finally, 7-, 9- and 11-level branching networks are fabricated with the nanosecond ablation. For this study, microchannels are machined into nitride coated silicon wafer with multiple parallel scans with 20 μm pitch as illustrated in figure 2-14. As mentioned in Chapter 2.2.3, the laser machined microchannels are etched in a solution of HF and HNO_3 as post-process. From now on, the laser ablation depth will be referred as the depth created by laser ablation only, and the channel depth will be referred as the depth of the channel created

with the laser ablation and the acid etching.

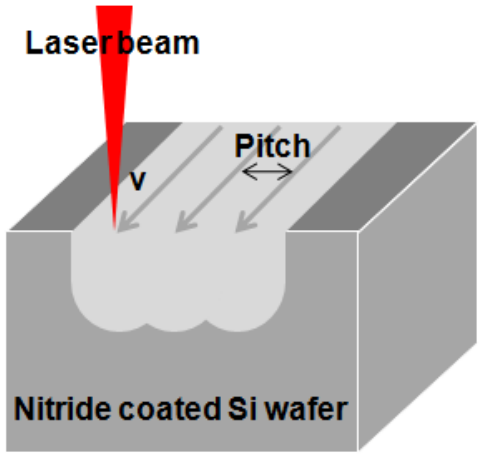

Figure 2-14: Laser ablation of nitride coated silicon wafer with multiple parallel scan. V is the scan speed and pitch is the distance between each scan line

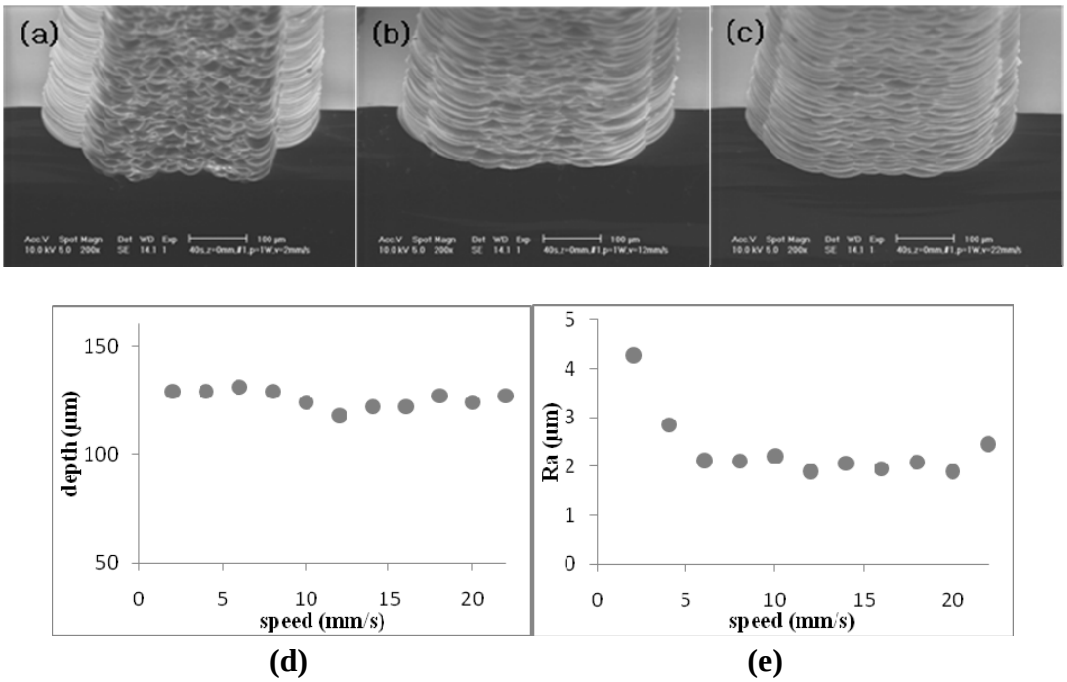

Figure 2-15: SEM images of laser machined microchannels with (a) 2 mm/s, (b) 12, and (c) 22 mm/s scan speed. Depth (d) and surface roughness, Ra (e) of laser ablation in terms of scanning speed. Operating parameters: 200ns pulse width, 1W average power, single pass, 0.5mm defocus below surface, 30µm focal spot size, and 40s chemical etching.

2.3.1 Influence of the scanning speed

Figure 2-15 shows the variation of microchannel depth and average surface roughness with the scan speed. While the ablation depth does not change much with the scan speed, the surface quality of channel can vary with the scan speed. Solidified molten material and splashed debris in the craters created by laser pulses initiates the surface roughness. And the overlapping of the pulses aggravates the surface roughness. Appropriate choice of the scan speed is important to make a smooth surface because the scan speed in pulsed laser ablation determines the overlap of the craters.

2.3.2 Influence of average power

Figure 2-16(d) shows the dependence of the channel depth on the average power. The channel depth almost linearly increases with the average power. So, the average power (or pulse energy) can be an effective parameter to control the depth of microchannel. In addition, our Nd:YAG laser provides unlimited power output with excellent beam quality (1.3-1.7X diffraction limit) from a micromachining point of view and the average power can be varied continuously by a beam attenuator. However, the surface roughness as well as the channel depth increases with increasing average power as shown in figure 2-16(e). More pulse energy is required to penetrate deeper into the silicon sample, thus stronger thermal reaction of irradiated silicon causes more roughness of the laser ablated surface. Abrupt changes of the roughness round 0.7 and 2.25 W in the plot of figure 2-16(e) are observed. At power just over the ablation threshold, only the surface nitride layer is removed. In this area a microchannel is created only by chemical etching, so the thermal effect is minimized to create smooth surface. Between 0.5 and 0.7 W, the incident beam starts penetrating into silicon surface and thus thermal damage

occurs in irradiated silicon. So, this adds the surface roughness. With more than ~2W average power, redeposit of molten material onto the ablated surface becomes noticeable. As a result, the recast silicon on the channel surface increases the surface roughness shifting the curve in figure 2-16(e) upward.

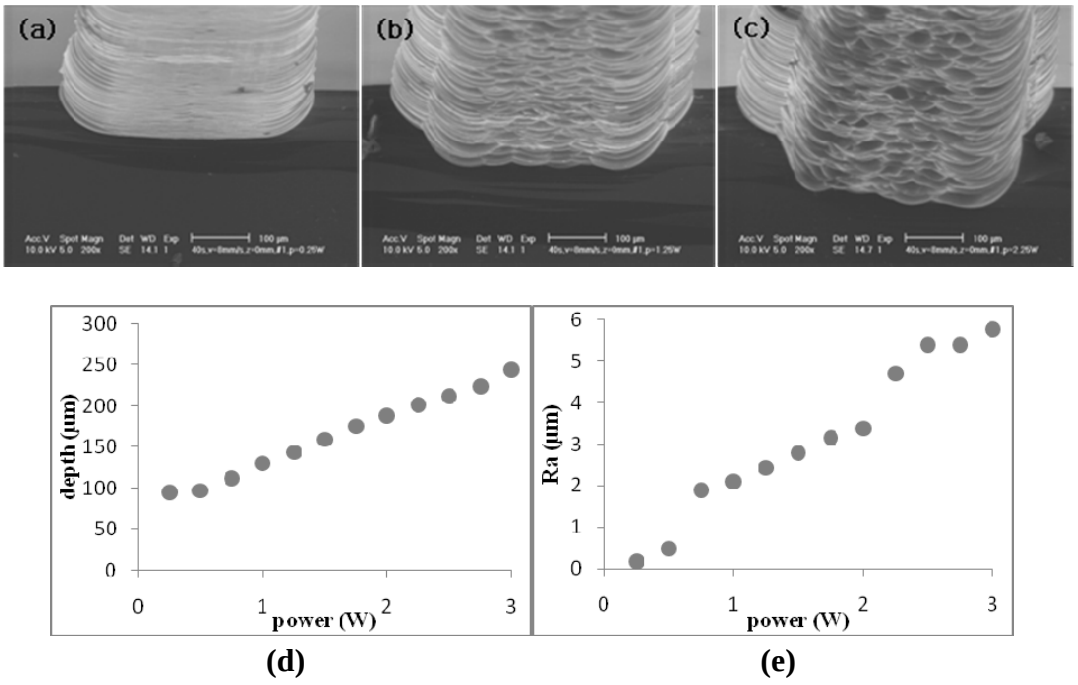

Figure 2-16: SEM images of laser machined microchannels with (a) 0.25 W, (b) 1.25 W, and (c) 2.25 W average power. Depth (d) and surface roughness, Ra (e) of laser ablation in terms of average power. Operating parameters: 200 ns pulse width, 1064 nm wavelength, 8 mm/s scanning speed, single pass, 0.5 mm defocus below surface, and 30 µm focal spot size. Depth and surface roughness are measured after 40 s chemical etching.

2.3.3 Influence of focal position

Focal position is also a parameter that affects the channel depth and the surface roughness. Defocusing attenuates beam intensity on the target resulting in shallower channel depths than that at focus as shown in figure 2-17. Increased beam intensity produces deeper channels with correspondingly rougher surface. But the focal position is

not so maneuverable as the average power because the beam has multi-mode profile as presented in figure 2-5. An acceptable focal range that has near-Gaussian intensity profile is about 1.5 mm below and above focus. As the beam shift out of the focal range, intensity profile becomes distorted resulting in irregular intensity distribution. So, the range of channel depth variation with the focal position is narrower than that of the average power variation. The focal position control does not show much merit compared to the power control and the number of passes control as seen in figure 2-17(d). For the multi-mode beam such as this laser, the beam shape and the intensity at target changes with the focal position. Thus, it is difficult to precisely control the depth with the focal position.

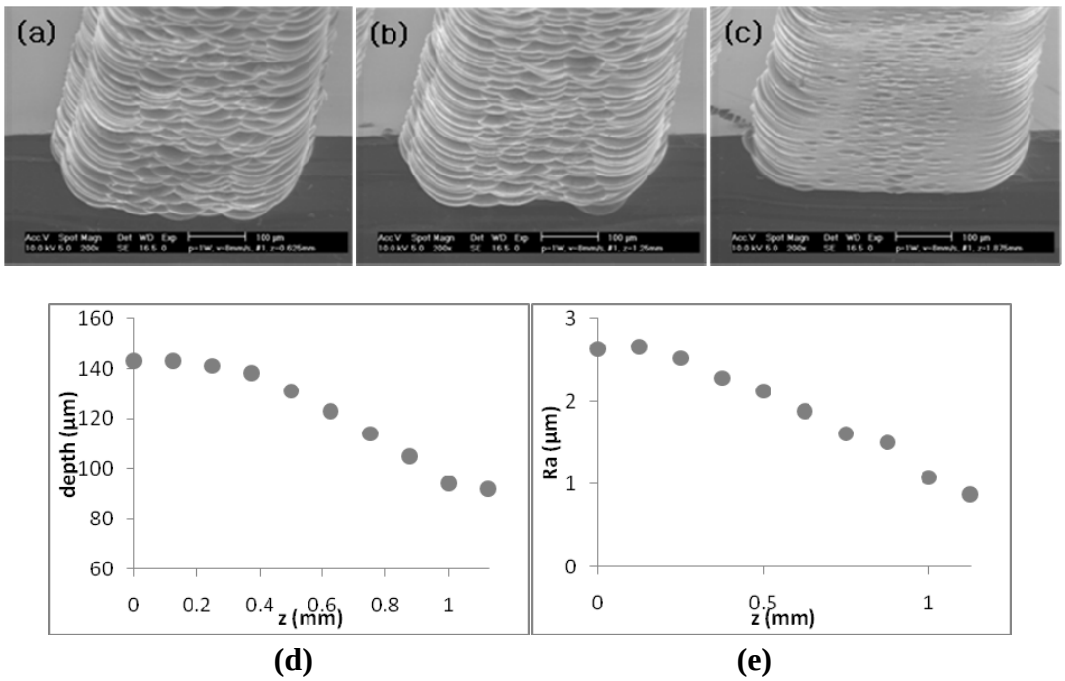

Figure 2-17: SEM images of laser machined microchannels at (a) focus, (b) 0.6 mm and (c) 1.2 mm defocus below the surface. Depth (d) and surface roughness, Ra (e) of laser ablation in terms of focal position below the surface. Operating parameters: 200 ns pulse width, 1064 nm wavelength, 1 W average power, 8 mm/s scanning speed, single pass, and 30 µm focal spot size. Depth and surface roughness are measured after 40 s chemical etching.

2.3.4 Influence of the number of scan passes

The number of scan passes refers to the number of scanned layers, which are multiple parallel passes as depicted in figure 2-14. This parameter is also one of effective parameters for control depth because of the linear dependence of channel depth on the number of scan passes as shown in figure 2-18. The microchannel surface gets rough as the number of passes increases because the overlapping of the pulses aggravates the surface roughness.

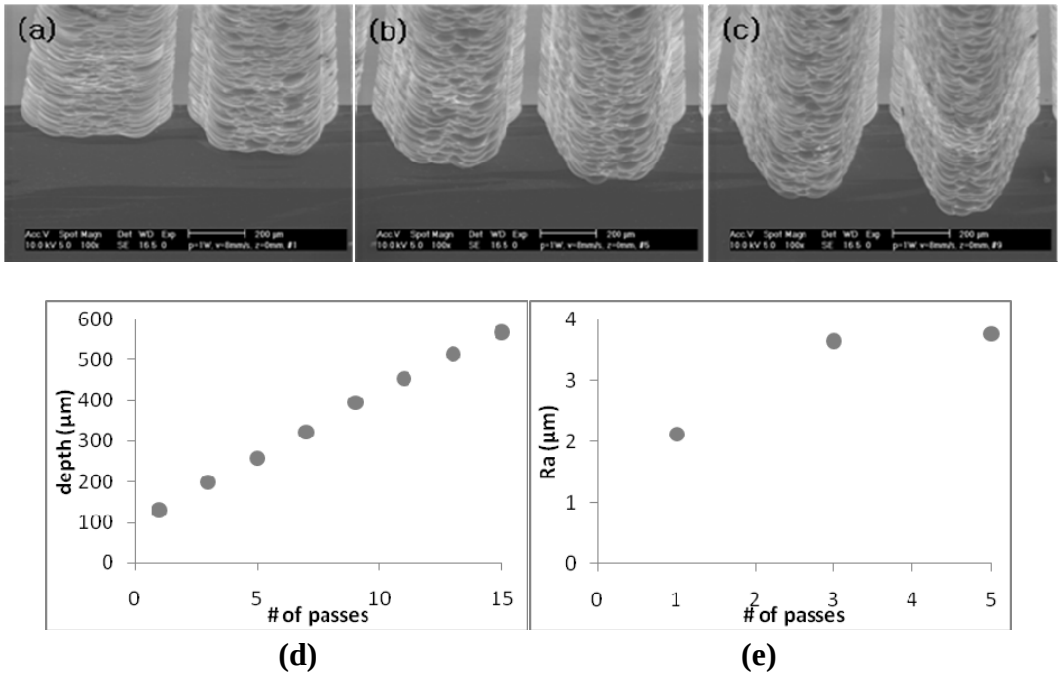

Figure 2-18: SEM images of laser ablated channels on silicon wafer after 40 s chemical wet etching. The numbers of passes in depth direction were 1, 3, 5, 7, 9, and 11 from left. All channels were machined with an average power of 1 W at focus. Depth (a) and surface roughness, Ra (b) of laser ablation in terms of the number of passes. Operating parameters: 200 ns pulse width, 1064 nm wavelength, 1 W average power, 8 mm/s scanning speed, 0.5 mm defocus below surface, and 30 µm focal spot size. Depth and surface roughness are measured after 40 s chemical etching.

For the depth control with the number of scan passes, a high repetition rate laser and a high speed scanning system are required for a precision machining with a reasonable productivity. This is because the scan speed is limited to prevent discontinuity of the channel in low repetition pulsed laser ablation. For instance, as shown in figure 2-18(d), a single pass with 1W average power generates about 60 μm depth; however, such depth resolution is not high enough to control the depth. To increase depth resolutions, power needs to be reduced. On the other hand, less power results in more number of passes. Thus, the fabrication time is further increased by the minimized pulse energy required for a precise depth control with the number of passes. To save the processing time, the scan speed needs to be increased. With the low repetition rate, however, the scan speed is limited to prevent discontinuity of the channel. As a result, with the current low repetition rate of 500 Hz, the number of passes should be minimized to save the processing time.

2.3.5 Optimal combination of parameters

In development of multi-depth microchannel branching networks, a wide range of microchannel sizes with reasonably smooth surface is necessary to realize various designs. However, it is challenging to meet such requirements because the laser ablated microchannel surface becomes rougher as the depth increases. In the nanosecond pulsed IR laser ablation of silicon wafers, a large part of the surface roughness comes from a strong thermal reaction of irradiated silicon. In order to obtain deeper channel, more laser thermal energy must be delivered to the target surface. Consequently, deeper channels accompany rougher surfaces.

Despite such dependence of surface roughness on ablation depth, use of optimal processing parameters can minimize the surface roughness while channel depth is

manipulated. The processing parameters decide the nature of laser energy transfer to target surface as described in previous sections. The delivered laser energy is increased by increasing the average power or the number of passes. For the same amount of pulse energy, the peak intensity in the spatial beam profile increases with focusing. As the scanning speed decreases, the distance between pulse to pulse gets close so that the time of laser energy delivery to target increases.

To simplify design of experiments, we need to understand the physical meaning of these processing parameters in the pulsed laser ablation. The microchannel is created by series of parallel laser pulses. In this process, the average power and the focal position determine the pulse shape, and the scan speed determines the overlap of pulses. The number of scan passes is the repetition of such processes. So, the geometry of a crater created by single pulse is determined by the average power and the focal position and the surface roughness can be minimized by manipulating the arrangement of the craters with the scan speed. The number of scan passes is just minimized to save the processing time because of the low repetition rate of the laser used.

Table 2-1: The range of laser parameters

Parameter	Sampling points
Average power, p (W)	0.5, 1.0, 1.5, 2.0 and 2.5
Focal position, z (mm)	0.0 (focus), 0.5 and1.0
Scan speed, v (mm/s)	4, 8, 12, … , 40
Number of scan passes, N	1

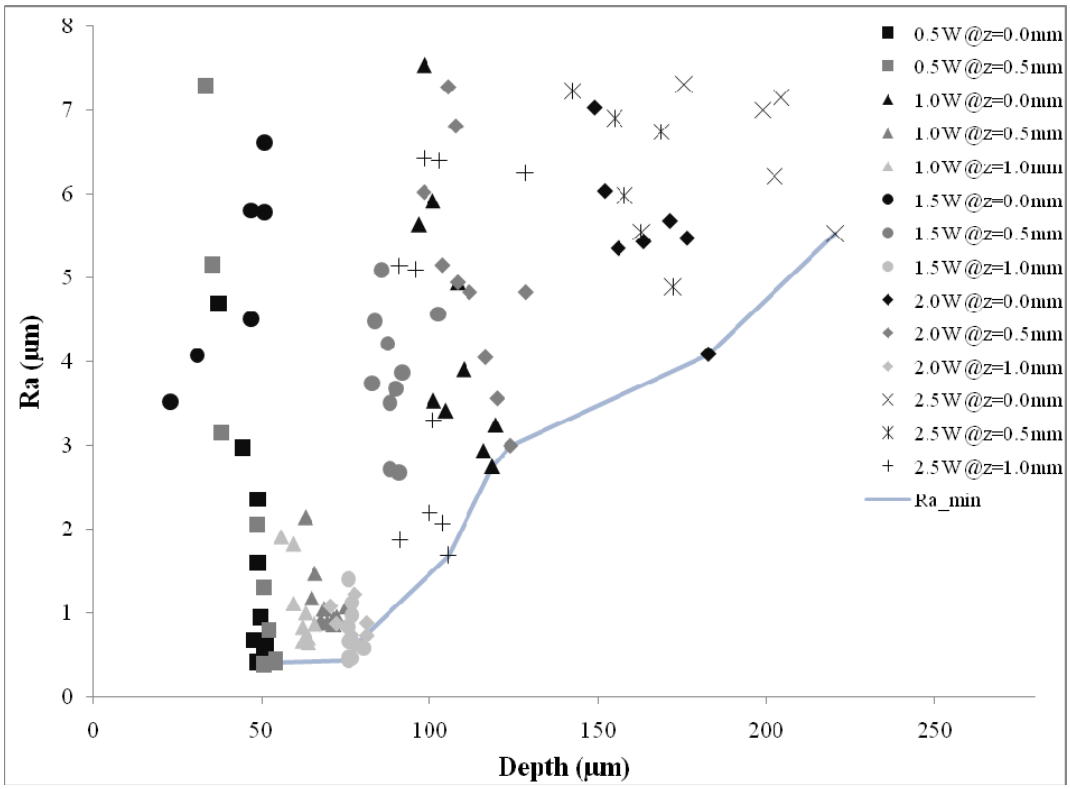

Figure 2-19: Average surface roughness, Ra of laser ablated micro-channels in terms of the channel depth. Depth and surface roughness are measured after 33 s chemical etching.

To evaluate combined effects of the processing parameters, dependent variables (channel depth and surface roughness) are measured for factorial combinations of main independent variables (average power, focal position and scan speed). The scan speed is varied from 4 to 40 mm/s for 15 different combinations of the average power and the focal position as given in table 2-1. The results are presented in figure 2-19. The corresponding roughness is shown for different channel depth using various combinations of average power, focal position and scan speed. The variations of average power are indicated by the shape of points and the variations of focal positions are indicated by contrast. The multiple points represent various scan speeds. It is observed to be effective

in controlling the channel depth by varying the combination of the average power and the focal position. While the effect of the scan speed on channel depth is found to be negligible, the surface roughness of channel can be minimized with appropriate choice of scan speeds. For the power and focal range used here, the speed ranging from 8 – 16 mm/s provides smooth surface. In figure 2-19, a line is drawn along the points, which have the minimum average roughness (Ra) for each depth. From the line, it can be shown that the surface roughness increases with increasing depth.

2.3.6 Etching time

Together with laser processing parameters, the time of the chemical wet etching as post processing is also a critical parameter to determine the depth and the surface roughness of laser machined micro-channels. Figure 2-20 shows surface roughness measurements as a function of channel depth with different acid-etching times: 20, 30 and 40 s. Detailed etching rate is presented in figure 2-13. The depth of channel is varied by manipulating the average power with constant scan speed of 8 mm/s. As the etching time increases, the channel surface gets smooth and thus the acceptable machining range with a reasonable surface roughness expands. At the same time, however, the minimum channel size increases with etching time: the minimum depths corresponding to 20, 30 and 40 s etching are ~20, ~30 and ~50 μm respectively. Here, the surface roughness is observed to decrease near the minimum depth. This is because the crater size created around the threshold fluence is not big enough to have a proper overlap of the craters with 8 mm/s scan speed. Thus, the surface quality around the minimum depth in this plot can be improved with decreasing the scan speed to have sufficient overlap of each crater.

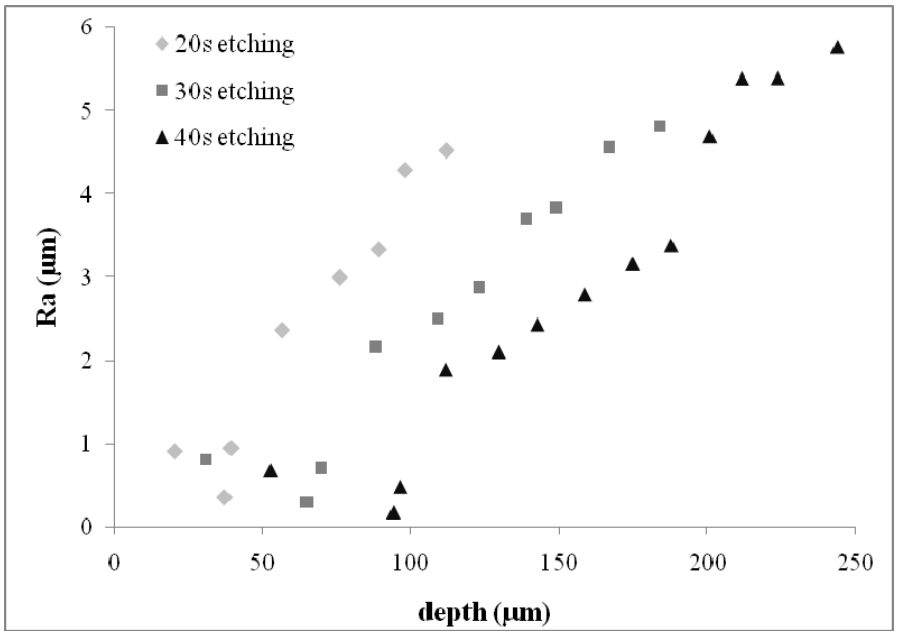

Figure 2-20: Average roughness, Ra vs. ablation depth after 20s, 30s and 40s chemical etching. The samples are prepared with the same processing parameters except the etching time as post processing.

2.4 LASER FABRICATION OF MULTI-DEPTH MICROCHANNEL BRANCHING NETWORK

To control the depth of each generation of the branching networks, the average power, the focal position, the number of scan passes are manipulated with constant scan speed of 8mm/s, which generally minimizes the surface roughness as mentioned in Chapter 2.3.5. The combination of processing parameters for a desired depth is chosen by interpolating the parameter test results presented in Chapter 2.3. For wide channels, multiple parallel scans are machined with 20 µm pitch. The etching time is selected as time it takes for the threshold depth, which has zero ablation depth because only the nitride layer is removed by laser ablation, to be etched into minimal depth in the designed networks. Then the other laser parameters are varied to achieve different corresponding channel depth using the same etching time.

7-, 9- and 11-level branching networks are laser machined into nitride coated silicon wafer with the nanosecond laser as shown in figure 2-21, 2-22 and 2-23. The depth of each generation of the networks and corresponding combinations of processing parameters are summarized in table 2-2, 2-3 and 2-4.

When the surface roughness is managed below ~3.5μm Ra, the 11-level network is created with two steps laser ablation for two steps chemical etching. In figure 2-16, an acceptable depth range with Ra less than 3.5μm after 20s chemical etching is from ~20 to ~80μm. To expand the acceptable depth range, the etching time must be increased. However, increasing etching time results in grow of the minimum channel depth. In the creation of the channel with a minimum depth, only the surface nitride layer is removed by laser ablation and then a channel is created by chemical etching. Thus, two steps chemical etching is applied to achieve channel depths from 20 to 200μm maintaining the surface roughness below ~3.5μm Ra. For example, first, channel depths from 50 to 200μm (1st – 7th generations) are laser ablated and then chemically etched for 20s. After an alignment of this silicon sample, the rest of channels (8th – 11th generations) are created and then chemically etched for another 20s. In short, channels with depth of 50 - 200 μm experience total 40s etching and channels with depth of less than 50 μm experience 20 s etching as summarized in table 2-4.

Table 2-2: The depths of each generation of 7-level branching network and processing parameters. The scan speed is 8 mm/s. Average power, p, focal position, z, and number of scan passes, N.

Generation	Depth (μm)	Parameters			
		p (W)	z (mm)	N	etching (s)
1st	400	3.04	0	2	60
2nd	320	2.25	0	2	60
3rd	250	3.04	0	1	60
4th	200	1.83	0	1	60
5th	160	1.21	0	1	60
6th	130	0.86	0	1	60
7th	100	0.86	2	1	60

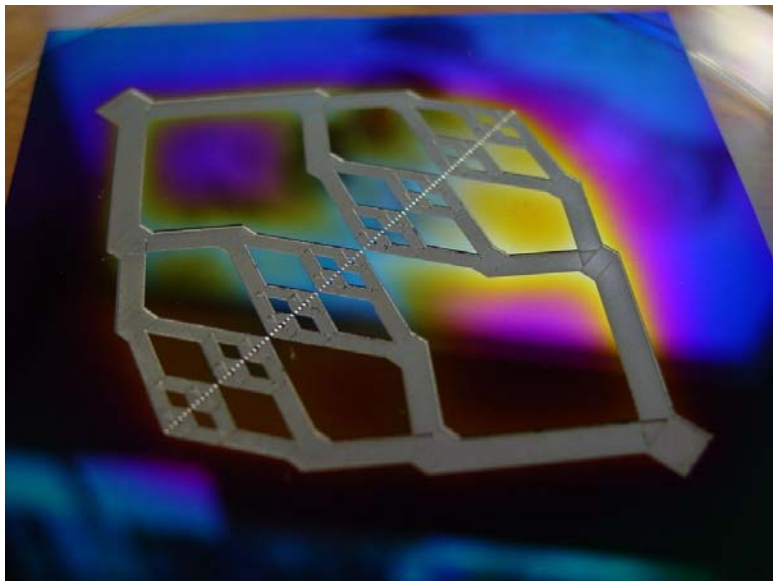

Figure 2-21: 7-level branching network

Table 2-3: The depths of each generation of 9-level branching network and processing parameters. The scan speed is 8 mm/s. Average power, p, focal position, z, and number of scan passes, N.

Generation	Depth (μm)	Parameters			
		p (W)	z (mm)	N	etching (s)
1st	317	2.73	0	2	40
2nd	252	1.9	0	2	40
3rd	200	1.5	0	2	40
4th	159	1.79	0	1	40
5th	126	2.95	2	1	40
6th	100	0.86	1	1	40
7th	79	1.84	2	1	40
8th	63	0.56	1	1	40
9th	50	0.25	1	1	40

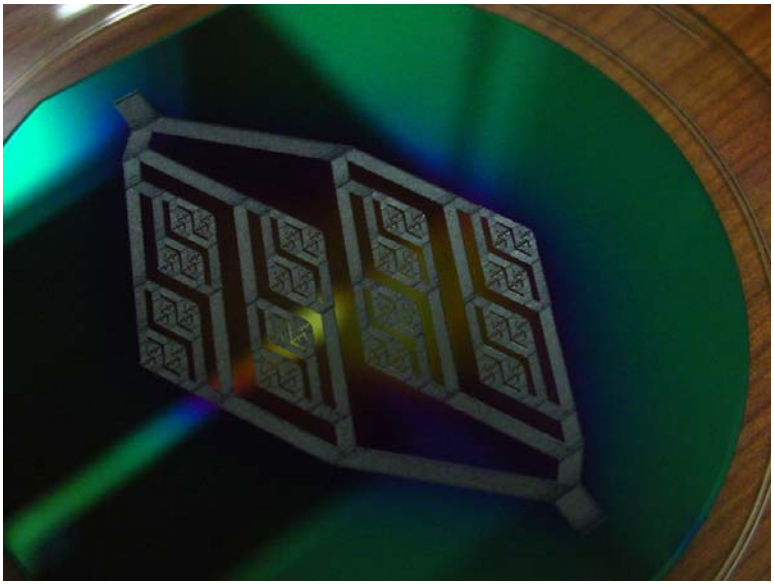

Figure 2-22: 9-level branching network

Table 2-4: The depths of each generation of 11-level branching network and processing parameters. The scan speed is 8 mm/s. Average power, p, focal position, z, and number of scan passes, N.

Generation	Depth (μm)	Parameters			
		p (W)	z (mm)	N	etching (s)
1st	202	1.5	0	2	40
2nd	160	1.79	0	1	40
3rd	127	2.95	2	1	40
4th	101	0.86	1	1	40
5th	80	1.84	2	1	40
6th	64	0.56	1	1	40
7th	50	0.25	1	1	40
8th	40	1.25	2	1	20
9th	32	0.76	2	1	20
10th	25	0.33	1	1	20
11th	20	0.25	1	1	20

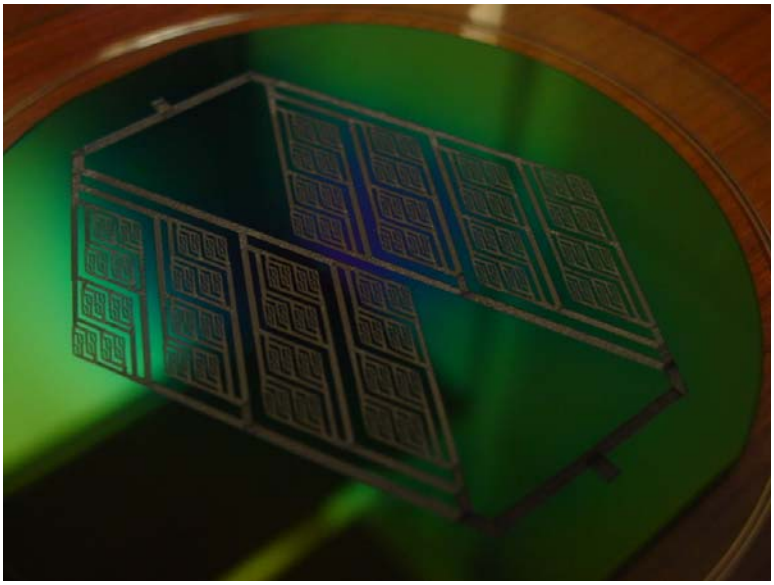

Figure 2-23: 11-level branching network

2.5 CONCLUSIONS

IR nanosecond ablation of silicon is studied for construction of multi-depth microchannel networks. The argon gas injection is effective to eject molten material out of the laser ablated zone, and thus laser energy transfer to the target surface is improved. Chemical wet etching in the HF and HNO_3 solution is effective to improve the surface roughness due to strong thermal reaction of silicon to IR nanosecond pulses. Use of optimal processing parameters can minimize the surface roughness while channel depth is manipulated. For the power and focal range used in this study, the speed ranging from 8 – 16 mm/s minimizes the surface roughness. Together with laser processing parameters, the time of the chemical wet etching as post processing is also a critical parameter to determine the depth and the surface roughness of laser machined micro-channels. In fabrication of multi-depth microchannel networks, the etching time is selected as time it takes for the threshold depth to be etched into minimal depth in the designed networks. Then the other laser parameters are varied to achieve different corresponding channel depth using the same etching time.

CHAPTER III

FEMTOSECOND PULSED ABLATION

3.1 INTRODUCTION

Femtosecond (fs $=10^{-15}$ s) lasers refer to a category of laser with sub-picosecond pulse duration. The pulse is also known as ultra-fast or ultra-short pulses. The femtosecond laser pulses have been attractive for a wide variety of micromachining applications because of their ability to fabricate micron-level features with minimal peripheral damage and associated debris [41, 42, 48]. Typical electron-phonon energy transfer takes ~10^{-13} s and thus during fs laser interaction neighboring atoms do not get affected leading to minimum collateral damage. The machined quality and the resolution of such ultrashort laser pulses have been demonstrated in many "proof of concept" experiments [35-38, 41-43, 48, 49]. The application of femtosecond laser writing that is based on the ablation of substrate material at or below the surface is described by Giridhar et al. [38]: microfluidic pathways and chambers 10-100μm wide and 5-50μm deep on several glass plates were fabricated. The prospects of ultrashort pulse machining for a variety of materials are shown in a review [35], where femtosecond laser micromachining was successful on the surface of metal (aluminum, steel), glass, diamond, polymers, PMMA, silica, and ceramic substrates. Femtosecond laser drilling of straight and 3D microchannels in glass was made with help of liquid and an ultrasonic chamber

[36]. In the study, straight and bent microchannels having high aspect ratios and smooth machined walls were produced. In other studies, 3D hollow microstructures were formed inside glass with direct write of a near-infrared femtosecond laser followed by post-annealing and preferential acid etching [37, 43]. The use of a femtosecond laser to create topographical structure in PDMS substrate was reported [49].

Femtosecond laser ablation is studied as a potential tool to realize artificial vascular networks with wider depth range with better quality compared to the channel that is fabricated with nanosecond pulses. As demonstrated in Chapter 2, it becomes possible to fabricate multi-depth branching microchannel networks obeying Murray's law with nanosecond ablation followed by acid etching. However, the channel depth range with a reasonable surface quality is not wide enough to realize variety of microchannel network designs. Although the chemical wet etching as post-processing smoothes the surface roughness, relatively long chemical etching time to remove debris buildup, resulting from a strong thermal reaction of irradiated silicon, limits the minimum channel size. Alternatively, non-thermal process of femtosecond ablation minimizes collateral damage due to thermal effects including melting, boiling and fracture [41, 42, 48].

The example in figure 3-1 demonstrates how the improved processing precision reduces the required etching time, which in turn reduces the minimum width and depth. Furthermore, the uniformity of the interior surface and edges are significantly improved. However in order to fully take advantage of these benefits, it is necessary to machine the entire structure with ultrashort pulse laser. Compared with related costs, however, the low productivity of femtosecond pulses has limited its contribution in practical applications. In the majority of applications, macroscopic material removal as well as micron-level

precision is required.

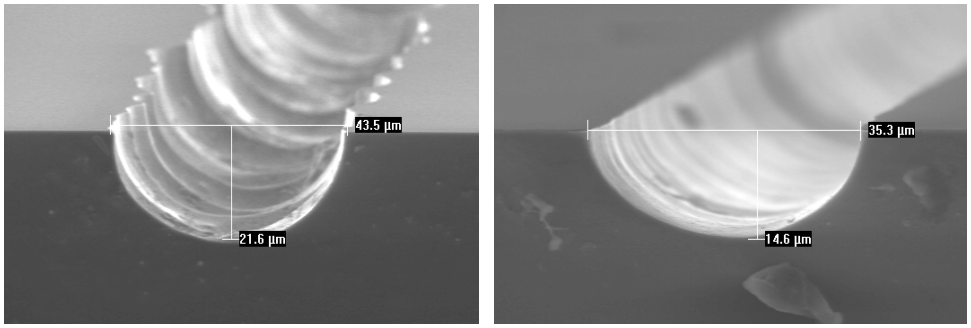

(a) **(b)**

Figure 3-1: SEM images of nitride coated silicon, (a) nanosecond laser machined channel after 30 s etching; (b) femtosecond machined channel after 20 s etching

Progression of experiments is planned to determine and optimize processing parameters for the fabrication of multi-depth microchannel branching networks into silicon wafer. Here, the influence of processing parameters, such as the pulse energy / the focal position / the scan speed / the number of scan passes, on machined channel is investigated. Then, processing parameters are optimized to fabricate wide range of microchannel depth with quality surface and to increase the processing speed.

As a demonstration, a 9-level branching network designed using Murray's law, for which the depth range is 50 to 320µm, is laser machined into a silicon wafer. Actual branching network is created out of PolyDiMethylSiloxane (PDMS) using the laser machined silicon structure as mold.

3.2 EXPERIMENTAL

The schematic of the femtosecond laser micromachining setup is shown in figure 3-

2. The laser used for this study is a femtosecond pulsed fiber laser operating at 1040 nm. The femtosecond laser is set to produce ~600 fs pulses with ~10 μJ pulse energy at repetition rate of 200 kHz. So, the output average power is ~2 W at 200 kHz. The average power is varied using a combination of a half-wave plate and a polarizer in beam delivery. A quarter-wave plate is used to circularly polarize the beam at target. The beam shape is near Gaussian. Using a 125-mm focal length F-theta objective, the beam spot size (see Chapter 3.2.1) at focus is approximately 11.3 μm in radius. A two-mirror galvanometric scanner and an X-Y-Z motion stage are used to control the position and the motion of laser beam spots.

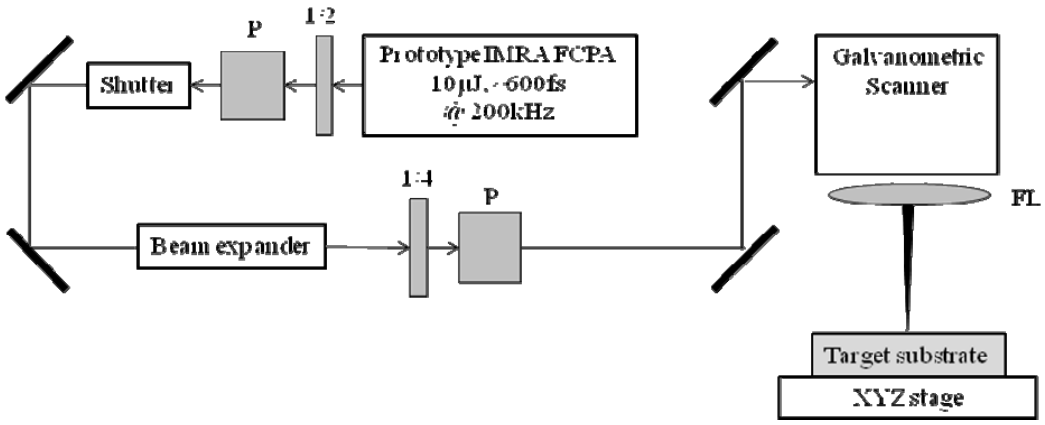

Figure 3-2: Experimental system schematic: polarizer (P), half wave plate (1/2), quarter wave plate (1/4), and focal lens (FL)

For wide channels, the beam is scanned side by side with 20 μm pitch as illustrated in figure 2-14. Channels are machined into the silicon wafer with a 3000 Å nitride coating. The wafer is N-type and <100> in crystal orientation. As post-processing, chemical wet etching with a solution of 49 % HF and 69 % HNO_3 with a ratio of 10:1 is

done to smooth the roughness of the laser ablated surface. The nitride layer is resistive to this etchant, so the laser ablated area is selectively etched as illustrated in figure 2-11. SEM images are taken to see the laser ablated surface and to measure the size of microchannels. Laser machined silicon samples are cleaved using a glass cutter for cross-section images of micro-channels. Surface roughness is measured with a commercial surface profiler (Taylor Hobson: Intra)

3.2.1 Beam shape and spot size

Beam spot size and fluence are essential parameters for studies of laser ablation. In this study, the laser beam is focused to less than tens of microns for micromachining applications. So, it is not appropriate to measure these parameters with common methods using photodiode array or pinhole detector due to their limited resolution. Alternatively, for Gaussian irradiation distribution, the beam spot size and the threshold fluence are determined from curve fitting of the dependence of ablated spot diameter, D, on the pulse energy, E_p, [**50**]. The fit function is written as:

$$D^2 = 2w^2 \ln\left(\frac{F_0}{F_{th}}\right) \qquad (3-1)$$

where w is the beam spot radius of full width $1/e^2$ maximum ($FW1/e^2M$) of Gaussian beam, F_{th} is the threshold fluence of silicon, and F_0 is the laser fluence and defined by following forms:

$$F_0 = \frac{2E_p}{\pi w^2} \qquad (3-2)$$

While this measurement technique is simpler and more accurate than the knife edge method used in Chapter 2.2.1, this is not applicable when laser ablated spot size is not clearly defined. In nanosecond ablation, as shown in figure 3-3(a), the ablated spot size is unclear because the edge of the spot is messed up with splashed molten material and collateral damage. On the other hand, as shown in figure 3-3(b), ablated spot area by femtosecond pulse is clearly defined compared with nanosecond ablation because femtosecond laser irradiation does not have enough time for thermal interaction with target material.

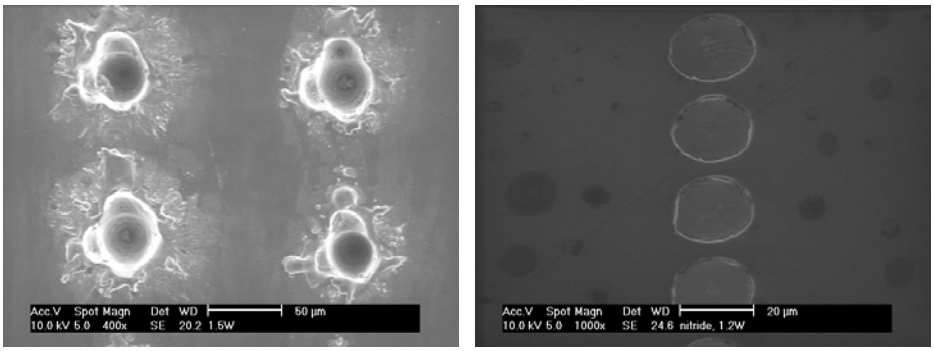

(a) **(b)**

Figure 3-3: SEM images of craters on nitride coated silicon created by (a) 200 ns pulses and (b) 600 fs pulses

Figure 3-4 presents a series of pictures representing the ablated spot size increase with the pulse energy. The pulse energy is controlled by manipulating the average power at 200 kHz repetition rate. Pulse to pulse is fully separated by increasing the scan speed to 3750 mm/s. The dependence of ablated spot size on the pulse energy is plotted in figure 3-5. The series of data points is curve fitted with equation 3-1. About 11.3 μm FW1/e^2M focal spot radius for Gaussian irradiation is calculated from the slope of the curve. And about 0.331 J/cm^2 threshold fluence for bare silicon is determined with the

intersection point.

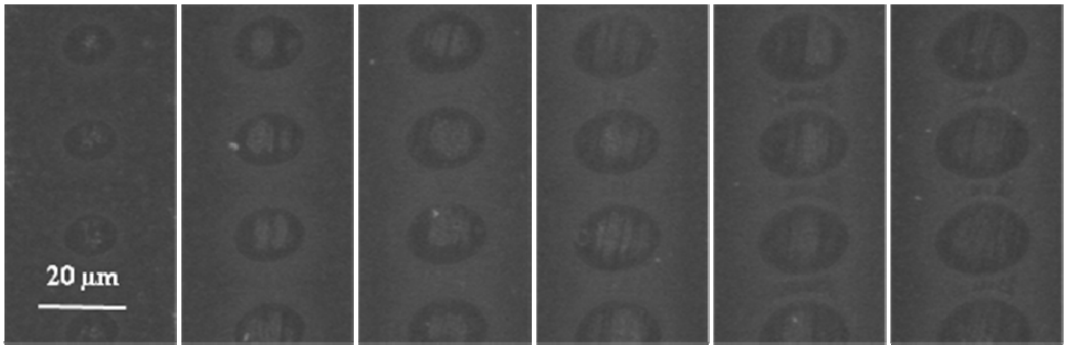

Figure 3-4: SEM images of femtosecond ablated spots on silicon. Pulse energes, E_p, are 2.15, 2.9, 3.6, 4.35, 5.05, and 5.75 µJ from left

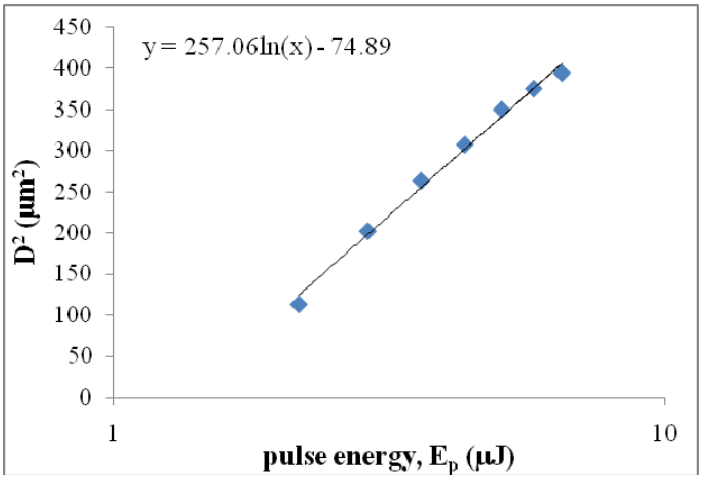

Figure 3-5: Semilog plot of spot diameter, *D*, dependence on laser pulse energy, E_p

3.2.2 Measurement of material removal rate

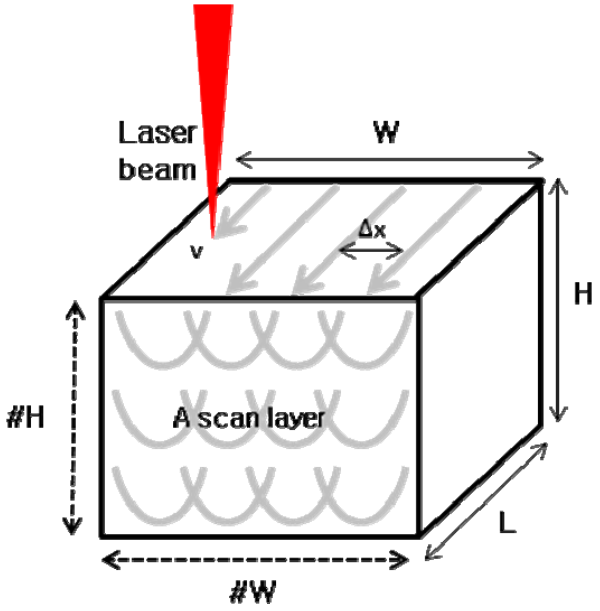

Figure 3-6: Schematics of laser ablation of microchannel

In laser ablation of microchannels as illustrated in figure 3-6, each layer is scanned parallel with the pitch, Δx, of 20 μm. And the number of the laser scanned layers, *#H*, is manipulated to control the depth, *H*, of channels. Here, a simply way to measure the material removal rate is derived. It is particularly convenient and accurate if the microchanel depth is clearly defined. The material removal rate is the channel volume divided by the processing time. The volume of the laser ablated channel and the processing time are written in terms of several parameters.

$$vol = L \cdot W \cdot H \qquad (3-3)$$

$$t = \#H \cdot \#W \cdot \frac{L}{v} \qquad (3-4)$$

Here, v denotes the scan speed, *vol* the channel volume, *t* the processing time, *L* the length of channel, *W* the channel width, and #W the number of parallel scan composing a laser scanned layer as illustrated in figure 3-6. The pitch, Δx is expressed as *W/#W*. Dividing *vol* by *t*, the material removal rate is obtained as

$$\frac{vol}{t} = \frac{L \cdot W \cdot H}{\#H \cdot \#W \cdot L \cdot \frac{1}{v}} = \frac{H \cdot \Delta x}{\#H \cdot \frac{1}{v}} \qquad (3-5)$$

The depth of microchannel is measured using an SEM picture. Other values in equation are all given as input parameters.

3.3 PROCESSING PHYSICS

Current phase of our artificial lung development requires multi-level structures with depths ranging from 20 μm to several hundreds of micron. Additionally, the surface roughness should be minimized to reduce any probable influence of rough surface on blood activation and damage resulting in blood clotting and clogging [**2, 25**]. Achieving the necessary feature depth with rapid processing speed requires efficient energy transfer from laser to the target; however, the energy transfer must be well controlled in order to maintain sufficient surface smoothness. The laser energy transferred to target can be manipulated with processing parameters such as the number of scan passes, the scanning speed, and the pulse energy. Here, the number of scan passes and the scan speed are considered as two main parameters because of the relatively low pulse energy of ~10 μJ and the high repetition rate of 200 kHz. First, the ablation depth range in a single pass scanning is measured to optimize the average power, focal position, and scan speed. In

the multiple passes scanning, the influence of the scan speed on the material removal rate and the surface roughness is studied. Based on the parameter study results, a 9-level branching channel is laser machined into silicon as an example.

3.3.1 Cross section shape of microchannels

In this section, influence of processing parameters such as the average power, the focal position, and the number of passes, on the cross section and the depth of femtosecond machined microchannels are studied. ~325 fs pulses with 2 μJ pulse energy at 100 kHz repetition rate are used for this test. The FW1/e^2M spot size at focus is about 11 μm in diameter. The scan speed is set to 10 mm/s. Figure 3-7 shows variation of cross section with (a) the average power and (b) the focal position. When the intense laser beam is tightly focused, the material removal in laser ablation is not effective so that defect on the bottom of the channel is created. The defect reduces as the peak intensity decreases with decreasing the average power or defocusing. Figure 3-8 shows variation of cross section with the number of passes (a) at focus and (b) 100 μm defocus below surface. The cavity on the bottom of the channel is destroyed with the repetition of the laser scan. But the quality of ablated surface remains unsatisfactory. Manipulating the number of passes with defocused beam for less peak intensity is more effective for material removal as shown in figure 3-8(b). Thus, despite the superiority of femtosecond pulses in micromachining, these results show the necessity of efficient energy transfer from laser to target material to control the channel depth while maintaining smooth surface. The energy transfer is controlled with manipulating the processing parameters.

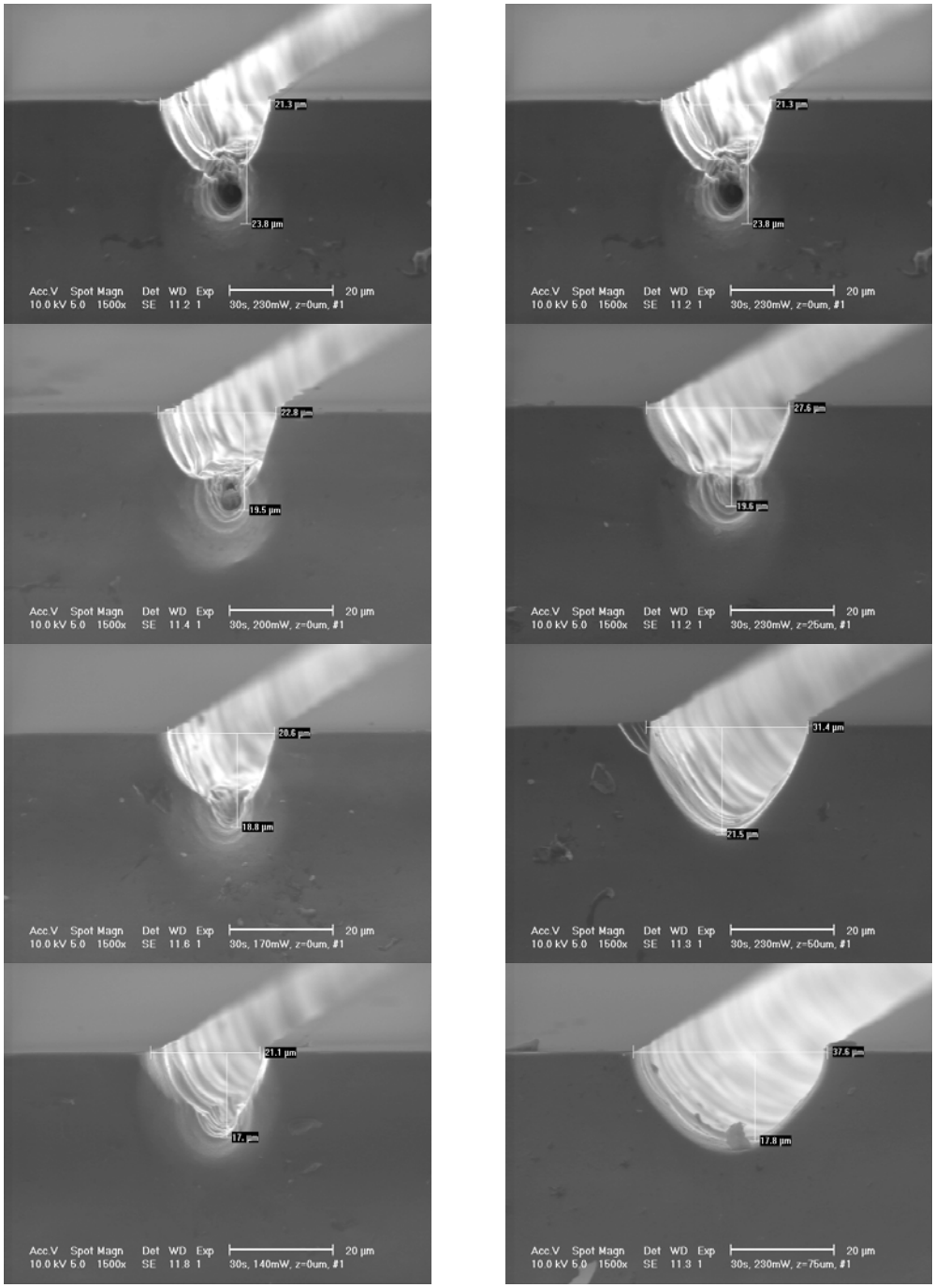

(a) **(b)**

Figure 3-7: (a) From top, the powers are 203, 177, 150, and 123 mW at focus (b) From top, the focal positions are 0, 25, 50, and 75 µm defocus below surface with 203 mW average power. Operating condition is 10 mm/s scan speed, single pass, and 30 s etching

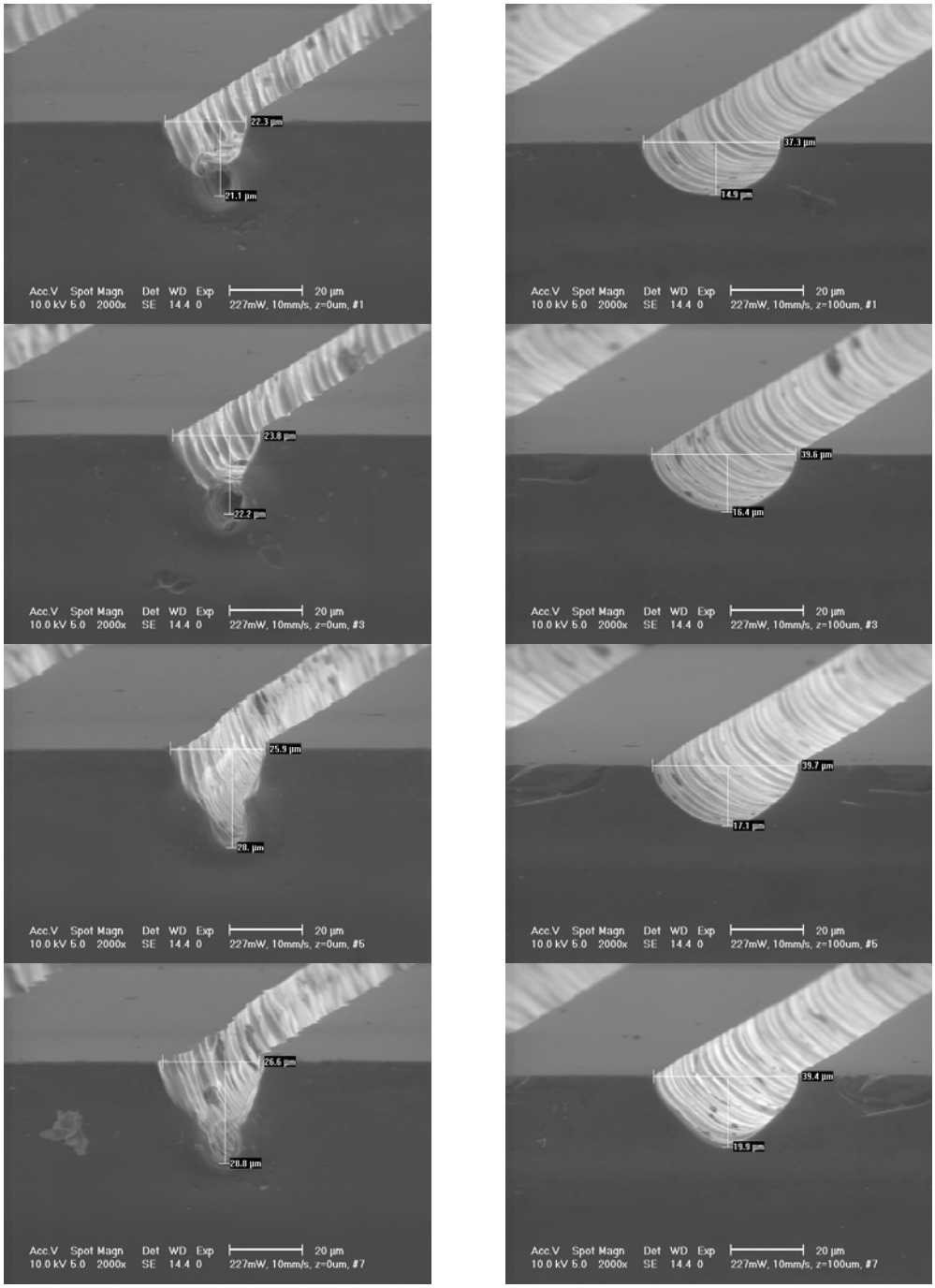

(a) **(b)**

Figure 3-8: From top, the numbers of passes are 1, 3, 5, and 7 (a) at focus and (b) 100 µm defocus below surface. Operating condition is 203mW average power, 10 mm/s scan speed, and 30 s etching

3.3.2 Choice of the scan speed in single pass scan

Higher power femtosecond laser is used to make wider range of microchannel depth. The femtosecond laser is set to produce ~600 fs pulses with 10 μJ pulse energy at 200 kHz repetition rate. The FW1/e^2M spot size at focus is about 11.3 μm in radius.

If silicon substrate is irradiated by high intensity pulses at a slow scan speed like 1mm/s, the ejection of the ablated material is not so effective that a notch-like shape is created on the bottom of the channel as shown in figure 3-9 and 3-10. The depth of the notch-like shape is formed by the depth difference between the penetration and the material removal. The formation of the shape is not desired for effective material removal with smooth surface. Such defect is attributed to the ineffective ejection of the ablated material when pulses with high intensity are overlapped too much by a low scan speed.

In the plot in figure 3-9, the average power of more than 1W does not help to make deep channels. Also, in the focal test in figure 3-10, the penetration depth is its maximum at focus, but actual material removal is the most at 0.5mm defocus below the surface. In order to avoid creating such a notch-like structure on the bottom of laser ablated channels, ranges of the average power and the focal position creating such defect can be cut out from the plots in figure 3-9 and 3-10. Although more pulse energy penetrates deeper into silicon wafers, this increase does not necessarily result in deeper material removal.

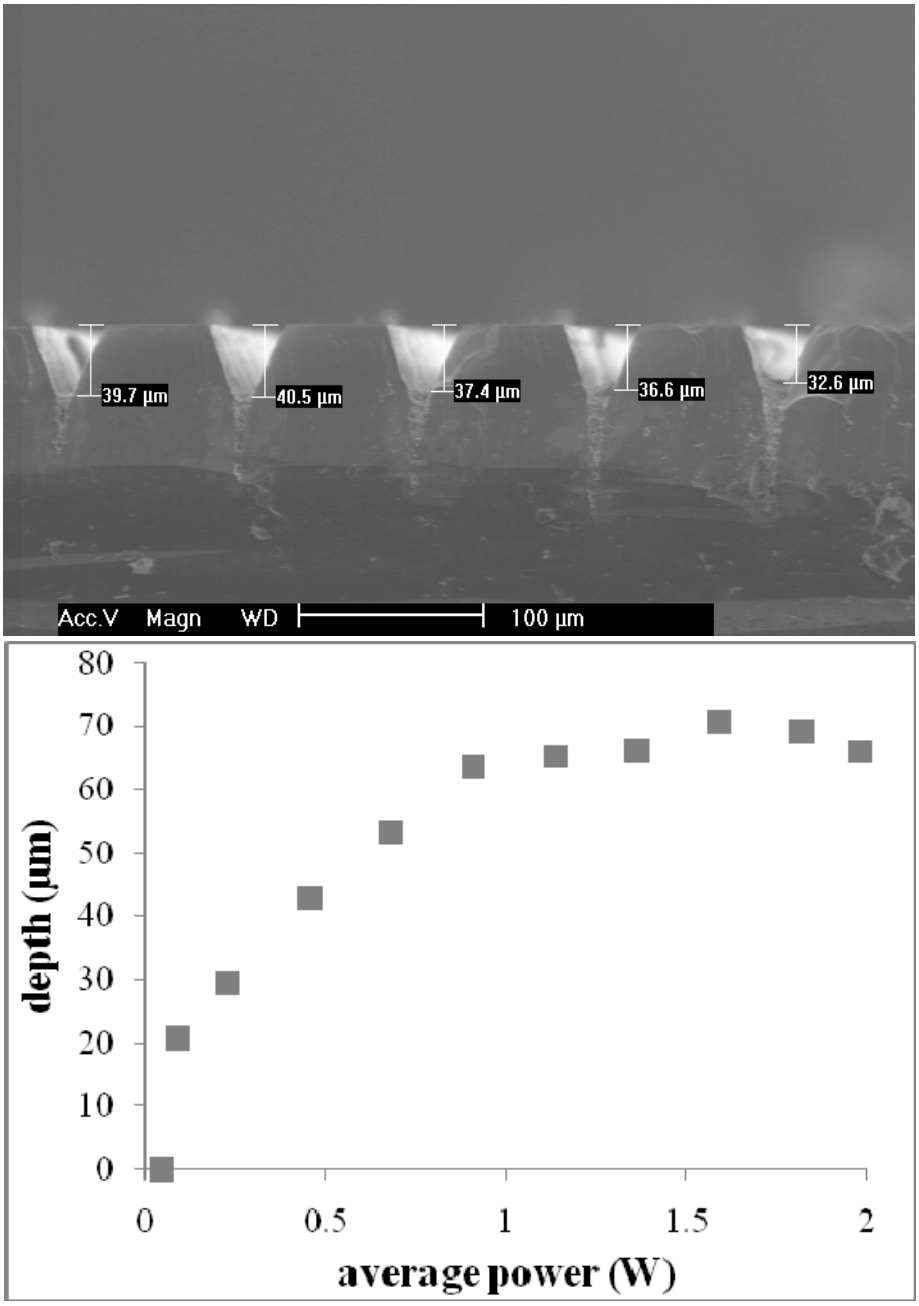

Figure 3-9: (Top) The channels on the image are created with different average powers: 1.14W, 1.36W, 1.59W, 1.82W, and 1.98W from the left. All other processing parameters are same and the sample is wet etched for 10s. (Bottom) Ablation depth vs. average power. Depths are measured after 20s chemical etching. Operating parameters: 1mm/s transverse speed, 200kHz repetition rate, 600fs pulse width, 1040nm wavelength, at focus, and 30µm focal spot size.

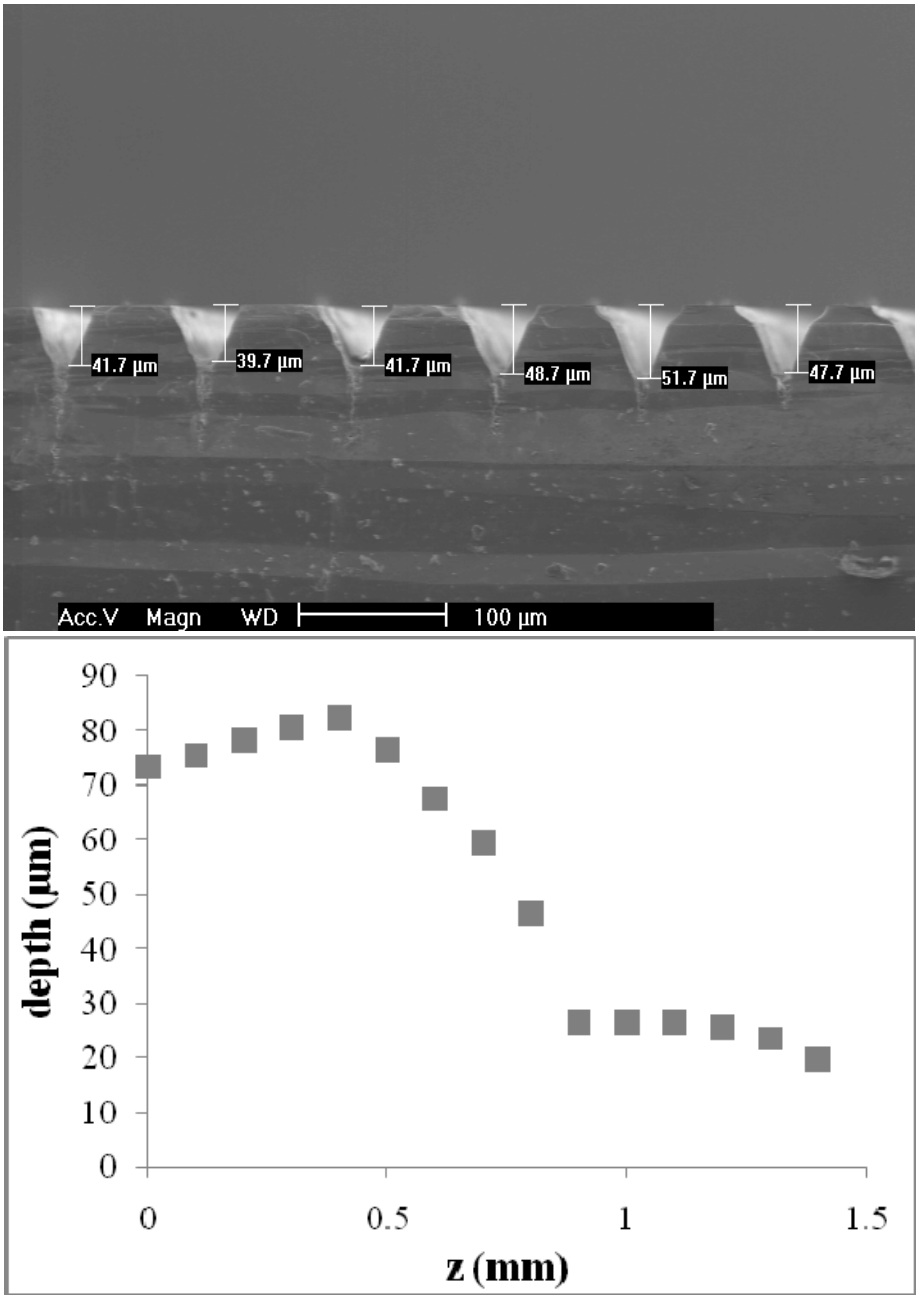

Figure 3-10: (Top) The channels on the image are created with different focal positions below the surface: z=0mm, 0.125mm, 0.25mm, 0.375mm, 0.5mm and 0.625mm from the left. All other processing parameters are same and the sample is wet etched for 10s. (Bottom) Ablation depth vs. focal position. Depths are measured after 20s chemical etching. Operating parameters: 1mm/s transverse speed, 200kHz repetition rate, 600fs pulse width, 1040nm wavelength, 1.98W average power, and 30µm focal spot size.

Another method of avoiding the defect on the bottom of channel is to control the scan speed. Selecting appropriate scan speeds, the notch-like shape can be avoided for smooth surface and effective depth control is achieved. In the SEM image in figure 3-11, the notch-like defect is not observed at scan speeds of more than 5mm/s even with a full power at focus. In this image, the scan speed of 5 mm/s provides deepest and smoothest channel among the channels on the image.

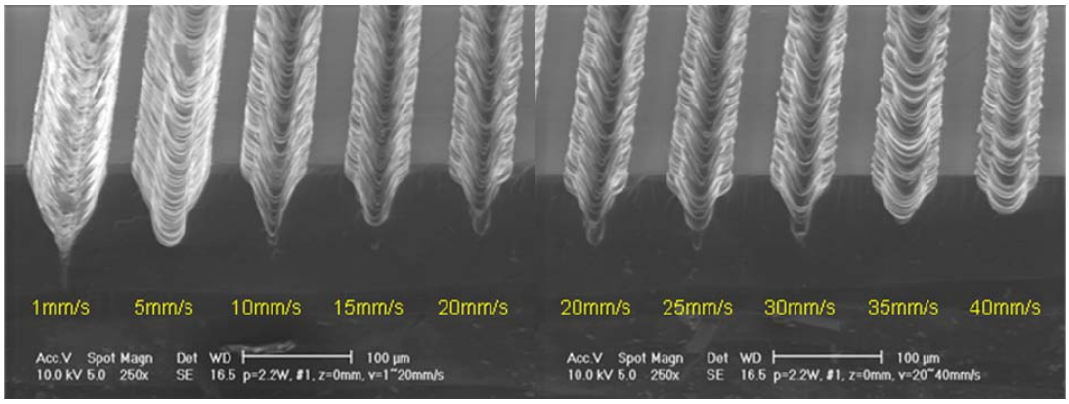

Figure 3-11: SEM images of micro-channels machined with femtosecond laser pulses at different scanning speeds. All other processing conditions are same and etching time is 20s.

Manipulating the pulse energy (or the average power) and the focal position below the surface, the depth of channels created with the laser ablation and 20 s etching is varied from 17 to 63 µm as presented in figure 3-12. Here, the scan speed is set to 5 mm/s at the repetition rate of 200 kHz. As intended, the notch-like defect on the bottom of channels is not observed at 5mm/s scan speed with single pass scanning after 20 s acid etching. At power just above the ablation threshold of nitride coat on silicon wafer, only the nitride layer with 0.3 µm thickness is removed by laser pulses. Here, the nitride coating protects the silicon from chemical etching. So the jump in the plots is developed

only by selective chemical wet etching. In other words, the minimum depth of 17 µm is purely created by 20 s acid etching when only the nitride coating is removed by laser pulses. Thus, with a single pass scanning, the ablation depth range is less than ~50 µm.

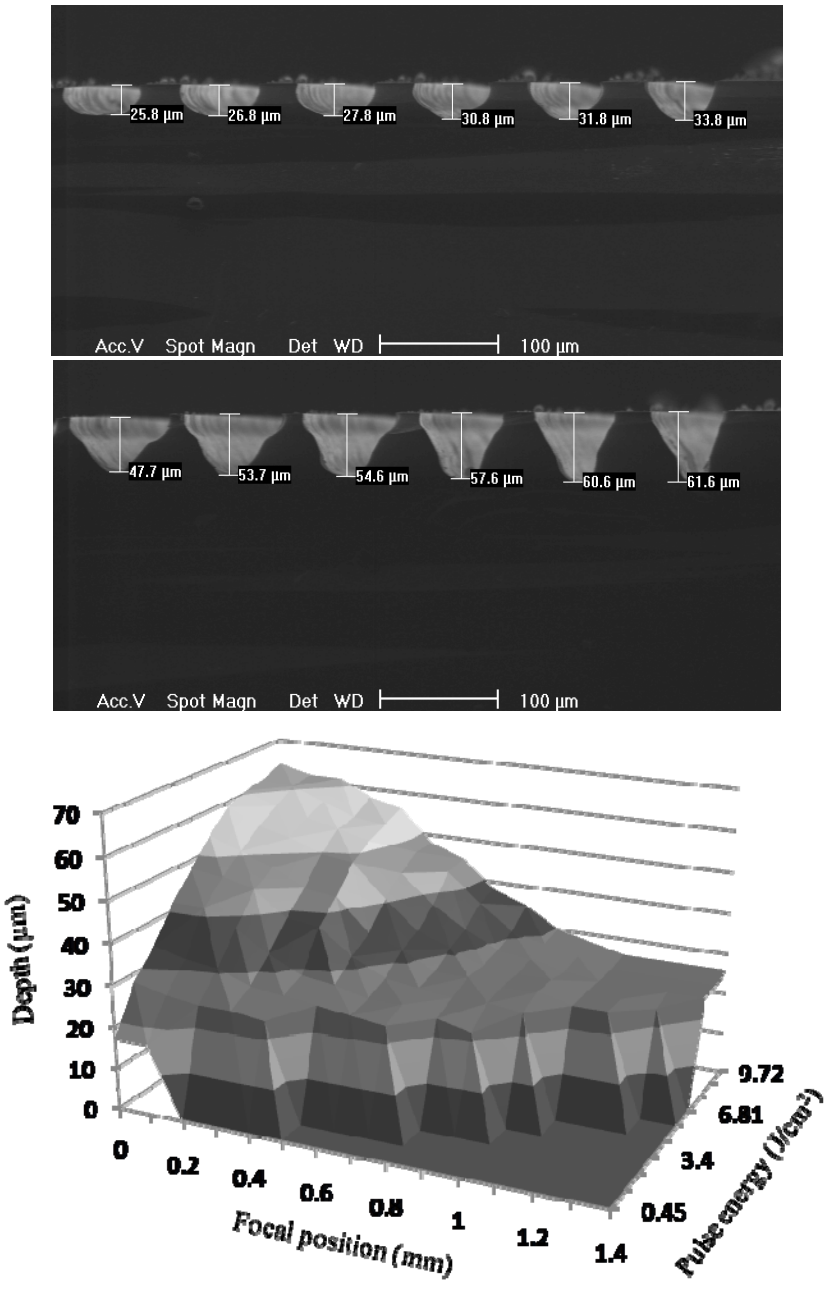

Figure 3-12: Depth of laser ablated channel vs. focal position below the surface and the pulse energy. Transverse speed is 5mm/s. Depths are measured after 20s chemical etching.

3.3.3 Choice of the scan speed in multi-layer scan

With single scan pass, the pulse energy of ~10 μJ is not strong enough to create wide range of microchannel depth up to several hundreds of micron. As described in previous section, at some point, decrease of scan speed does not help to make deeper channel due to the ineffective ejection of the ablated material. Therefore, the number of scanned layers (see Chapter 3.2.2 for the definition) is increased to expand the microchannel depth. For wide channels, each layer is scanned parallel 20 μm pitch as depicted in figure 3-6. The femtosecond laser is set to produce ~600 fs pulses with 10 μJ pulse energy at 200 kHz repetition rate. The FW1/e^2M spot size at focus is about 11.3 μm in radius.

Figure 3-13 shows surface morphologies of laser ablated channels before acid etching. The number of scanned layers is 1, 3, 5, and 7 from top. With 5 mm/s scan speed in figure 3-13(a), the depth of channel does not increase as the number scanned layers increases. Debris buildup fills the channel and blocks laser energy delivery to the target surface. And the debris accumulates with the number of scanned layers. In previous section, such debris problem is not observed in single pass scan even with the same operating condition. In the multiple parallel scan of wide area, each scan line is overlapped depending on the pitch. So, the overlap causes the debris buildup seemingly coming from heat accumulation. When the scan speed increases to 20 mm/s, less debris are observed as presented in figure 3-13(b). And channel depth almost linearly increases with the number of scanned layers until debris accumulation starts. Considerable debris buildup is also observed with more than 7 scanned layers as presented in the bottom of figure 3-13(b).

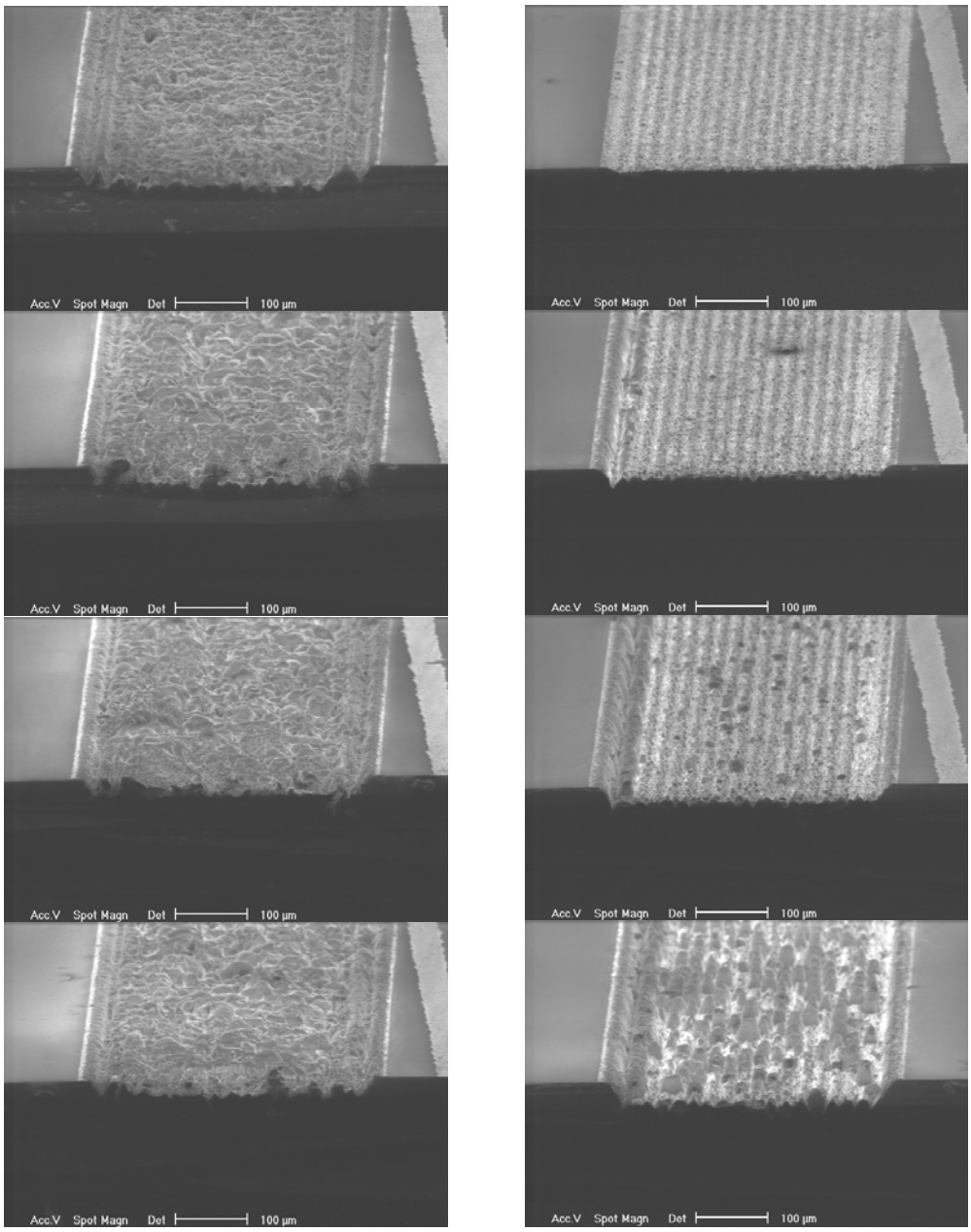

(a) **(b)**

Figure 3-13: The number of scanned layers is 1, 3, 5, and 7 from top with the scan speed of (a) 5 and (b) 20 mm/s. Operating condition is 2 W average power, at focus, 20 µm pitch, and no acid etching

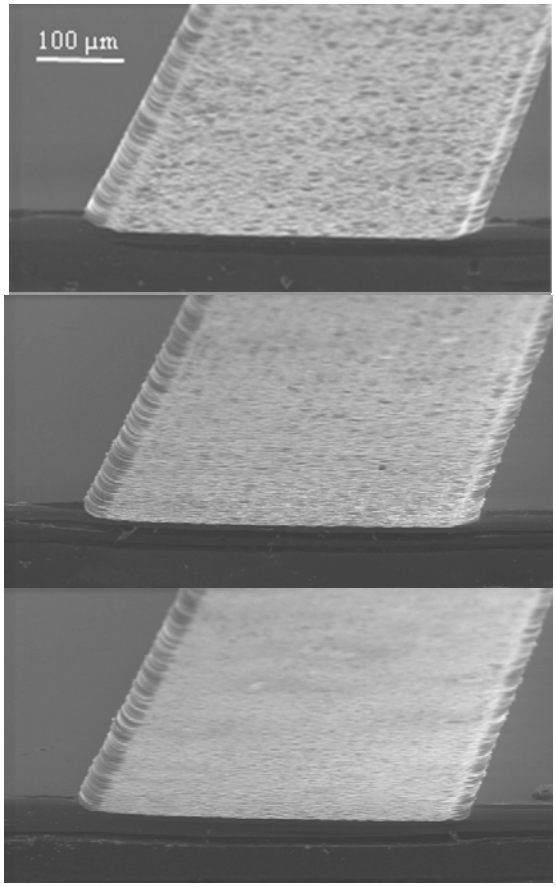

Figure 3-14: The scan speed is 30, 90, and 150 mm/s, from top. Operating condition is 2 W average power, at focus, 20 µm pitch, one scan layer, and 20 s acid etching

The scan speed is a key parameter to improve surface quality as well as to expand the machining range. As shown in figure 3-14 surface morphologies of laser ablations followed by acid etching are pretty different depending on the scan speed. At least up to 150 mm/s scan speed, the ablation surface gets smooth as the scan speed increases.

To study the influence of a wide range of scan speed on femtosecond ablation a galvanometric scanning system is used instead of a linear motion stage. Maximum scan speed of the scanner used in this study is about ~6000 mm/s at target surface.

Combination of the high repetition rate (200 kHz) and the high speed scanning system facilitate the manipulation of the number of scanned layers. Thus, as shown in figure 3-15, microchannel depths up to several hundred μm can be achieved varying the number of scan layers.

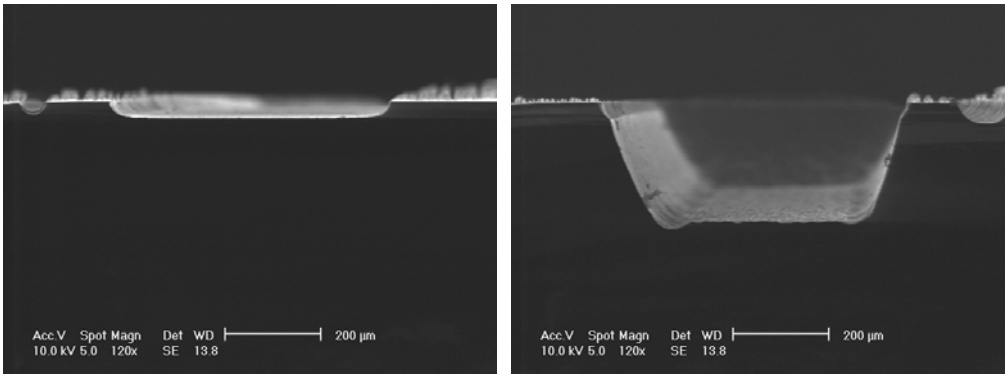

Figure 3-15: SEM images of cross section of laser machined channels on silicon after 20s acid etching. The scanning numbers 480 mm/s.

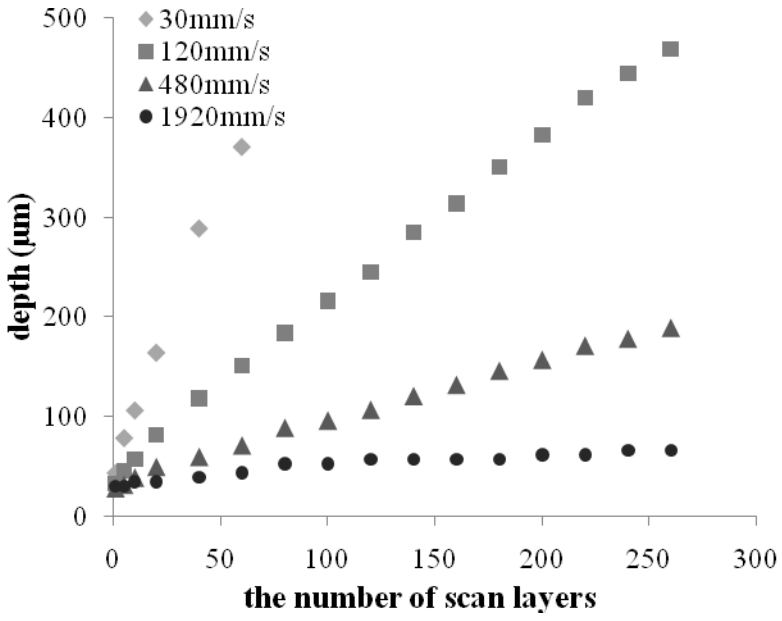

Figure 3-16: Ablation depth into nitride coated silicon wafer vs. the number of scan layers after 23 s acid etching. 10 μJ pulses are scanned at focus with four different scan speeds: 30, 120, 480, and 1920 mm/s.

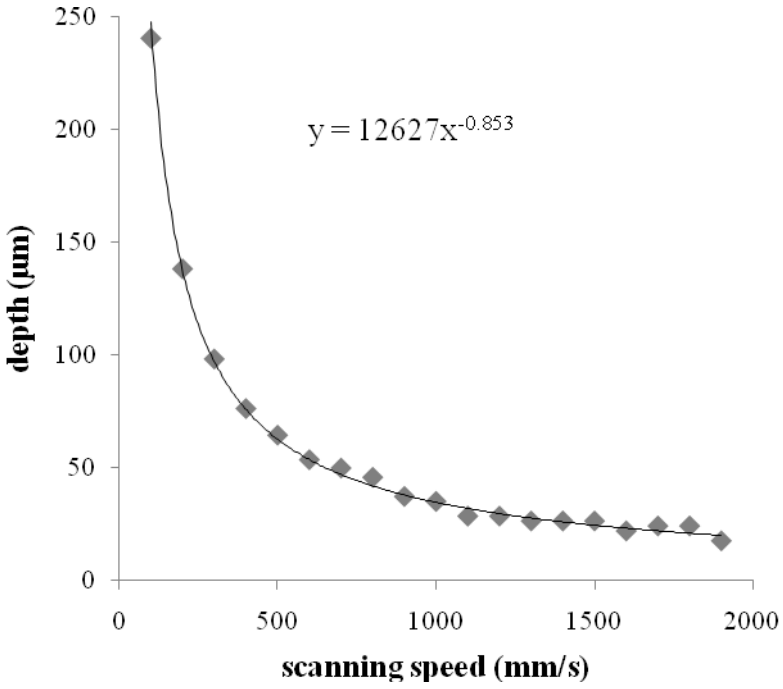

Figure 3-17: Ablation depth into nitride coated silicon wafer vs. the scan speed after 19 s acid etching. The number of scanned layers is 100 and the pulse energy is 10 μJ at focus

The ablation depth linearly increases with the number of scan layers as shown in figure 3-16. At 30 mm/s, the ablation depth saturated to around 300 μm after ~50 scan layers due to debris buildup, which fills the channel and blocks laser energy delivery to the target surface. For 120 mm/s, however, such saturation is not observed up to 260 passes corresponding to ~470 μm depth. The number of scan layers when the debris starts building up is observed to increase as the scan speed increases. So, the appropriate choice of the scan speed is important to achieve a wide machining range. And the ablation depth with 100 scan layers as a function of the scan speed, v, is shown in figure 3-17. The data fit well to a $v^{-0.853}$. That is, more numbers of scan layers are required to make the same depth of microchannel with faster scan speed using same pulse energy.

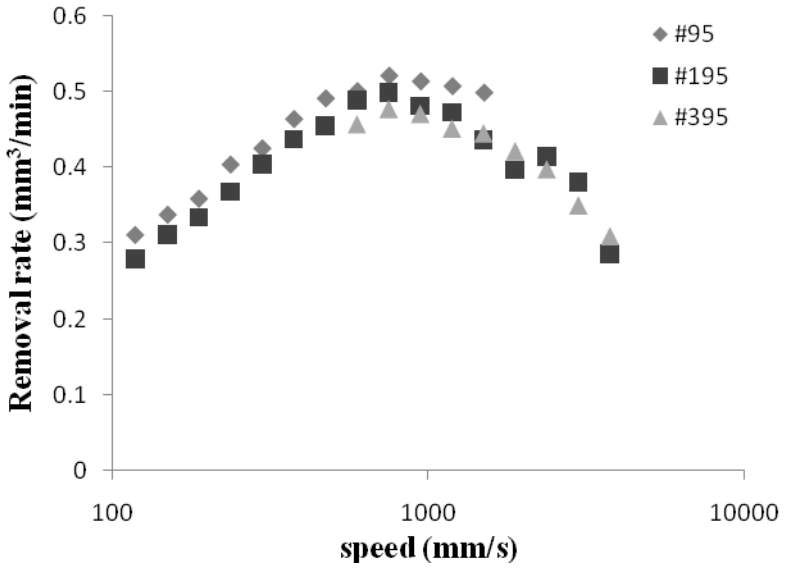

Figure 3-18: The material removal rate vs. scan speed

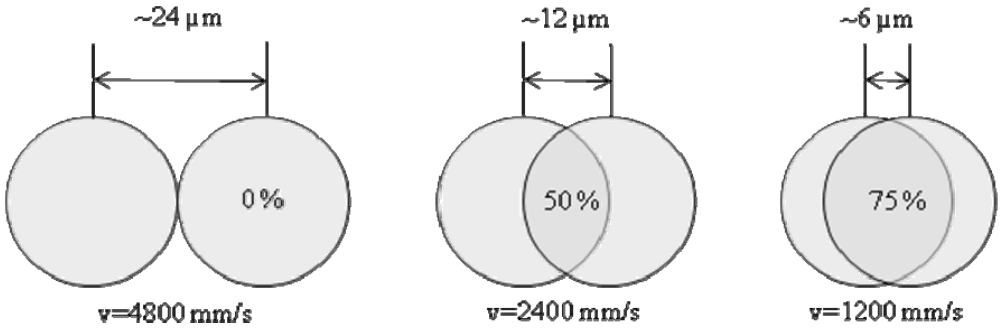

Figure 3-19: Schematic sketch to illustrate the relation between the scan speed and the overlap of each crater with diameter of ~24 µm. The interval between each pulse at 200 kHz is 5 µs, so the scan speed is more than ~4800 mm/s to separate each crater created by a single pulse.

In order to find out an optimal scan speed to provide effective material removal, the material removal rate is measured in terms of the scan speed. The material removal rate is measured as described in Chapter 3.2.2. The variation of the material removal rate with the scan speed is shown in figure 3-18. The material removal rate is measured for three different numbers of scan layers: 95, 195, and 395. In the measurement, the affect of the acid etching is removed. The maximum material removal rate is obtained round 750 mm/s scan speed. As depicted in figure 3-19, 750 mm/s scan speed corresponds to ~84 % overlap of laser ablated spots with ~24 μm diameter created by a 9.72 μJ pulse. The material removal rate slightly decreases as the number layers increases for all scan speed. This is primarily due to the defocusing with the increase of the ablation depth, since the focal position is fixed during machining and the Rayleigh range is ~300 μm.

The scan speed also plays a key role in the machined surface quality. Interpolating the linear dependence of the ablation depth on the number of scan layers, the number of scan layers for 100 μm depth is plotted in terms of the scan speed as shown in figure 3-20. Using this result, depths of channels are fabricated to 100 μm with less than 2% error by varying the number of scan layers according to the scan speed. Figure 3-21 shows the average surface roughness of the same ablation depth in terms of the scan speed. The scan speed range providing the optimal material removal also creates smooth channel surface.

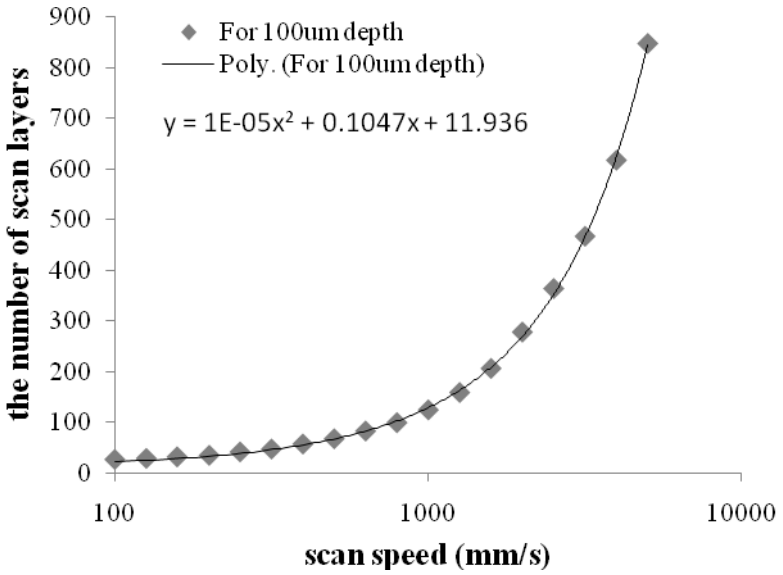

Figure 3-20: The number of scanned layers as a function of the scan speed to make 100 µm depth after 20 s acid etching

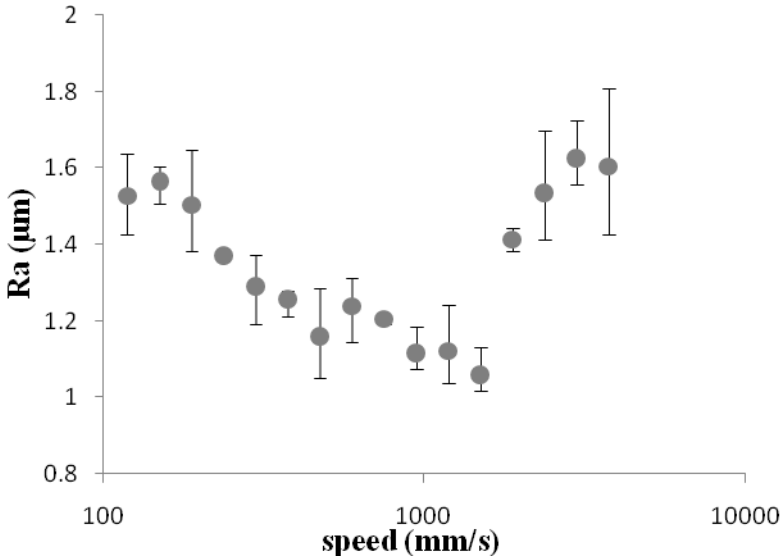

Figure 3-21: The average surface roughness (Ra) vs. the scan speed after 20 s acid etching

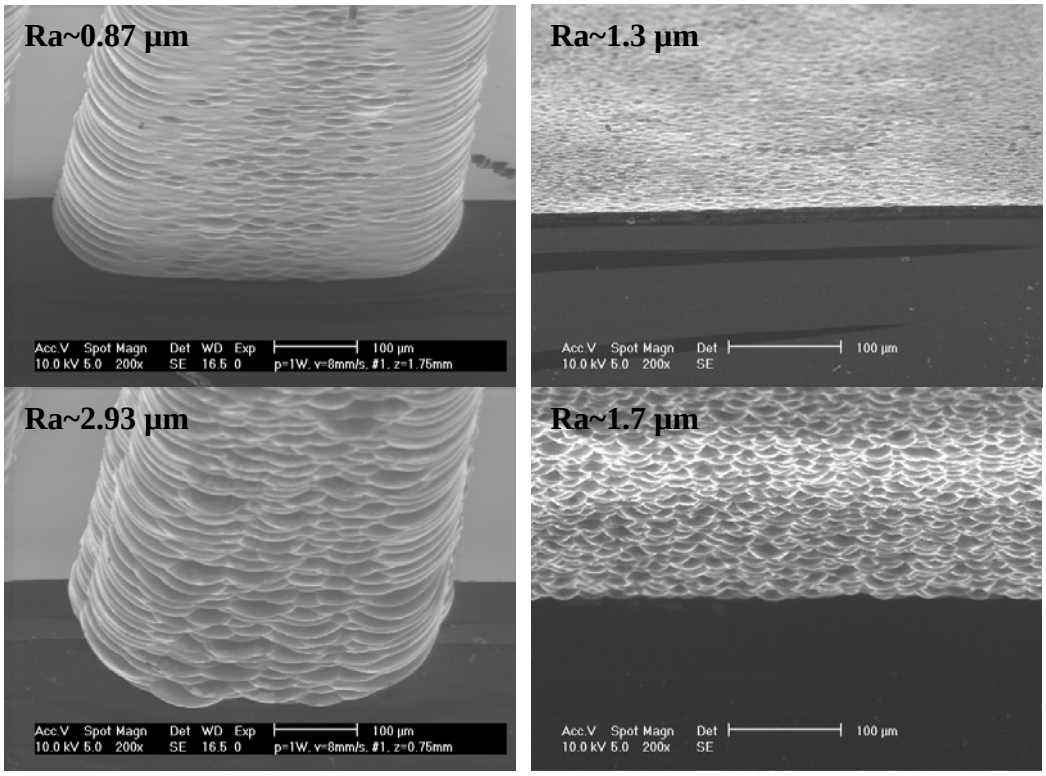

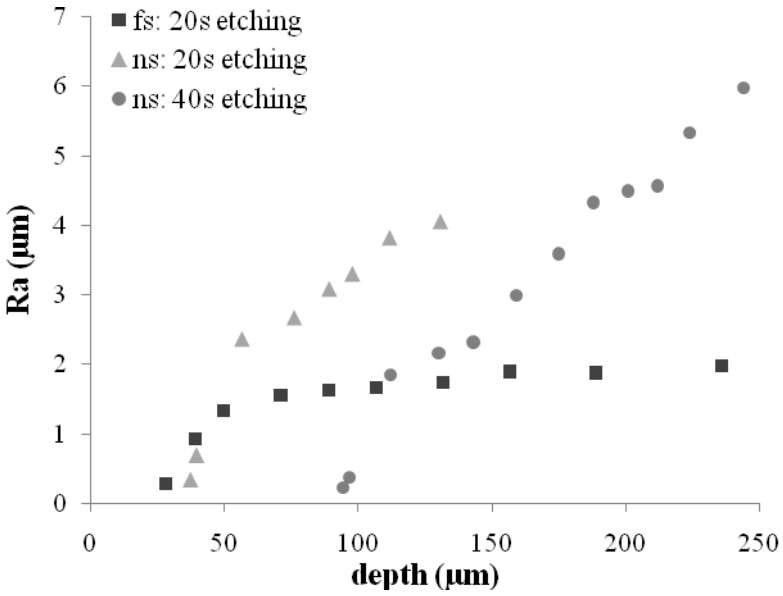

(c)

Figure 3-22: Surface morphologies of (a) nanosecond ablation after 40 s acid etching and (b) femtosecond ablation after 20 s acid etching. (c) Average roughness, Ra vs. depth for fs and ns laser machined channels after acid etching. The scan speeds are set to 8 mm/s for ns and 480 mm/s for fs.

3.3.4 Femtosecond vs. nanosecond ablation

The morphology of the laser ablated silicon surface after chemical etching process as shown in figure 3-22(a, b) provides an understanding of a quantified surface roughness. The dependence of the ablation surface roughness on the channel depth is plotted in figure 3-22(c). For femtosecond (fs) ablation, the scan speed is set to 480 mm/s and the number of scan layers is varied from 1 to 330 resulting in ablation depths from 28 to 236 μm after 20 s etching. For comparison, channels are machined with a pulsed Nd:YAG laser operating at 1064 nm with 500 Hz repetition rate and 100 μs pulse width. The 100 μs pulses are modulated to produce a series of 200 nanosecond (ns) pulses with 10 μs interval. The near-Gaussian beam spot size of FW1/e^2M is about 30 μm in diameter. The average power is manipulated from 0.2 to 3 W with the scan speed of 8 mm/s and 0.5 mm defocus below surface. For both fs and ns laser ablation, the surface roughness increases with the ablation depth. For 20 s etch time, the maximum ns ablation depth, with the average roughness (Ra) of < 2 μm, is ~50 μm; whereas, for fs ablation, a depth of more than 200 μm is less than 2 μm Ra. Increasing etch time for ns ablated channel to 40 s increases the maximum depth with < 2 μm Ra to ~130 μm; however, the minimum channel depth also increases to ~90 μm.

Gas exchanger performance can be limited in two significant ways by thermal effects associated with the IR nanosecond laser. First, longer acid-etching is required to remove the recast and heat-effected material thereby limiting the minimum channel size. Second, the internal channel surfaces and edges are notably rougher. While this does not limit the initial performance of the device, it may lead to blood clotting or clogging which are the primary causes of device failure. SEM images in figure 3-23 are taken after 4 hours blood flow along nanosecond machined channels. It is shown that rougher surface

has more risk of protein or blood cell depositions, which can cause blood clotting or clogging. Although blood flow test in femtosecond machined channels is not conducted, it is expected that the smoother surface of femtosecond ablation can reduce the chance of protein or blood cell depositions.

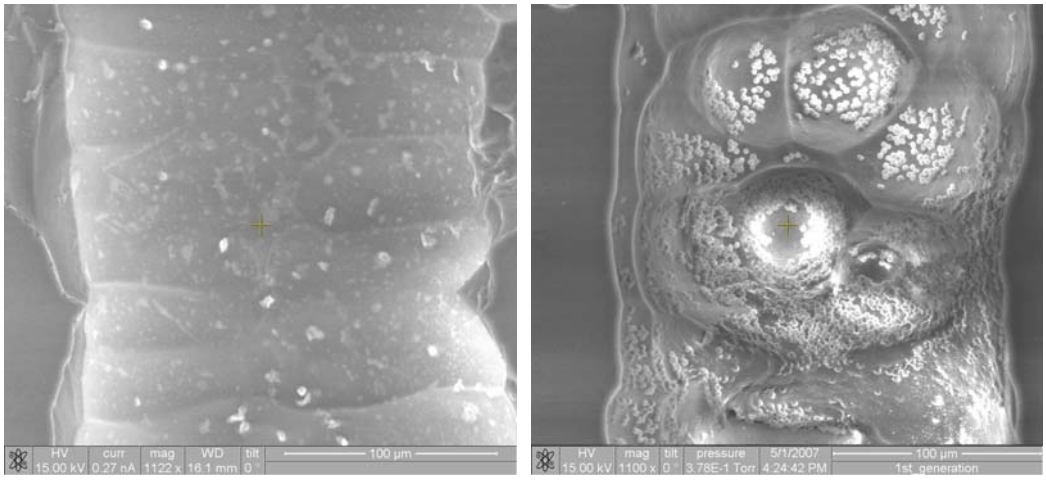

(a) (b)

Figure 3-23: SEM images of Microchannels after 4 hours blood flow. The microchannels are machined with 200 nanosecond pulses. The average surface roughnesses are (a) ~0.8 and (b) ~4 µm

3.4 MULTI-DEPTH MICROCHANNEL NETWORK

As a demonstration, a 9-level branching network is laser machined into a nitride coated silicon wafer with the femtosecond laser. And, acid etching post process is applied to the laser machined silicon. The SEM image in figure 3-24 shows the surface morphology of the laser machined channel surface after 20 s etching. The depth of the branching network ranges from 50 to 317 µm as presented in table 3-1. The etching time is selected as time it takes for single scan depth to be etched into minimal depth in the

networks. Then the number of scan layers is manipulated to achieve different corresponding channel depth using the same etching time. The number of scan layers for desired depths is chosen by interpolating the plot in figure 3-25. In the depth control with the number of scan layers, the processing time as well as the surface roughness is reduced with increasing the etching time. Table 3-1 compares the number of scan layers required to achieve the same depth of channel. The number of scan layers with 30 s etching is less than that with 23 s etching. The laser processing times of this branching network are about 5 and 4 hrs with 23 and 30 s etching respectively. Thus, macroscopic material removal in addition to micron level precision is achieved with fs ablation.

An actual blood flow/oxygen-exchange (oxygenator) device is created from the PDMS using the laser machined silicon structures as molds, as shown in figure 3-24(a). A thin film of PDMS is placed on top of the PDMS network to make a closed channel. Blood flows inside the channels and gas exchanges through the gas permeable PDMS film. The molding and sealing procedure is described in Chapter 4.2.

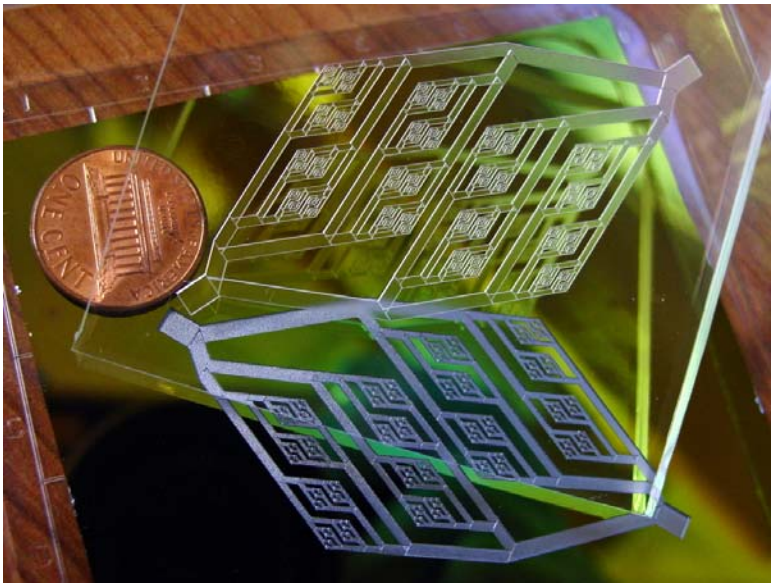

(a)

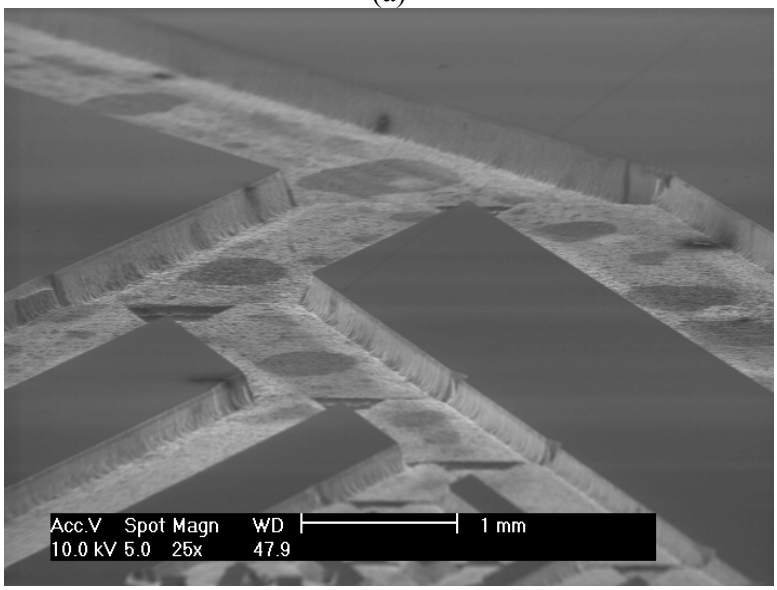

(b)

Figure 3-24: (a) 9-level branching network laser machined into nitride coated silicon and PDMS replica. The process is done at focus with 480mm/s scan speed and the etching time is 20 s. (b) SEM image of the network in silicon.

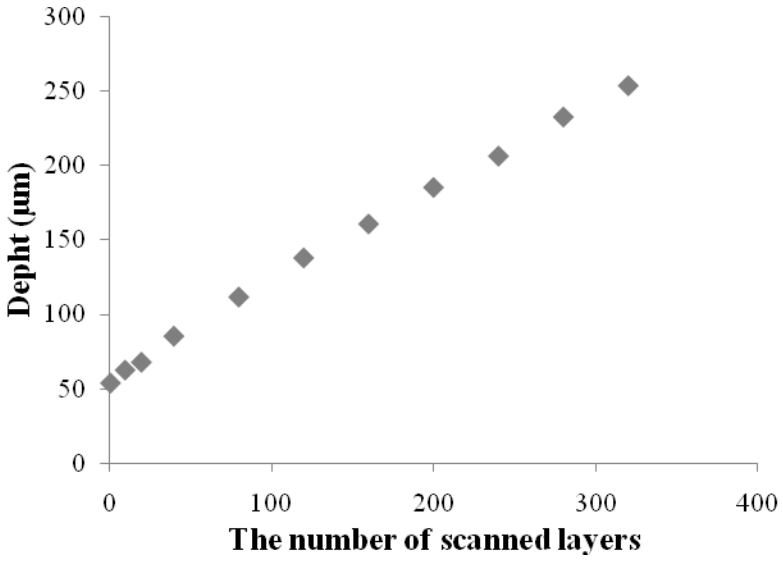

Figure 3-25: Laser ablation depth into nitride coated silicon wafer vs. number of scan layers after 30s chemical etching. The process is done at focus with 480 mm/s scan speed.

Table 3-1: The depths of each generation of 9-level branching network and the number scan layers with 23 s etching. The scan speed is 480 mm/s

Generation	Depth (µm)	The number of scan layers	
		23 s etching	30 s etching
1st	317	462	442
2nd	252	356	318
3rd	200	271	229
4th	159	204	157
5th	126	150	102
6th	100	108	62
7th	79	74	33
8th	63	47	10
9th	50	26	1

3.5 SIMULATION OF FEMTOSECOND INTERACTION WITH SILICON

For the femtosecond laser ablation, development of a model which will provide the scientific basis and theoretical framework for the laser interaction physics is investigated and attempted. Femtosecond (sub-picosecond) pulses in laser ablation end to be more precise than nanosecond (or long) pulses. Non-thermal process of femtosecond ablation minimizes collateral damage due to thermal effects including melting, boiling and fracture [41, 42, 48]. The advantages of the femtosecond pulses have been demonstrated in many studies [35-38, 41-43]. This is also illustrated in our fabrication of micorchannels with femtosecond pulsed laser. However, mechanism of the femtosecond laser material interaction is poorly understood and remains controversial. This is because extremely small time and length scales are involved in such process so that experimental approaches are limited.

A numerical modeling of the femtosecond pulse interaction with silicon is carried out to understand the physical processes involved in femtoescond ablation of silicon. In numerical studies on femtosecond ablation [41, 51-64], various approaches are suggested and modeled depending on the target materials. For dielectrics, the mechanism of photo-ionization by intense femtosecond pulses has been of interest and thus electron number densities are evaluated to estimate ablation threshold [58, 59]. In studies on femtosecond ablation of conductive material (or metal), the interaction between electron and lattice during non-thermal equilibrium has been mostly characterized and modeled [60-64]. For semiconductors irradiated with an intense femtosecond pulse, however, one of both conductive and nonconductive characters has been assumed and corresponding models have been applied in numerical studies [51-57]. Here, both characters are considered in

numerical modeling of femtosecond pulse-silicon interaction, i.e. free electron (or electron-hole pair) generation followed by thermalization process is considered.

When intense laser pulse in femtosecond regime is incident on silicon, a complex chain of processes occur. Initially, electrons in the valence band excite to the conduction band absorbing the photon energy of intense laser beam. The generation of free electrons is followed by secondary processes. The free electrons absorb the laser energy and have excess energy. And electron-electron interactions lead to an equilibrium electron distribution (Fermi distribution) in which an electron temperature is defined. The hot electrons in quasi-equilibrium interact with the lattice and cools down to reach equilibrium with lattice. It is generally accepted that such thermalization process takes a few picoseconds.

Laser beam propagation in bulk silicon is simulated by solving the Maxwell's equations [67, 68] with finite-difference time-domain method (FDTD) [69, 70]. In calculating electrical conductivity of laser induced electron-hole plasmas in silicon, influences of the electron temperature and the electron number density on laser beam propagation in material are taken into account. Among the various models used for simulation of the free electron generation, here we adopt the linear and two-photon absorption (TPA) [55, 65] which are expected to be dominating, so that the electron number density is obtained. It is assumed that the electrons build up quasi-equilibrium state absorbing energy of the laser field. The thermalized electrons cool down while interacting with the lattice. Energy conservation in such mechanisms is described as the two temperature model (TTM) [66]. Temporal and spatial dependence of material parameters (such as the electron temperature, the lattice temperature, the electron number

density, thermal properties, and electric properties) is reflected in the femtosecond laser material interaction by solving coupled equations with an iterative scheme.

Transient evolution of silicon properties such as the electron number density, the electron conductivity, the electron temperature and the lattice temperature are characterized in this numerical modeling.

3.5.1 Incident beam profile

Single femosecond pulse is considered in this modeling. The femtosecond pulse is assumed to have Gaussian profile in time and space. Thus, the incident beam, $I_0(r,t)$, at target can be written as

$$I_0(r,t) = \frac{2\Delta E}{\pi w^2}\exp\left[-\frac{2r^2}{w^2}\right]\cdot\frac{1}{\Delta t}\sqrt{\frac{\ln 2}{\pi}}\exp\left[-\frac{t^2}{\left(\Delta t/\sqrt{\ln 2}\right)^2}\right] \qquad (3-6)$$

where r is the distance to the Gaussian beam axis; t is the time; ΔE is the pulse energy; w is the beam spot radius of full width $1/e^2$ maximum ($FW1/e^2M$); Δt is the pulse duration. As mentioned in chapter 3.2, the femtosecond laser output is ~600 fs pulses with the pulse energy of ~10 μJ. and the beam spot size at target is approximately 11.3 μm in radius.

3.5.2 Laser beam propagation in bulk silicon

The electromagnetic field of laser in bulk silicon is determined solving Maxwell's equations [67, 68]. Thus, reflection, absorption and transmission in the laser beam

propagation are described.

$$\nabla \cdot \vec{E} = \frac{\rho}{\varepsilon} \qquad (3-7a)$$

$$\nabla \cdot \vec{B} = 0 \qquad (3-7b)$$

$$\nabla \times \vec{E} = -\frac{\partial(\mu \vec{H})}{\partial t} \qquad (3-7c)$$

$$\nabla \times \vec{H} = \sigma \vec{E} + \varepsilon \frac{\partial \vec{E}}{\partial t} \qquad (3-7d)$$

Here, ρ denotes the volume charge density, ε the permittivity, μ the permeability, $\vec{E}$ the electric field, $\vec{B}$ the magnetic flux density, and $\vec{H}$ the magnetic field density ($\vec{B} = \mu \vec{H}$). Finite-difference time-domain method (FDTD) [69, 70] is employed to simulate electromagnetic scattering in the material. The electric field is assumed to have a superimposed incident and scattered field, $\vec{E} = \vec{E}_{incident} + \vec{E}_{scatter}$ [71]. The incident field is determined from the incident beam intensity given in Chapter 3.5.1. The scattered field for FDTD is obtained by solving the following equation [69, 70] instead of the equation (3-7d)

$$\varepsilon \frac{\partial \vec{E}_{scatter}}{\partial t} + \sigma \vec{E}_{scatter} = \nabla \times \vec{H}_{scatter} - \sigma \vec{E}_{incident} - (\varepsilon - \varepsilon_0) \frac{\partial \vec{E}_{incident}}{\partial t} \qquad (3-8)$$

where σ is the electrical conductivity of silicon and ε_0 is the permittivity of free space. Adopting electrical conductivity of laser induced plasma in Maxwell's equations, influences of the electron temperature and the electron number density on laser beam propagation in material is taken into account. Mur' absorbing boundary condition [72] is adopted to eliminate scattered field reflection at the boundary of computational domain. Laser beam intensity is obtained from Poynting vector, $\vec{S}$, [67] as follows

$$I = \left|\vec{S}\right| = \left|\vec{E} \times \vec{H}\right| \qquad (3-9)$$

3.5.3 Free electron generation

In silicon, the generation of conduction band electron (free electron or electron-hole pair) by an intense femtosecond pulse is described by linear and two-photon absorption (TPA) [65].The laser intensity and electron number density, n_e inside bulk silicon can be obtained by solving the following differential equation.

$$\frac{\partial n_e(\vec{r},t)}{\partial t} = -[\alpha_0 + \beta I(\vec{r},t)]\frac{I(\vec{r},t)}{h\nu} \qquad (3-10)$$

where z denotes the depth from the irradiated target surface into bulk silicon, α_0 the linear absorption coefficient, β the two-photon absorption coefficient, h Planck's constant and ν the frequency of light. Here, recombination is assumed to be negligible.

3.5.4 Electron-lattice interaction

It is assumed that the electrons generated by linear and TPA absorb the laser energy

and build up quasi-equilibrium state with diffusive motion. The thermalized electrons cool down interacting with the lattice. Energy conservation in such mechanisms is described as the two temperature model (TTM) [66].

$$\frac{3}{2} n_e k_B \frac{\partial T_e}{\partial t} = \nabla(k_e \nabla T_e) - G(T_e - T_l) + \sigma E^2 - U_i \frac{\partial n_e}{\partial t} \qquad (3\text{-}11\text{a})$$

$$C_l \frac{\partial T_l}{\partial t} = \nabla(k_l \nabla T_l) + G(T_e - T_l) \qquad (3\text{-}11\text{b})$$

Here, T_e and T_l denote the electron and lattice temperatures, k_B Boltzmann's constant, U_i the band gap energy for a electron, C_l the heat capacities for lattice, k_l the thermal conductivities for lattice. The source term, σE^2, describes the laser energy absorbed by electrons. The electron-lattice coupling coefficient G is calculated as follows [66]

$$G = G_0 \left\{ \left(\frac{T_e}{T_D} \right) D_4(T_e, T_D) - \left(\frac{T_l}{T_D} \right) D_4(T_l, T_D) \right\} \qquad (3\text{-}12)$$

where

$$D_4(T, T_D) = 4 \left(\frac{T}{T_D} \right)^4 \int_0^{T_D/T} \frac{x^4}{e^x - 1} dx \qquad (3\text{-}13)$$

$$G_0 \cong 3 \times 10^{16} \ [W/m^3 - K] \quad \text{for silicon [50]} \qquad (3\text{-}14)$$

where T_D is the Debye temperature. The delay of electron-phonon relaxation due to non-thermalized electrons is assumed to be negligible because the characteristic time of electron excitation is much shorter than the electron-phonon relaxation time.

3.5.5 Electrical conductivity

The electrical conductivity of the dense electron-hole plasmas generated by intense femtosecond pulse is a function of T_e and n_e. In the present study, such dependence of the electric conductivity of the ionized silicon is described by a modified Spitzer's model [73] for non-ideal plasmas as follows

$$\sigma(T_e, n_e) = \frac{\gamma_E T_e^{3/2}}{38Z \cdot \ln(1 + 1.4\Lambda_m^2)^{1/2}} \qquad (3\text{-}15)$$

where Z is the mean ionic charge, γ_E is a factor depending on Z and Λ_m, is the modified form of the Coulomb logarithm which is given as [73]

$$\Lambda_m = \frac{[\lambda_D^2 + \lambda_+^2]^{1/2}}{\bar{b}_0} \qquad (3\text{-}16)$$

Here λ_D is the Debye length, λ_+ is the mean ionic radius and $\bar{b}_0$ the impact parameter. These are given as follows [73]

$$\lambda_D^2 = \frac{\varepsilon_0 k_B T_e}{n_e e^2} \qquad (3\text{-}17)$$

$$\lambda_+^2 = \left(\frac{4}{3}\pi n_+\right)^{-2/3} \qquad (3-18)$$

$$\bar{b}_0 = \frac{Ze^2}{12\pi\varepsilon_0 k_B T_e} \qquad (3-19)$$

where e denotes the electron charge and n_+ the positively charged ion (hole) density.

3.5.6 Simulation

A Gaussian pulse with 600 fs full width half maximum (FWHM) at 1040 nm wavelength is assumed to be incident on bare silicon in simulation. The ablation threshold fluence for bare silicon is approximately 0.331 J/cm^2 with 11.3 μm FW1/e^{2}M spot radius for Gaussian profile. To save calculation time, 1 μm radius beam with the same intensity is assumed in simulation. The target silicon has the electric conductivity of 10-100 S/m. 4 μm x 4 μm x 2.5 μm (depth) domain is modeled with 0.05 μm grids. Temporal and special dependence of material parameters (such as the electron temperature, the lattice temperature, the electron number density, thermal properties, and electric properties) is reflected in this simulation by solving coupled fields and material equations with an iterative scheme.

3.5.7 Results and discussion

The reference time (t=0) is 300 fs before when the peak of Gaussian pulse with 600 fs FWHM passes the silicon surface. Figure 3-26 shows time history of laser intensity

distribution inside the silicon substrate. The Laser induced electric field inside bulk silicon is clearly illustrated. At ~17.9 fs, beam energy is concentrated at 0.8 μm below the surface as shown in figure 3-26 and disperses down later. At ~200 fs, the highest intensity is observed along the edge of the incident beam instead of the center axis. The "leaking" phenomenon, which occurs at the outer edge of Gaussian laser beam, is not clearly observed in this simulation because the incident beam has almost top-hat beam distribution. The evolution of the electron temperature distribution is similar to that of the laser intensity distribution as shown in figure 3-27. This is expected because the heating rate of free electrons by intense laser pulse in femtosecond time regime is extremely high and thus the characteristic time of the electron excitation is shorter than electron-electron and electron-lattice relaxation times. In other words, the free electrons respond instantly to the intense laser induced field. However, the response of the lattice is relatively slow. As shown in figure 3-28, the lattice temperature distribution is similar in shape to the electron temperature distribution, but the lattice temperature begins to rise much later.

Laser beam intensity is higher at the location slightly below surface, and likewise the temperature. This seems as a result of complex diffraction in beam propagation which is coupled with material properties. In present simulation, the domain depth is not deep enough to see the pulse energy dissipation: the domain size is comparable to the wavelength of 1.04 μm.

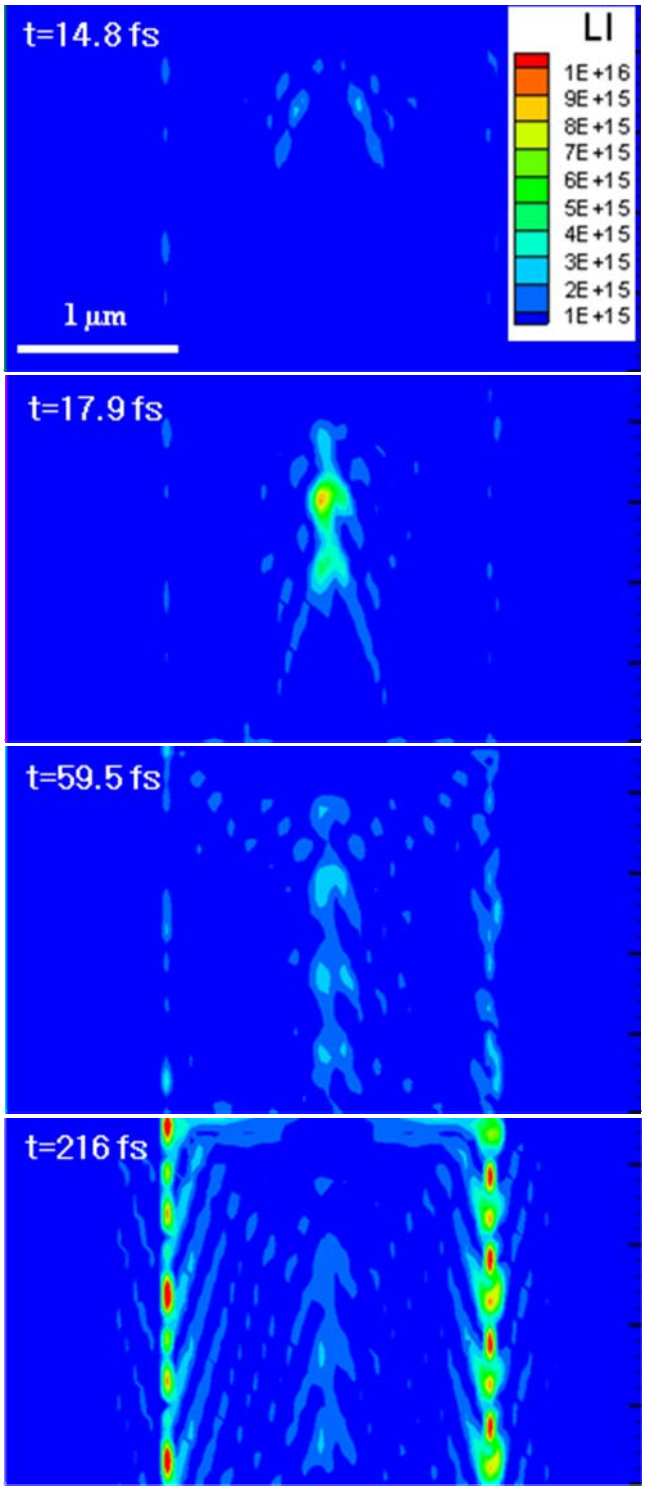

Figure 3-26: Evolution of laser intensity distribution in bulk silicon. The unit of the scale is W/m ^{2}.

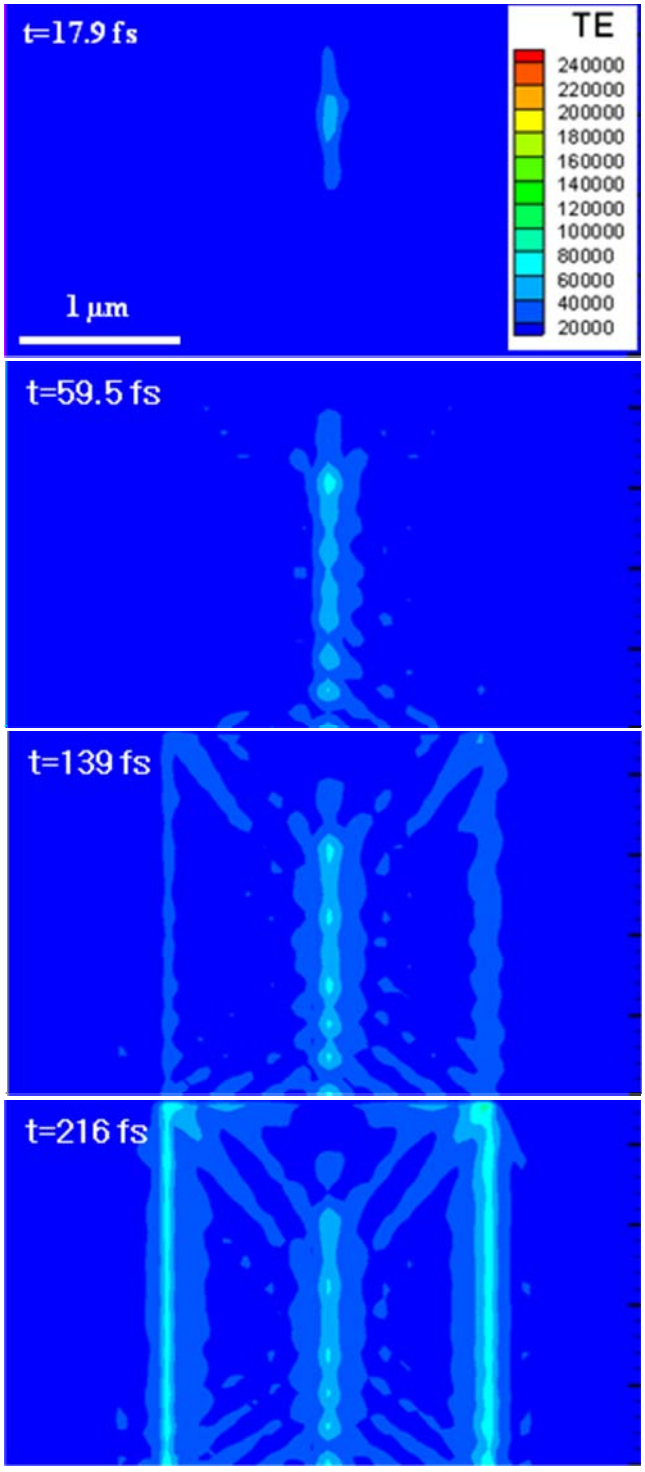

Figure 3-27: Evolution of electron temperature distribution in bulk silicon. The unit of the scale is Kelvin.

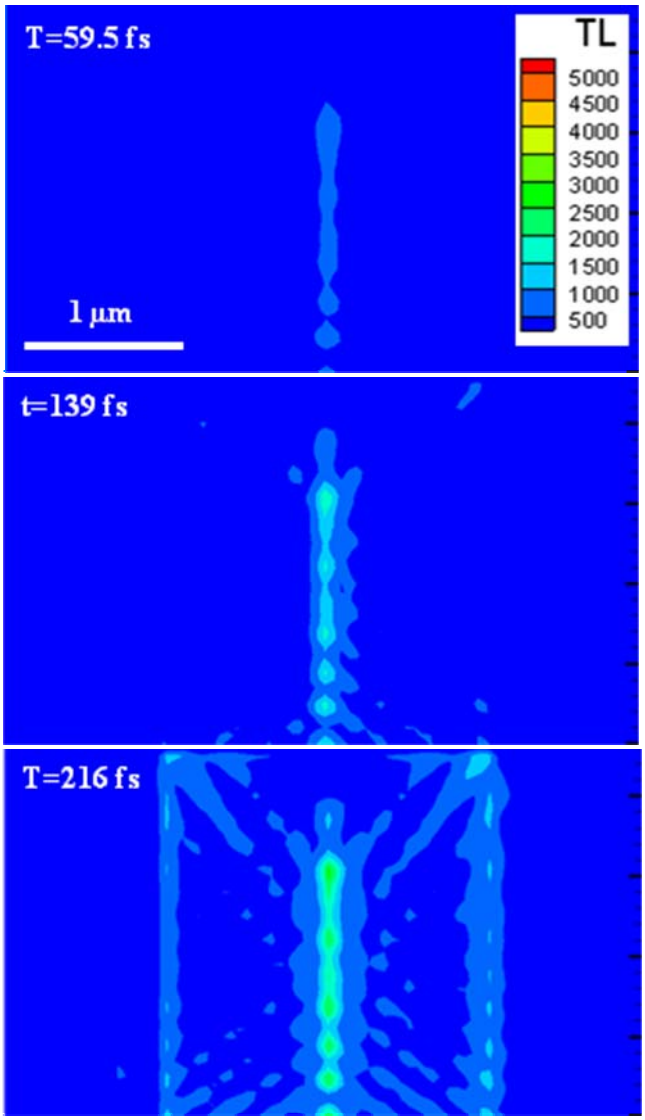

Figure 3-28: Evolution of lattice temperature distribution in bulk silicon. The unit of the scale is Kelvin.

Figure 3-29 presents the evolutions of laser intensity and electron number density at the center of the domain 0.25 μm below surface. The laser intensity increases rapidly and begins to decrease before the peak of the incident beam hits the surface. As mentioned above, this seems a result of the complex diffraction of laser induced field in the domain comparable to the wavelength. Although generation of free electron is a function of the laser intensity, the electron number density does not follow the trend of the laser intensity. This is partially because recombination is not considered in the ionization model.

Figure 3-30 presents time histories of electric conductivity, electron temperature, and lattice temperature at the center of the domain 0.25 μm below surface. The electric conductivity is a function of both electron number density and electron temperature, and thus its trend reflects both effects. Electron temperature closely follows the laser intensity due to its small heat capacity. The electron temperature rises more than 20000 K, but the increase of lattice temperature is only 150 K for the same period. This is because the heat capacity of lattice is much larger than that of electron and thus the response is very slow. The heating rate of electrons is extremely higher than that of lattice, and thus electrons alone can reach an ablation point under intense femtoseocnd pulse while the lattice remains cold. Much longer simulation is required to reach the thermal equilibrium between electron and lattice.

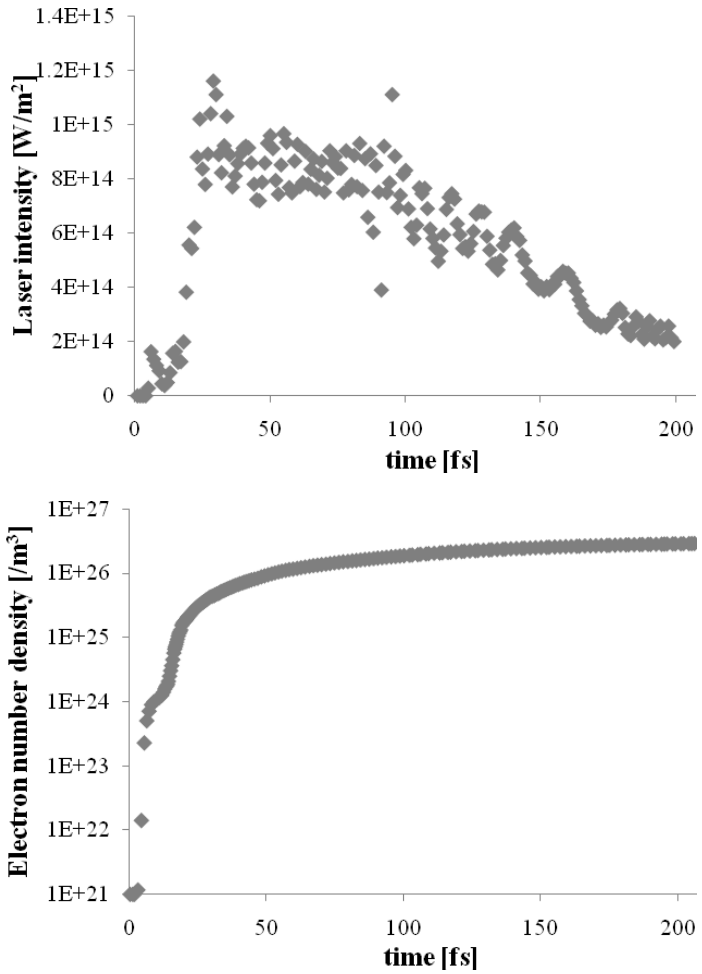

Figure 3-29: Time histories of laser intensity and electron number density at the center of the domain 0.25 μm below surface.

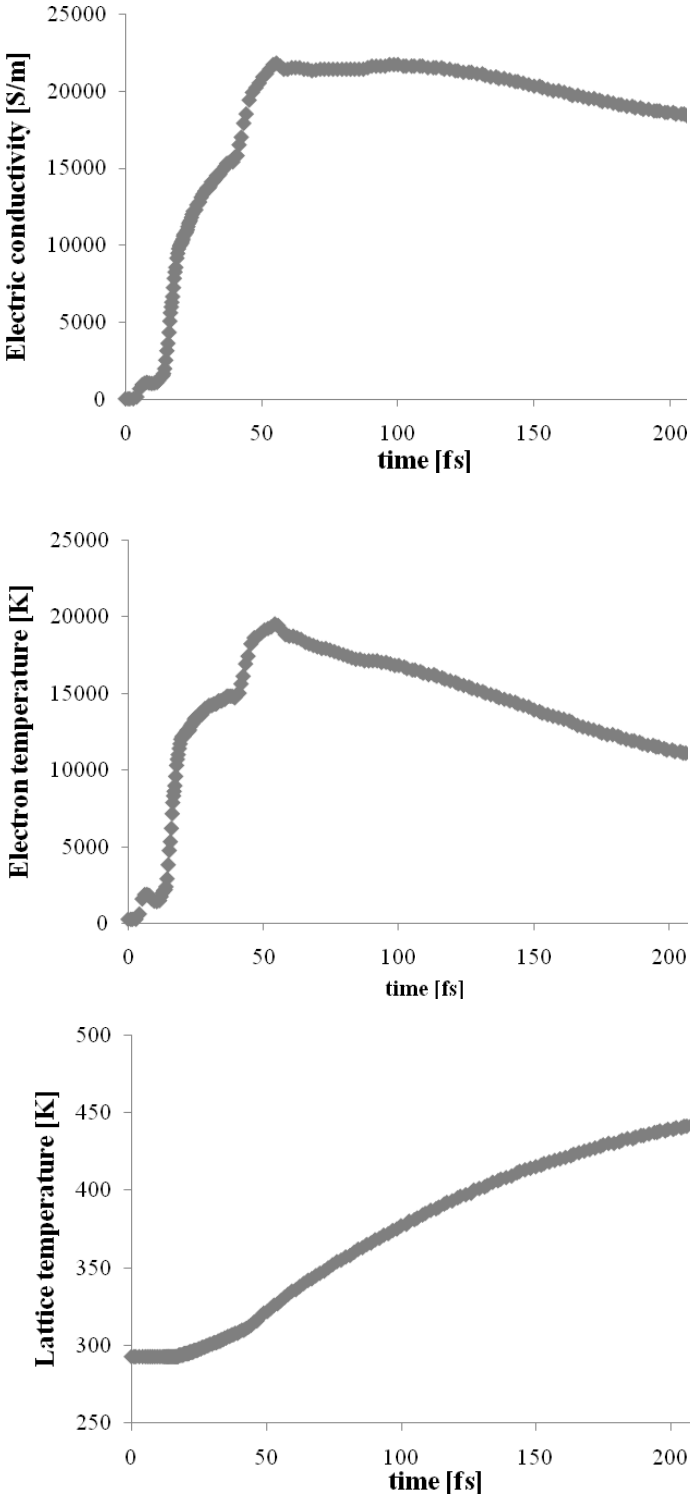

Figure 3-30: Time histories of electric conductivity, electron temperature and lattice temperature at the center of the domain 0.25 μm below surface.

3.6 CONCLUSIONS

Femtosecond ablation of microchannels into silicon is studied to develop branching networks designed to serve oxygenators for use in artificial lungs. Wide range of microchannel size with quality surface is required to realize artificial vascular network. In development of such devices, the processing speed is also a significant consideration. The expansion of machining range with quality surface and the increase of processing speed in a big part relies on the appropriate choice of the scan speed. Utilizing a high repetition of 200 kHz with 10μJ pulse energy, the channel depth varies from 20 to several hundreds of micron with the appropriate choice of the scan speed. The scan speed range providing an effective material removal also creates smooth ablation surface. A 9-level microchannel network is realized as a demonstration. Then, an actual branching channel network (oxygenator) is constructed in PDMS using the laser machined silicon structures as a mold. With 20 s acid etching as a post-processing, the average surface roughness (Ra) of the femtosecond machined channel is less than 2 μm for more than 200 μm depth.

The numerical modeling of femtosecond interaction with silicon shows electron temperature closely follows the laser intensity due to its small heat capacity. But the response of the lattice temperature is very slow compared with the electron temperature. Thus, the heating rate of electrons is extremely higher than that of lattice, and thus electrons alone can reach an ablation point under intense femtoseocnd pulse while the lattice remains cold. As a result, thermal damage is minimized.

CHAPTER IV

BLOOD FLOW IN THE BRANCHING NETWORKS

4.1 INTRODUCTION

The blood flow and the oxygen transfer in the microchannel networks are characterized with both experiments and numerical simulations. Pressure drop and gas exchange in the networks are measured by Cook et al. in Department of Surgery & Biomedical Engineering, University of Michigan and the results are presented in chapter 4.3. The numerical simulations are focused on the demonstration of the benefit of Murray's law applied to blood oxygenators. One purpose of the simulation is to analyze the wall shear stress distribution throughout the branching network which is one of significant factors in activating coagulation and inflammatory systems [2]. Shear stress above a threshold value causes adverse blood trauma including cell trauma and too low shear stress activates coagulation and immunologic factors. [2]

In modeling, blood is considered as incompressible viscous fluid governed by the Navier-stokes equations and the continuity equation. The gas transfer in blood flow is described by the species conservation equation. The shear thinning non-Newtonian characteristic of the blood viscosity is taken into account in the modeling. In the species conservation, the amount of oxygen bound to hemoglobin as a function of oxygen partial

pressure is derived from the oxygen-hemoglobin dissociation curve.

4.2 FABRICATION OF ACTUAL CHANNELS OUT OF PDMS

Actual branching networks are created out of PolyDiMethylSiloxane (PDMS) using the laser machined silicon structures as molds. Figure 4-1 illustrates the molding process. To copy PolyDiMethylSiloxane (PDMS) structures from the laser machined silicon master, Sylgard 184 pre-polymer base and Sylgard 184 curing agent are mixed at a 10:1 ratio in weight. The mixture is put into a vacuum chamber for 3 hours to remove air bubbles generated in the mixing. The surface of the master mold is silanized in a vacuum chamber before pouring the PDMS pre-polymer liquid to release PDMS structures. The air removed PDMS pre-polymer is poured onto the silanized silicon mold and then cured for 3 hrs at 60 □. Then, the cured PDMS replica mold is peeled off from the silicon master mold. To get the same positive pattern on PDMS as the silicon master mold, the negative patterned PDMS replica is used as a mold. In making a positive PDMS replica from the negative PDMS mold, the procedure to make the PDMS replica from the silicon structure is repeated. That is, an opposite patterned PDMS mold is prepared to copy final PDMS structures with the same pattern with laser machined silicon masters as shown in figure 4-2. A 40 μm thick PDMS film is placed on top of the PDMS network to make a closed channel. They are plasma oxidized to be bonded and to make the PDMS channel surface hydrophilic. Blood flows inside the channels and gas exchanges through the gas permeable PDMS film.

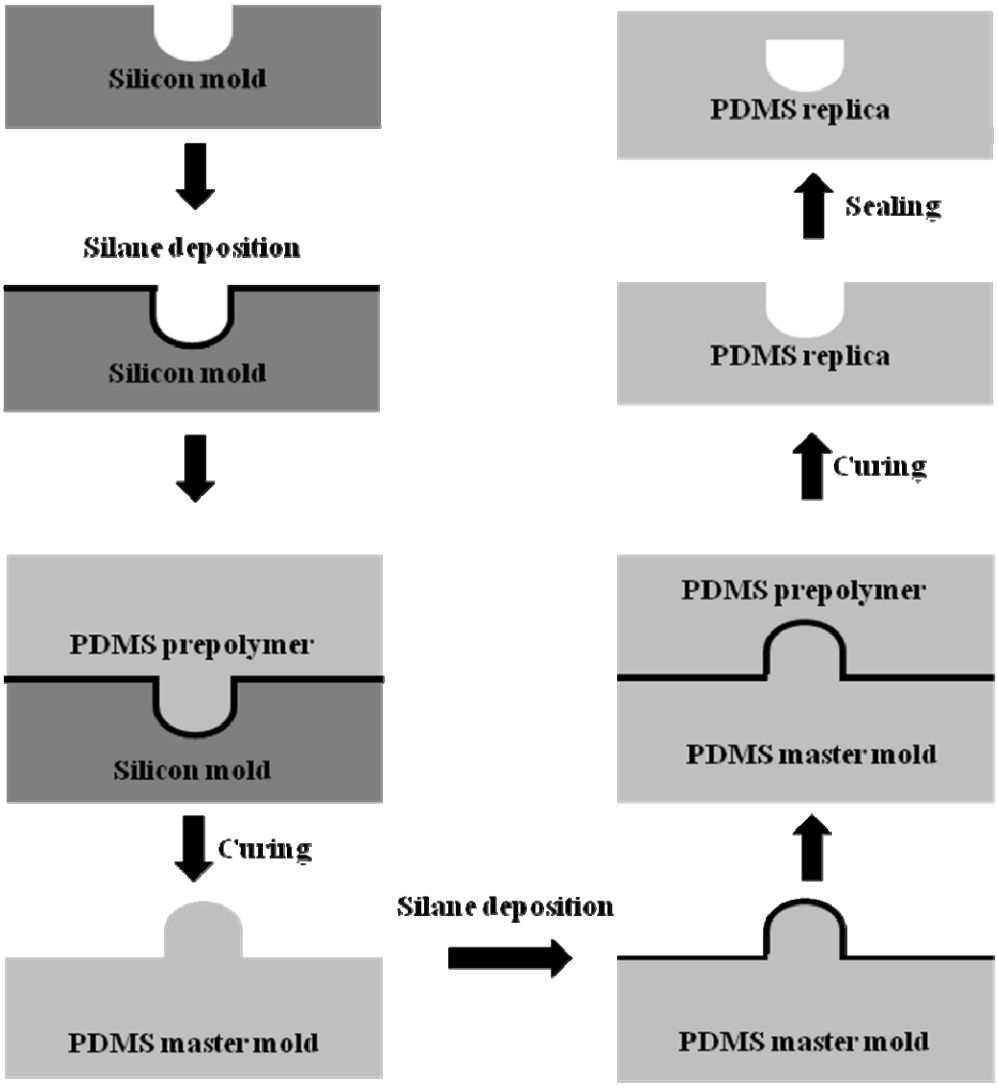

Figure 4-1: Schematic representation of PDMS molding and bonding process

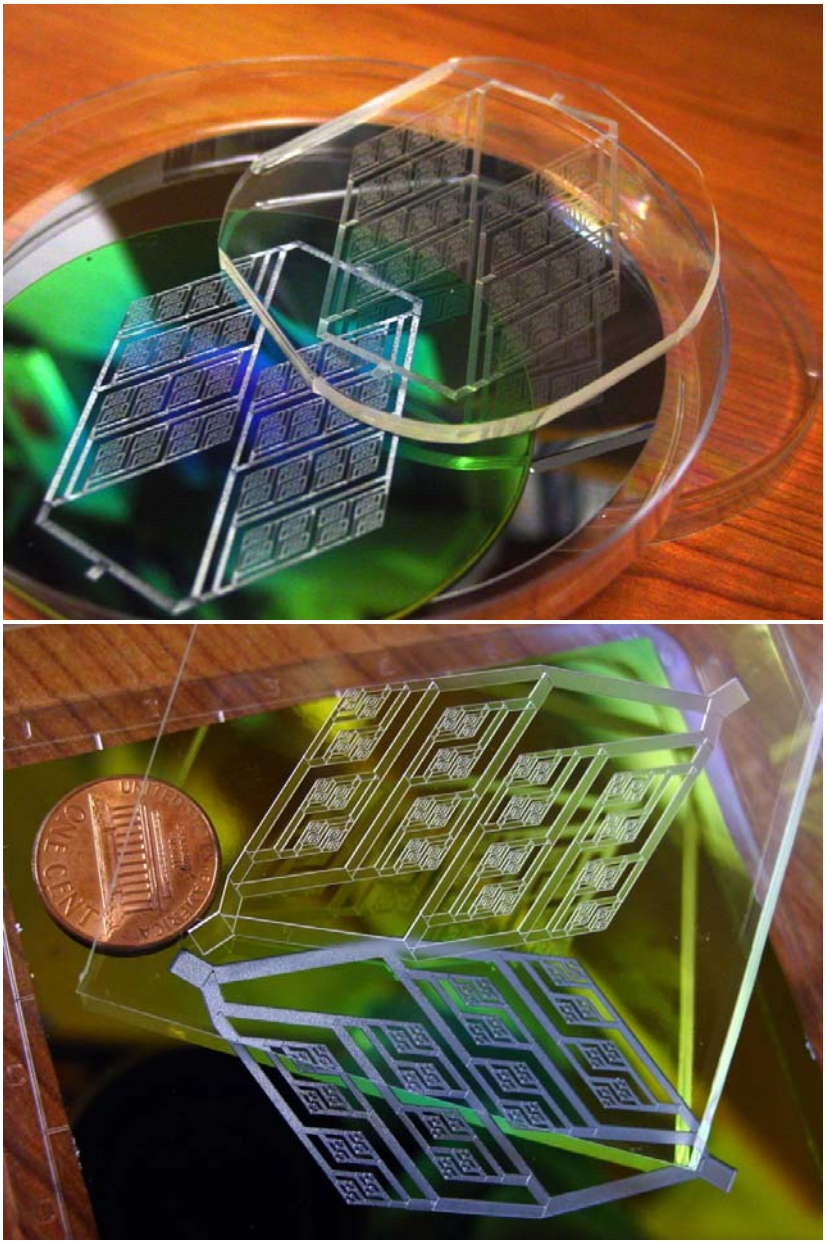

Figure 4-2: Laser machined silicon masters and their PDMS replica. (Top) nanosecond machined 11-level branching network. (Bottom) femtosecond machined 9-level branching network.

4.3 CHARACTERIZATION OF CHANNEL NETWORKS

In vitro blood flow / oxygen transfer in microchannel branching networks are tested by Cook et al. in Department of Surgery and Biomedical Engineering, University of Michigan, to evaluate performance of microchannels. The 9-level and 11-level branching networks were used in the in vitro test as shown in figure 4-3. Ovine blood heparinized and warmed to 37 °C was used in the test, which was carried out in an oven set at 37 °C. The experimental result is summarized in table 4-1.

Table 4-1: Blood flow and gas exchange in 9- and 11-level networks. Averaged hemoglobin concentration, H_{cr}, average flow rate, Q, pressure drop, ΔP , O_2 partial pressure, PO_2 and CO_2 partial pressure, PCO_2.

	9-level		11-level	
	Inlet	Outlet	Inlet	Outlet
H_{cr} (g/dl)	10.1	-	10.1	-
pH	7.4	-	7.4	-
Q (ml/hr)	100		100	
ΔP (mmHg)	34		5	
PO_2 (mmHg)	30-35	102	30-40	323
PCO_2 (mmHg)	40-45	35.7	40-45	33.7

The 9- and 11-level networks with the surface areas of 26.5 and 30 cm^2 have the minimum channel depths of 50 and 20 μm respectively. Across the flow geometry, the 11-level network provides greater gas transfer even with less pressure drop. Therefore, it can be concluded that, the 11-level network is more efficient than the 9-level network. It is also observed that increase of the flow rate results in decrease of the gas transfer and increase of the pressure drop. As for the gas transfer, the residence time of blood in the

manifold increases with decreasing flow rate. The dependence of the pressure drop on the flow rate can be explained by the shear thinning characteristic of blood. As the flow rate increases, the shear rate increases resulting in decrease of blood viscosity.

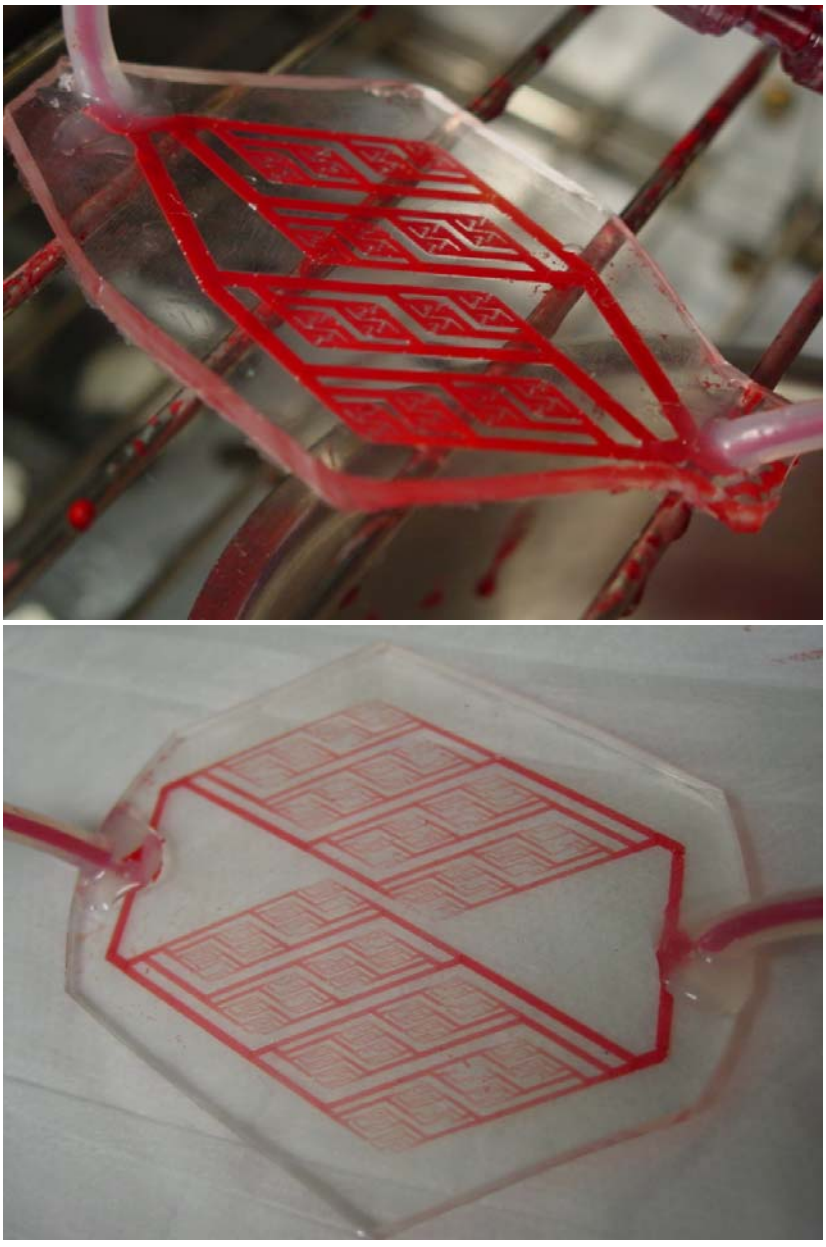

Figure 4-3: Blood flows in 9-level (top) and 11-level (bottom) branching networks.

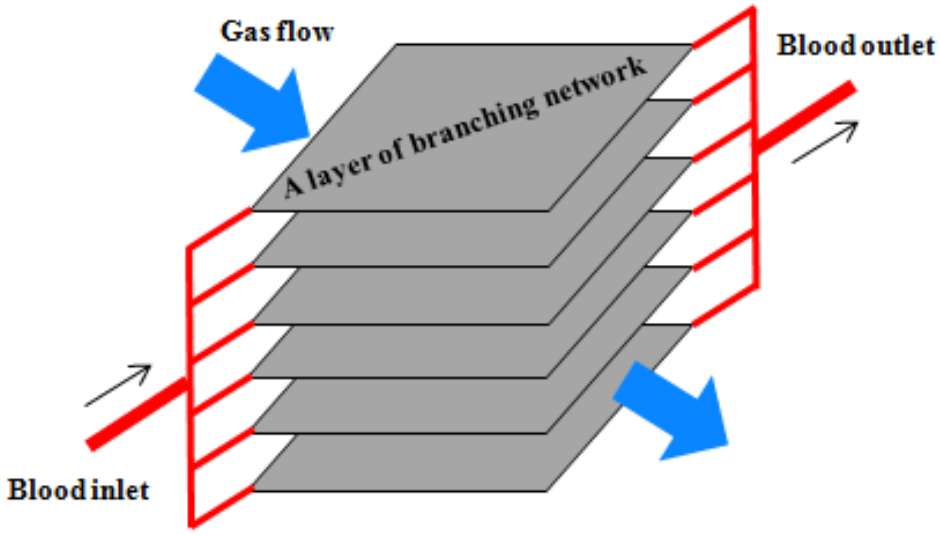

Figure 4-4: Stack network layers as parallel connections. Gap between layers are for ventilation.

Gas exchangers for use in artificial lungs compose of these microchannel branching networks instead of the hollow fiber membrane presented in figure 1-1. The layers of microchannel branching network will be stacked as parallel connections to increase flow rate and gas exchange without increasing pressure drop as shown in figure 4-4. A lumped model, which is derived from electrical circuit analogy, will be used to represent blood flow and pressure drop in these stacked networks. From this blood flow circuit analysis, performance of the gas exchanger can be estimated. In other words, design of such gas exchangers is simplified into that of the microchannel branching network. Therefore, it is essential to characterize and optimize the design of the microchannel network.

4.4 MODELING OF BLOOD FLOW AND GAS EXCHANGE IN A MICROCHANNEL NETWORK

Numerical simulation is carried out to figure out blood flow pattern, shear stress distribution, and blood oxygenation, which are not obtained in the vitro test. The

simulation considers a 4-level branching network composed of rectangular cross-sections. Figure 4-5 illustrates the top view of the network. The network bifurcates according to Murray's law and thus the channels become shallower and narrower at each bifurcation: the channel depths are 40, 32, 25 and 20 μm with constant depth to width ratio of 1:10. The network is sealed with the gas permeable PDMS membrane. Figure 4-6 illustrates a microchannel which is a branch of the network. Blood flows in the microchannel and oxygen transfers through the thin PDMS membrane.

Steady state simulations of blood flow and oxygen transfer are carried out using a commercially available computational package, FLUENT 6.3. The software is based on the finite volume method. Geometries and meshes are created using GAMBIT software.

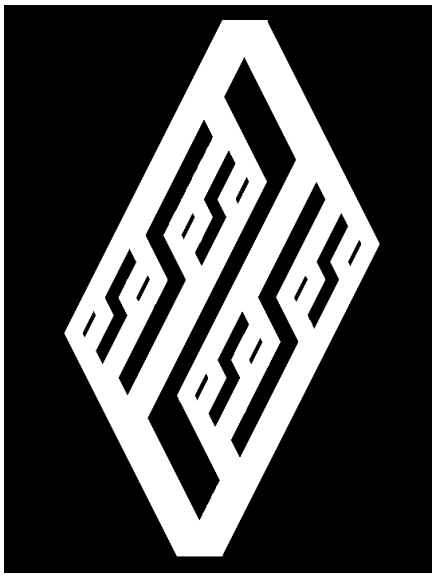

Figure 4-5: Top view of 4-level network with multi-depth (20, 25, 32, and 40 μm)

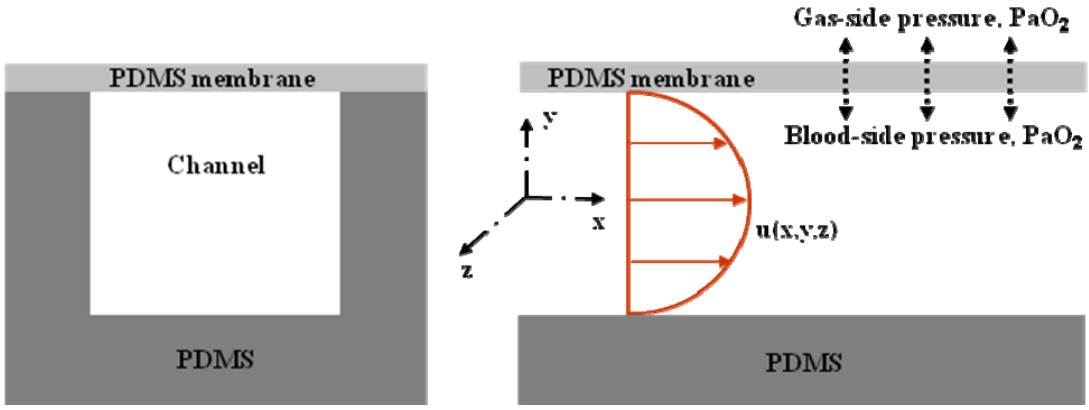

Figure 4-6: (Left) Cross-sectional view of a microchnnel. (Right) Side view of blood flow and gas transfer in the microchannel. Gas exchange occurs through the thin PDMS membrane

4.4.1 Governing equations and boundary conditions

Blood is a heterogeneous fluid consisting of different cells suspended in plasma. Most of the blood cells are red blood cells with a diameter of 6-8 μm and a thickness of 2 μm thickness [74]. Although the cell size is comparable to the minimum channel depth, 20 μm, the blood is treated as a homogeneous continuum to reduce the complexity of modeling.

Blood is assumed to be incompressible viscous fluid governed by mass and momentum conservations. Such flow of blood can be described by Navier-Stokes equations and continuity equation given in equations (4-1) and (4-2) respectively

$$\rho\left(\frac{\partial \bar{u}}{\partial t} + \bar{u}\cdot\nabla\bar{u}\right) = \rho\bar{g} + \nabla\cdot\tau_{ij} \qquad (4-1)$$

$$\nabla\cdot\bar{u} = 0 \qquad (4-2)$$

where $\bar{u}$ is the velocity vector, $\bar{g}$ the vector acceleration of gravity, τ_{ij} the stress tensor, and ρ the density. It is assumed that oxygen is conserved and the oxygen transfer does not affect the blood flow. Then the gas transfer in blood flow can be described by the species conservation equation

$$\frac{\partial C_{O2}}{\partial t} + \bar{u} \cdot \nabla C_{O2} = \nabla \cdot \left(D_{O2} \nabla C_{O2} \right) + R \qquad (4 - 4)$$

where C_{O2} and D_{O2} are the concentration and the diffusion coefficient of oxygen in the blood and R is a source term.

The boundary conditions (BCs) are assumed as follows:

- Inlet of the network is assumed to have uniform velocity profile: for the steady pressure-driven laminar flow in microchannels, the hydrodynamic entry length is very short (~0.05h·*Re* [**75**]), so the effect of inlet velocity profile is negligible.
- Outlet is held at zero gauge pressure.
- No-slip conditions are imposed for surfaces.
- The gas permeable membrane is assumed to have constant oxygen concentration: in membrane oxygenators, oxygen transfer is known to be blood-phase limited because membrane resistance is negligible compared to blood-phase resistance, and thus it is typically assumed that the membrane is infinitely permeable [**25, 76, 77**].
- Mass flux of oxygen is negligible for surfaces but the gas permeable membrane.

4.4.2 Viscosity of blood

Blood is characterized (or behaves) as a shear thinning non-Newtonian fluid. Such nature of blood viscosity is mainly caused by the shear dependent behavior of red blood cells [78, 79]. Various models for non-Newtonian behavior of blood have been proposed to simulate the dependence of the blood viscosity on the shear rate [80, 81]. While showing a similar trend of viscosity dependence on shear rate, such models have different magnitudes of viscosity at low shear rate. Being obtained from curve fitting of experimental data for blood viscosity with shear rate, it is difficult for the model to reflect all the effects of many other parameters such as hematocrit, temperature, and sex. That is, no model is universally accepted. In the present study, blood viscosity is described by Carreau model because of its availability in Fluent. The Carreau model for blood viscosity [82], μ, is given as

$$\mu = \mu_\infty + (\mu_0 - \mu_\infty)[1 + (\lambda\dot{\gamma})^2]^{(n-1)/2} \qquad (4-5)$$

where $\lambda = 3.313\ s$, $n = 0.3568$, $\mu_0 = 0.056\ kg/m-s$ and $\mu_\infty = 0.00345\ kg/m-s$

4.4.3 Oxygen binding

The concentration of oxygen in blood is defined by

$$C_{O2} = \alpha PO_2 \qquad (4-6)$$

where α denotes the solubility of oxygen in blood plasma, and PO_2 is the oxygen partial pressure. The species conservation equation in equation (4-4) is rewritten in terms

of PO_2 as:

$$\frac{\partial(\alpha PO_2)}{\partial t} + \overline{u} \cdot \nabla(\alpha PO_2) = \nabla \cdot [D_{O2} \nabla(\alpha PO_2)] + R \qquad (4-7)$$

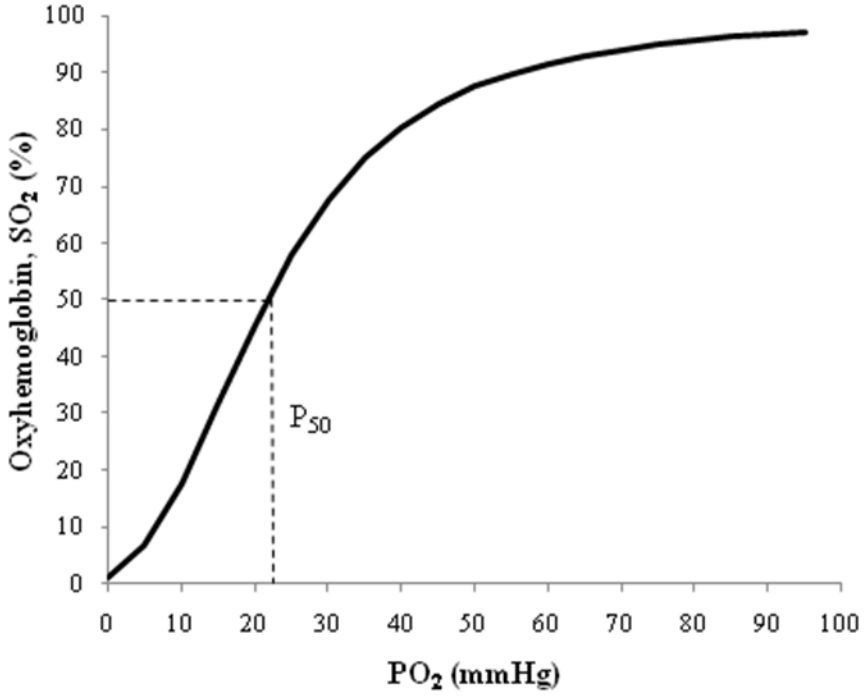

Figure 4-7: the oxygen-hemoglobin dissociation curve.

The source term R represents the rate of oxygen bound to hemoglobin in red blood cells. This term (actually sink) can be derived from the oxygen saturation, SO_2 as follows [76]

$$R = -\frac{D(cSO_2)}{Dt} = -\frac{\partial(cSO_2)}{\partial t} - \overline{u} \cdot \nabla(cSO_2) \qquad (4-8)$$

$$c = H_a H_{cr} / \alpha \qquad (4-9)$$

Here, c is a proportionality constant to convert the percentage of the oxygen saturation to the oxygen partial pressure and H_a denotes the hemoglobin affinity for oxygen. Oxygen-hemoglobin binding is assumed to be fast enough so that oxygen transfer between hemoglobin and surrounding plasma is in near equilibrium. The relation between the oxygen saturation, SO_2, in the red blood cells and PO_2 is plotted as the oxygen-hemoglobin dissociation curve as shown in figure 4-7. And the curve is mathematically expressed with the form of Hill equation [83]

$$SO_2 = \left(\frac{PO_2}{P_{50}}\right)^n \Bigg/ \left[1 + \left(\frac{PO_2}{P_{50}}\right)^n\right] \qquad (4-10)$$

Here the Hill coefficient, n, is 2.7 [81] and 50 % saturating oxygen partial pressure, P_{50}, is 26.6 for human [85] and 30.4 for bovine [76]. For steady state, using equation (4-10) the sink is expressed in terms of PO_2 gradient

$$R = -\bar{u} \cdot \nabla(cSO_2) = -\bar{u} \cdot \left(c \frac{\partial SO_2}{\partial PO_2}\right) \nabla PO_2 \qquad (4-11)$$

$$\frac{\partial SO_2}{\partial PO_2} = \frac{n}{P_{50}} \left(\frac{PO_2}{P_{50}}\right)^{n-1} \left[1 + \left(\frac{PO_2}{P_{50}}\right)^n\right]^{-2} \qquad (4-12)$$

So, steady state oxygen partial pressure distribution in the manifold can be obtained by solving the following species conservation equation

$$\alpha\bar{u}\cdot\nabla PO_2 = \alpha\nabla\cdot\left(D_{O2}\nabla PO_2\right) - c\bar{u}\cdot\left(\frac{\partial SO_2}{\partial PO_2}\right)\nabla PO_2 \qquad (4-13)$$

The sink term is introduced using User Defined Functions (UDF) in Fluent in the form of C code.

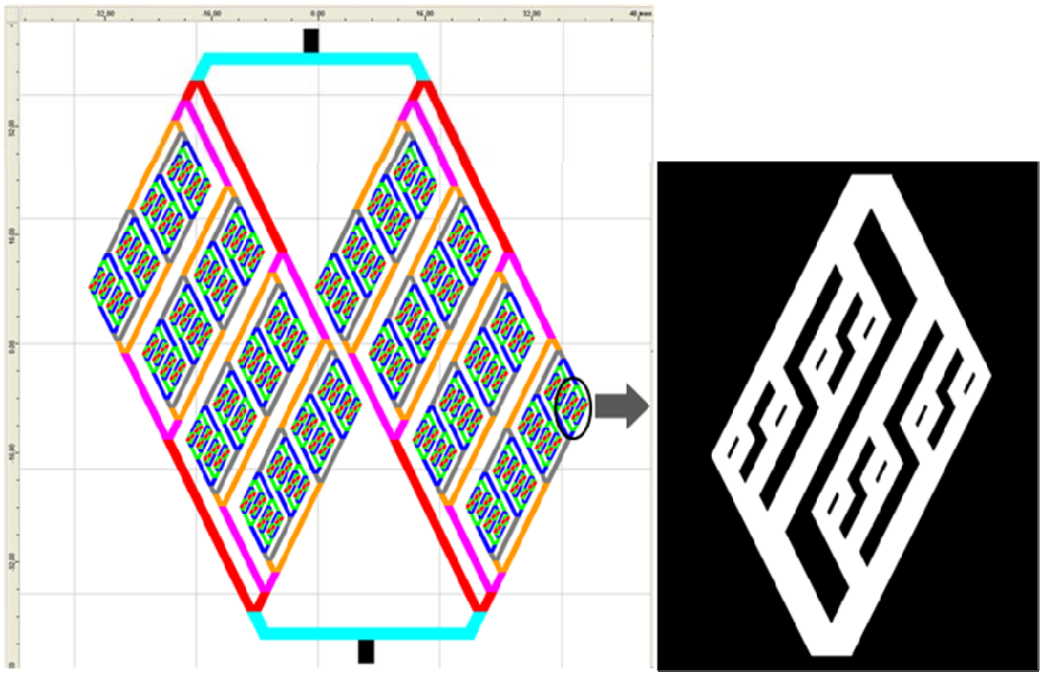

Figure 4-8: (Left) Top view of 11-level multi-depth network with depths ranging from 20 to 200 µm. (Right) Top view of 4-level network corresponding to 8th - 11th generations of the 11-level branching network. The depths of the 4-level network are 20, 25, 32, and 40 µm

4.4.4 Numerical vs. experimental

The 4-level multi-depth network considered in the simulation corresponds to 8th–11th

segment of the 11-level network as shown in figure 4-8. In the vitro experiment conducted by Cook et al., the blood flow rate through the 11-level network is set to 100 ml/hr: the flow rate could not be increased more than 100 ml/hr because of the leakage which is due to high pressure. The corresponding flow rate through the 8^{th}–11^{th} segment is 100/64 ml/hr because the blood flow is evenly distributed to 64 of the segments in the 11-level network. In other words, 100/64 ml/hr for the 4-level network is equivalent to 100 ml/hr for the 11-level network. So, the flow rate of 100/64 ml/hr is simulated for the 4-level network.

Table 4-2: Blood parameters

Parameter	Description	Value
α	Solubility of oxygen in blood plasma	3.14×10^{-5} /mmHg
H_a	Hemoglobin affinity for oxygen	1.36 ml/g
H_{cr}	Hemoglobin concentration in blood	0.101 g/ml
D_{O2}	Diffusion coefficient of oxygen	1.7×10^{-5} cm^2/s
ρ	Blood density	1050 kg/ m^3

As illustrated in figure 4-6, oxygen transfers through the gas permeable PDMS membrane driven by the oxygen partial pressure difference between the gas-side and the blood-side. In the experiment, pure oxygen gas is used as a sweep gas, such that gas-side oxygen partial pressure (PO_2) is more than the partial pressure of atmospheric oxygen gas (~150 mmHg). Membrane resistance to O_2 transfer is known to be negligible compared to blood-phase resistance. As a result, the membrane is assumed to have a constant oxygen concentration in the simulation. Here, PO_2 on the membrane is set to 100 mmHg because blood is fully saturated with oxygen at 100 mmHg PO_2 as presented in figure 4-7.

Approximately 60 % inlet oxygen saturation of blood is used in the blood flow test in the 11-level manifold. In the simulation, however, the inlet oxygen saturation for the 4-level network is assumed to be zero to simplify the analysis because it is prohibitively difficult to find out the actual inlet saturation into the 8^{th}-11^{th} segment.

Blood at 37 °C is modeled with properties given in table 4-3.

Table 4-3: Comparison between the experiment and the simulation

	11-level (experiment)	4-level (simulation)
Flow rate, Q (ml/hr)	100	100/64
Pressure drop, ΔP (Pa)	667	3504
Oxygen transfer, ΔPO_2 (mmHg)	283-293	93

Table 4-3 summarizes the comparison between the experiment with 11-level network and the simulation with the 4-level network. The pressure drop through the 4-level network is very high compared with that of the 11-level network. Considering relative size of the 4-level network over the 11-level network, the pressure drop in the simulation is much higher than that through the 8^{th}-11^{th} segment in experiment. This discrepancy is in part because the pliancy of the PDMS membrane is not considered in the simulation. In the experiment, the membrane is very thin (~40 μm) and thus very flexible, so that the channels become swollen under the given flow condition. Therefore, real channel has less pressure drop than the predicted in the simulation. Other possible reason is that pulsate flow of blood in the experiment is assumed as a steady flow in the simulation. In combination with such periodic pressure variation, the pliancy of the PDMS can allow more flow rate under a certain pressure drop. For flow rate of 100/64

ml/hr, the 4-level network itself shows sufficient oxygen transfer. In the experiment of the 11-level network, the oxygen transfer is more than enough i.e. the outlet oxygen partial pressure is about 323 mmHg: the design goal is about 100 mmHg (equivalent to 97.5 % saturation in figure 4-7). Thus the numerical analysis is in agreement with the experiment showing high saturation results. Thus it is predicted that increase in flow rate is possible to provide even more oxygen exchange.

4.4.5 Multi-depth vs. uniform depth

In order to demonstrate the benefit of multi-depth branching structures designed using Murray's law, the 4-level multi-depth network is compared with 4-level uniform depth networks. Simulations consider three different 4-level branching networks which have the same top-view dimensions as shown in figure 4-5. One manifold is corresponding to 8^{th} - 11^{th} generations of the 11-level branching network with multi-depth (20, 25, 32 and 40 μm) and other manifolds have uniform depths of 20 and 40 μm. Two flow rates ($Q_2 = 10Q_1 = 100/64\, ml/hr$) are simulated for the three networks. The flow rate, Q_2, has the same value as that used in the experiment. Other conditions and properties are set identical to those used in Chapter 4.4.4.

The simulation of the blood flow and the oxygen transfer for the three geometries shows the pressure drop, ΔP, and the oxygen partial pressure increase, ΔPO_2, across the geometries as presented in Table 4-4. The multi-depth manifold has about 4 times less flow resistance than 20 μm depth manifold and about 2 times more flow resistance than 40 μm depth manifold. Figure 4-9 shows the top-view contour plots for the pressure distribution with the flow rate of Q_1 for two 4-level networks: the multi-depth (top) and

the 20 μm-depth networks (bottom). Similar pressure distribution patterns with larger magnitudes are observed with the flow rate of Q_2. The 40 μm-depth networks (not shown) has the same pattern of the pressure contour as that of 20 μm-depth networks, while its magnitude is smaller that of 20 μm-depth networks.

Table 4-4: Simulation results on pressure drop, ΔP , and oxygen partial pressure increase, ΔPO_2 , for two different flow rates, $Q_1 = 0.156\ ml/hr$ and $Q_2 = 10Q_1$

Depth	ΔP (Pa)		ΔPO_2 $(mmHg)$	
	Q_1	Q_2	Q_1	Q_2
Multiple	421	3504	100	93
20 μm	1552	13993	100	97
40 μm	236	1881	100	86

The average velocity contours for two 4-level networks with multiple-depth (top) and the 20 μm-depth (bottom) are shown in figure 4-10. While decreasing with branching down in the constant-depth geometry, the blood velocity distribution is fairly even throughout the multi-depth network. In these symmetric systems, the flow rate halves at each bifurcation implying that the average velocity is determined by the selection of cross-section area of each segment. So, microchannel cross-section areas of the multi-depth network are designed to have the same velocity obeying Murray's law.

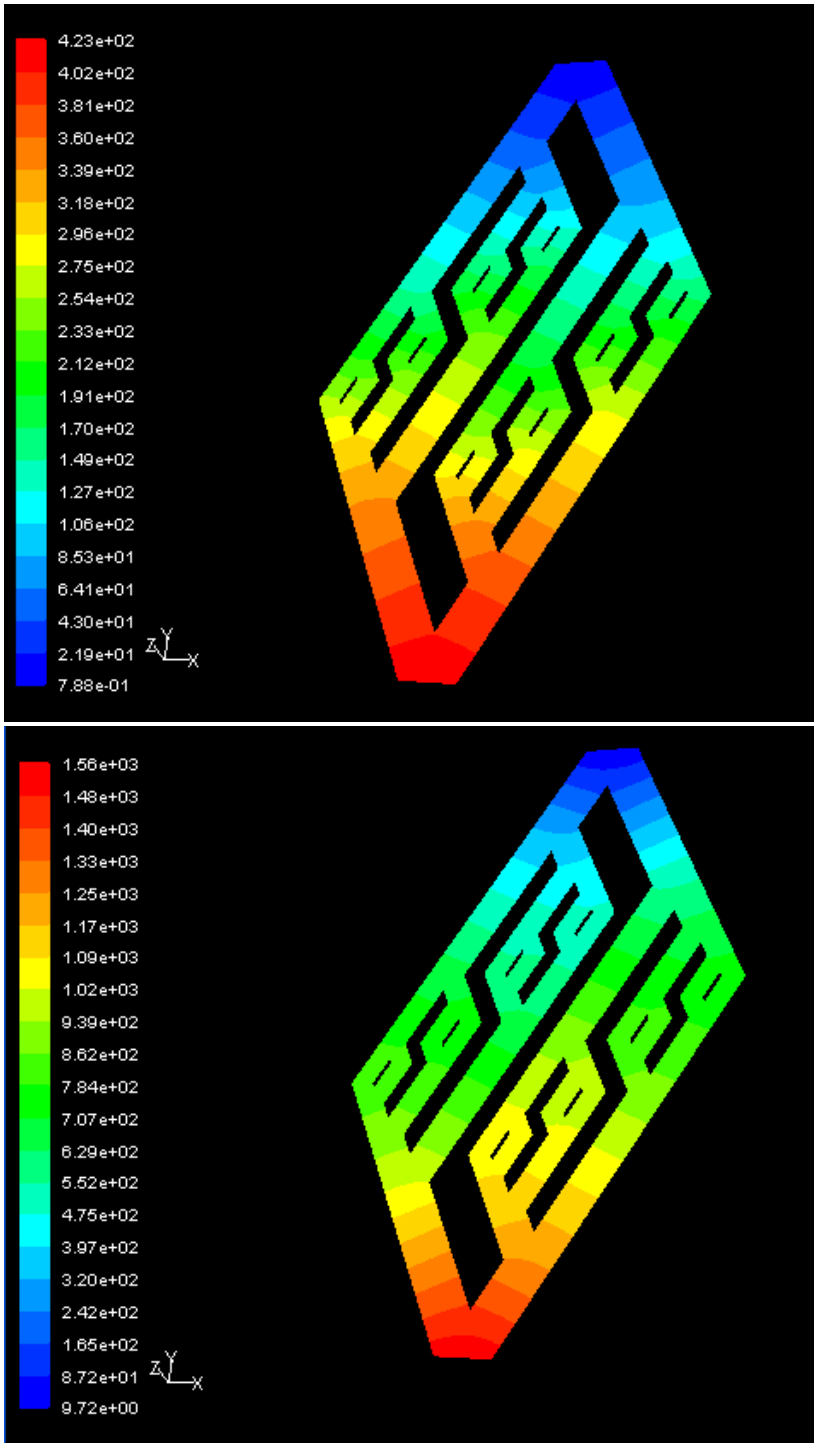

Figure 4-9: Pressure distributions of (top) multiple-depth and (bottom) 20 µm depth networks. Unit of the scale is Pa

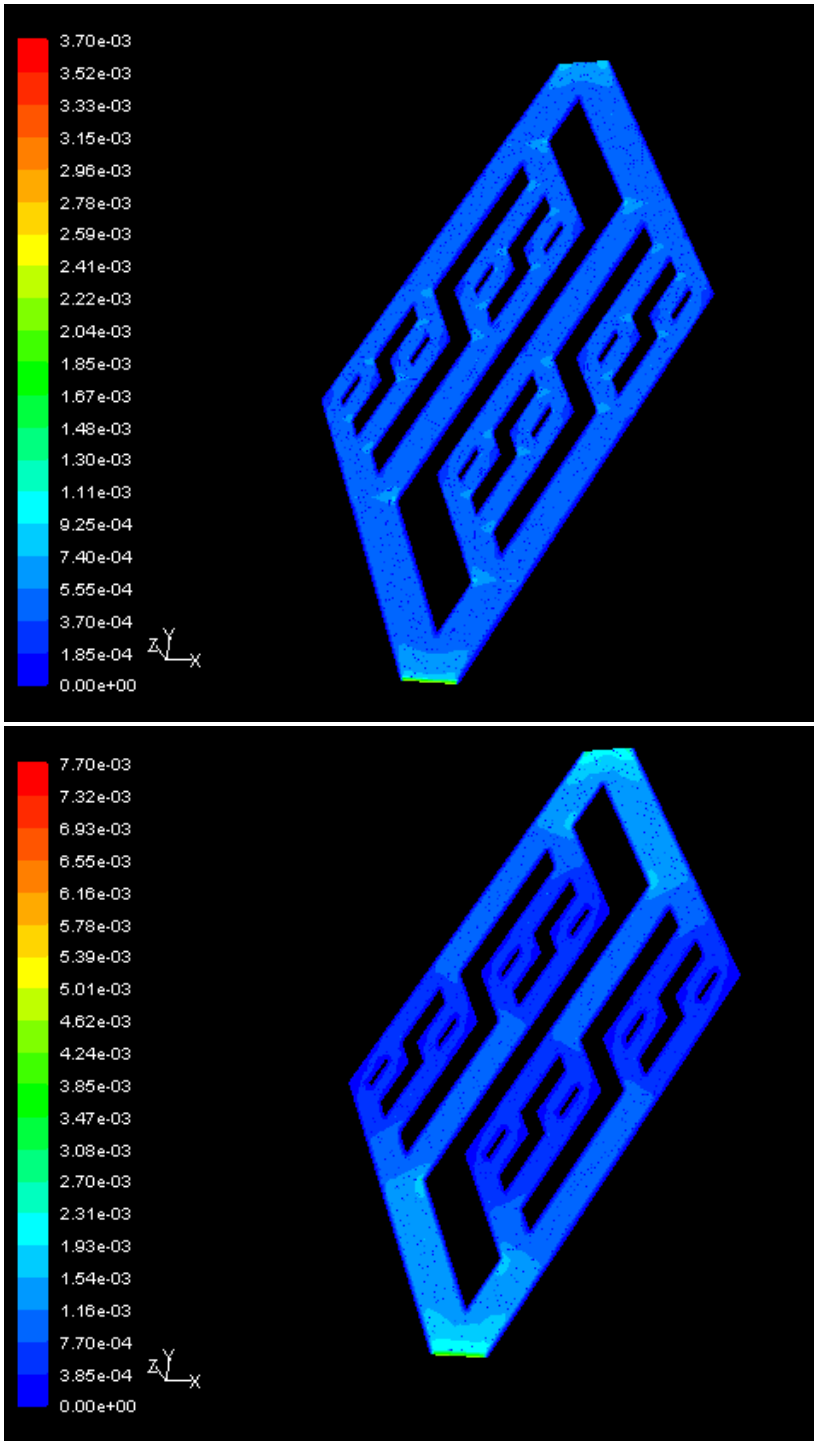

Figure 4-10: Velocity distributions of (top) multiple-depth and (bottom) 20 µm depth networks. Unit of the scale is m/s

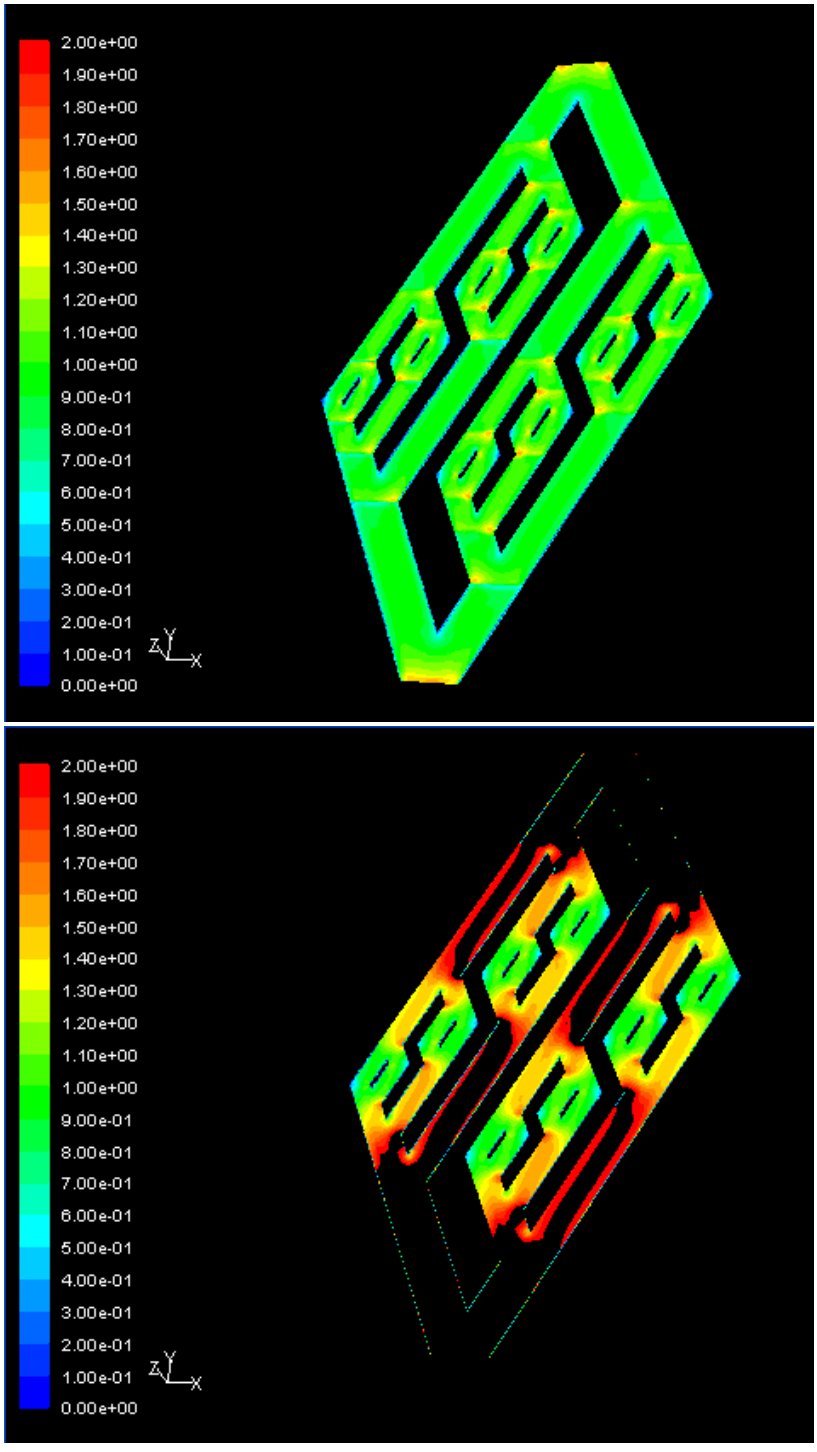

Figure 4-11: Wall shear stress distributions of (top) multiple-depth and (bottom) 20 μm depth networks. Unit of the scale is Pa

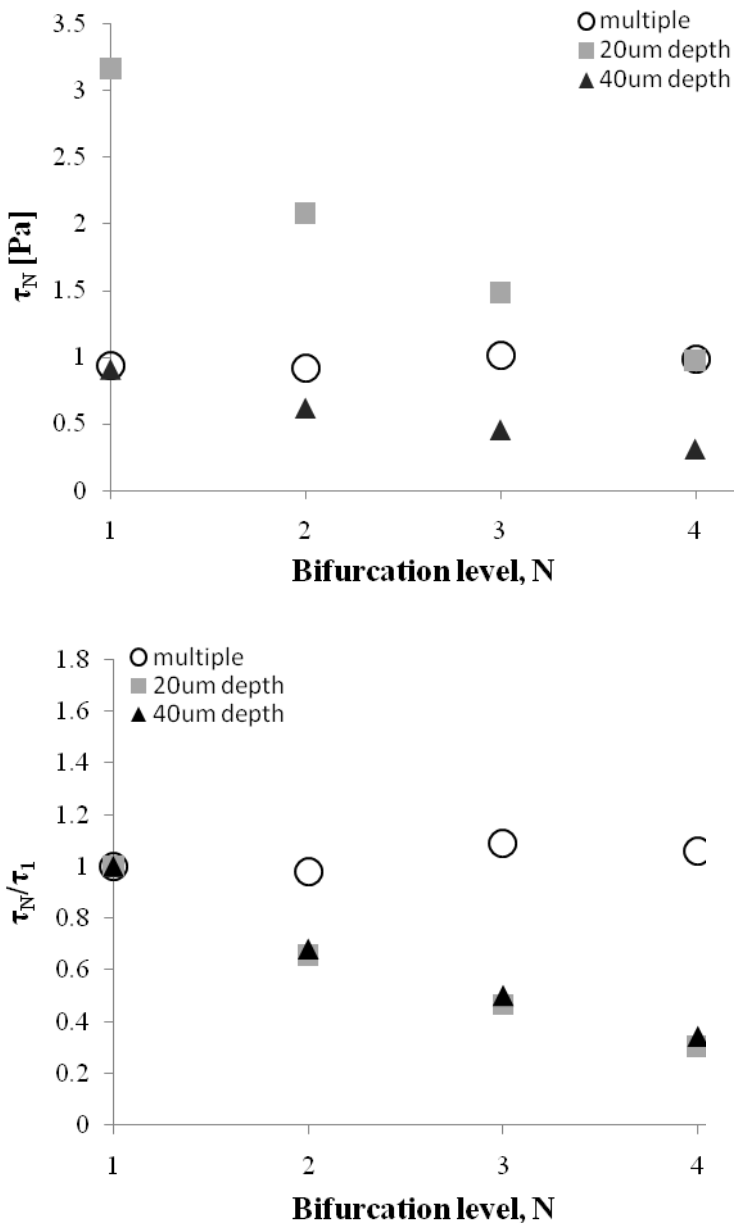

Figure 4-12: Average (top) and normalized average (bottom) wall shear stress distributions as a function of bifurcation level, N for branching networks with multiple, 20 and 40 μm depths

The wall shear stress distributions in two 4-level networks with multiple-depth (top) and the 20 μm-depth (bottom) are illustrated in figure 4-11. As expected, wall shear stress is uniformly distributed throughout the multiple-depth branching networks designed

using Murray's law. In contrast, the distribution in the constant-depth network has relatively considerable variation in each successive generation. In figure 4-12, the wall shear stress, τ_N, and the normalized wall shear stress, τ_N / τ_1, are plotted in terms of bifurcation level, N, where τ_N is a averaged value over the wall of the N^{th} generation. For the multiple-depth structure following Murray's law, the shear stress at each generation remains pretty much constant. For the constant-depth structures, however, the shear stresses decrease in each successive generation because the average velocity decreases at each bifurcation as illustrated in figure 4-10 (bottom). And the normalized averaged wall shear stresses for constant-depth manifolds – 20 and 40 μm depth – have the same trend with the bifurcation level. The 4^{th} generations of the 20 μm-depth and multiple-depth networks have the same shear distribution and the 1^{st} generations of the 40 μm-depth and multiple-depth networks have the same shear distribution. This is expected because the fluid flow behavior is determined by the cross-section area and the flow rate if other parameters are same.

The uniform shear stress distribution created in multi-depth microchannel networks designed using Murray's law facilitates to predict and to control the shear stress at each generation in such networks. Once the dimension of a channel of such branching network is optimized to create physiological blood flow behavior, the dimensions of other channels are found using the Murray's law.

4.4.6 Discussions

Table 4-5 compares the performance of 11-level network with basal respiratory requirement for a person in resting. The metabolic requirement at rest is known as ~5

L/min of blood flow rate and ~250 ml/min of oxygen transfer rate with the pressure drop of less than around 15 mmHg. Assuming the network layers are stacked as parallel connections as shown in figure 4-4, about 3000 of 11-level branching networks are estimated to be required in order to provide ~5 L/min blood flow with the pressure drop of 5 mmHg. Considering the thickness of the network layer and ventilation between each layer, the height for 3000 of the layers is approximated to 1.5 m with 4 inch cross section. But, there is more room to increase the flow rate, so that the size can be decreased. For instance, the flow rate can be increased because the oxygen is over saturated to 323 mmHg PO_2 across the network and the pressure drop is less than the requirement with the current flow rate of 1.67 ml/min (or 100 ml/hr): if we can use three times the flow rate than the current value, then the resulting height of the stack would be one thirds.

Table 4-5: Comparison between the respiratory requirement at rest and the in vitro test with the 11-level network

	Requirement (at rest)	11-level (in vitro)
Flow rate (ml/min)	> 5000	1.67
Pressure drop (mmHg)	< 15	5
Resistance (mmHg-min/ml)	~0.0016	2.99
Output PO_2 (mmHg)	~100	323

In design of the networks consisting of microchannels as blood oxygenators, it is necessary to control the shear stress within a certain range because blood cells are damaged or activated if the shear stress is either too high or too low. To minimize the blood damage and activation in blood oxygenators, the shear stresses should be between 0.4 – 0.8 Pa [2]. The simulation in Chapter 4.4.5 estimates that the average wall shear

stress in the 11-level network is about 8 Pa for the flow rate of 1.67 ml/min (or 100 ml/hr). So, the current flow rate used in the experiment creates too high of a shear stress increasing the risk of blood cell trauma [2, 25]. When the flow rate of 0.167 ml/min (or 10 ml/hr) is modeled, the averaged wall shear stress becomes about 1 Pa. In this case, however, blood is more saturated with oxygen than the current over saturation. So, the flow rate of 0.167 ml/min provides less efficient gas transfer although it creates better shear stress distribution. In other words, for the current design of the 11-level network, the flow rate has to be increased in terms of oxygen transfer, but the flow rate must be decreased to maintain the optimal range of the shear stress. While creating even distribution of blood flow, current design of the 11-level network has a lot room to be improved in terms of the shear stress and the gas exchange. A suggestion to achieve the optimal shear stress and the maximum oxygen transfer is to reduce the number of generations and to increase the minimal depth of the network. Reducing the number of generations decreases the residence time resulting in reduction of oxygen saturation. And the shear stress decreases with increasing the minimal depth of the network (dimensions of all other channels can be found using Murray's law). For example, 11-level network with ~80 μm minimal depth creates ~0.6 Pa shear stress with 100 ml/hr flow rate. For the same flow rate, however, the residence time increases with increasing depth. Thus, the number of generations of the network needs to be decreased to have appropriate oxygen saturation in outlet.

4.5 SUMMARY

The procedure to create actual microchannels out of PDMS using the laser machined silicon is described. In vitro blood flow / oxygen transfer in microchannel branching networks are tested. Both 9- and 11-level networks fully saturate blood with oxygen for the flow rate of 100 ml/hr. The simulation of blood flow and gas exchange in microchannels shows that the multi-depth branching structure following Murray's law creates physiological blood flow: uniform velocity and shear stress distribution. Thus, it is very easy to control the shear stress within a certain range, which minimizes adverse influence of the shear stress on blood cells. For the current design of the 11-level network, the flow rate has to be increased in terms of oxygen transfer, but the flow rate must be decreased to maintain the optimal range of the shear stress. Hence, the minimal depth of the network need to be increased and the number of generations of the network needs to be decreased to have appropriate oxygen saturation in outlet.

CHAPTER V

CONTRIBUTIONS AND FUTURE WORK

5.1 CONTRIBUTIONS

More than 35 million Americans are suffering from chronic lung disease and approximately 400,000 Americans die from lung disease every year [86]. Chronic obstructive pulmonary disease (COPD) is the 4th leading cause of death in US: 118,171 American died in 2004 [86]. Lung cancer is the leading cause of cancer-related deaths: more than 160,000 American died in 2005 [86]. In the short term, the artificial lungs may provide a bridge to recovery or a rescue therapy to the patients with reversible acute lung failures. In the long term, they may serve as a bridge to lung transplantation for the patients with end-stage lung disease.

The lung-like features are essential to the design of an artificial lung to enhance the gas exchange performance while maintaining the blood flow condition biocompatible. However, no proper technology has been available to mimic the features of the natural lung. In this study, the method of fabricating multi-depth microchannel networks with the laser direct writing followed by acid etching is developed: the method provides the ability to mimic the features of the natural vasculatures. The utility of the laser technique as a tool for rapid prototyping of artificial vasculatures is demonstrated by fabricating unprecedented multi-depth branching structures, which replicate the flow of blood in

natural vasculature to serve as oxygenators for artificial lungs. This unique attempt offers potential in further development of artificial lungs creating efficient gas exchange and biocompatible blood flow condition in the blood oxygenator.

In addition to the artificial lung development, the simplicity and flexibility of the laser technique is beneficial to the developments of MEMS, lab-on-a-chip systems, and other biotechnology applications. The maskless laser process will reduce time and cost compared to the conventional photolithography based technique in the device development. The capability of the laser technique to fabricate three-dimensional multi-level structures offers more design options than conventional microfabrications such as photolithography and etching.

The nanosecond and femtosecond pulses have been employed successfully in the laser process by optimizing processing conditions. It has been challenging for the nanosecond ablation to be used in micromachining due to the surface roughness caused by thermal effects including melting, boiling, and fracture. This study shows that optimal combinations of processing parameters can minimize the surface roughness while channel depth is varied. The low productivity of femtosecond pulses compared with related costs has limited its contribution in practical applications. In this study, the optimized conditions reduce the processing time, expand the machining range, and improve the surface quality. A numerical modeling of the femtosecond pulse interaction with silicon has provided understanding of the non-thermal process of femtosecond ablation. The knowledge of the processing physics is also applicable in fabrication of other materials including glasses, metals, ceramics and bio-compatible polymers. However, appropriate choice of laser source and calibration of the parameters are

necessary depending on the materials to be fabricated.

Therefore, the laser technique developed in this study provides the ability to mimic the feature of the natural vasculature in development of artificial lungs. The physiological features are expected to contribute to further development of artificial lungs.

5.2 RECOMMENDATIONS FOR FUTURE WORKS

The multi-depth network designed using Murray's law shows better balance between the pressure drop and the gas exchange with uniform flow distribution than uniform depth structures. However, the current design of the microchannel network needs to be modified to increase oxygen transfer and to create an adequate range of shear stress. For the geometric optimization, a series of numerical modeling and experiments need to be repeated in an iterative way until a desirable performance is obtained.

The long-term performance of blood oxygenators has been limited by the failure of device due to blood clotting or clogging. This problem attributes to the biocompatibility of the device. The biocompatibility is a complex problem that involves many factors including shear stresses, blood flow pattern, composition of the foreign surface, duration of exposure, and surface-to-volume ratio. In this study, however, only the flow pattern and the shear stress are considered and controlled in the design of the microchannel network. Future study on the biocompatibility should be toward mimicking the endothelial cell environment of the blood vessel. The endothelial cells release materials to regulate the activation of platelets and inflammatory systems, induce favorable protein layer to minimize blood damage / thrombosis. Synergetic advances with area of tissue engineering, bioengineering, and biomaterials is required to culture the endothelial cells

on the microchannels. Other approaches are simulating the functions of the endothelial cells engineering the microchannel surface: nitric oxide reduces platelet activation, heparin prevents thrombin formation, and lipid surface minimize damage of proteins and cells in blood.

For numerical modeling of femtosecond pulse interactions with silicon, the current domain size is not big enough to depict realistic behavior of properties, and a current simulation time does not cover the femtosecond pulse duration. These are due to limited CPU and the slow speed of the computation. After upgrading the computer or making a two-dimensional model, simulations for a single femtosecond pulse interaction with silicon can be conducted until the thermal equilibrium is reached. Then, the results of numerical analysis can be compared with experimental results to validate models adopted in the femtosecond ablation mechanism. In order to understand the physical meaning of the processing parameters, such as the scan speed, in the femtosecond ablation, it is necessary to adapt the numerical modeling to simulate multiple pulses. Here, pulse to pulse interval is several orders of magnitude of the thermalization time. Hence, new schemes to cover from femtosecond to microsecond regime must be developed for such numerical modeling.

BIBLIOGRAPHY

[1] OPTN/SRTR 2006 Annual Report

[2] J.B. Zwischenberger, C.M. Anderson, K.E. Cook, S.D. Lick, L.F. Mockros, and R.H. Bartlett, "Development of an Implantable Artificial Lung: Challenges and Progress", ASAIO J., 47, 316-320, 2001

[3] J.B. Zwischenberger and S.K. Alpard, "Artificial lungs: a new inspiration", Perfusion 17, 253-268, 2002

[4] J.W. Haft, B.P. Griffith, R.B. Hirschl, and R.H. Bartlett, "Results of an Artificial-Lung Survey to Lung Transplant Program Directors", J Heart Lung Transplant, 21, 467-473, 2002

[5] G. Matheis, "New technologies for respiratory assist", Perfusion, 18, 245-251, 2003

[6] S. Fischer, A.R. Simon, T. Welte, M.M. Hoeper, A. Meyer, R. Tessmann, B. Gohrbandt, J. Gottlieb, A. Haverich, and M. Strueber, "Bridge to lung transplantation with the novel pumpless interventional lung assist device Novalung", J Thorac Cardiovasc Surg, 131, 719-723, 2006

[7] R. Kopp, R. Dembinski, and R. Kuhlen, "Role of extracorporeal lung assist in the treatment of acute respiratory failure", MINERA ANESTESIOL, 72, 587-595, 2006

[8] M. Iglesias, P. Jungebluth, C. Petit, M.P. Matute, I. Rovira, E. Martinez, M. Catalan, J. Ramirea, and P. Macchiarini, "Extracorporeal lung membrane provides better lung protechtion than conventional treatment for severe postpneumonectomy noncardiogenic acute respiratory distress syndrome", J Thorac Cardiovasc Surg, 135, 1362-1371, 2008

[9] M. Iglesias, E. Martinez, J.R. Badia, and P. Macchiarini, "Extrapulmonary Ventilation for Unresponsive Severe Acute Respiratory Distress Syndrome after Pulmonary Resection", Ann Thorac Surg, 85, 237-244, 2008

[10] B. Kjaergaard, T. Christensen, P.B. Neumann, and B. Nürnberg, "Aero-medical evacuation with interventional lung assist in lung failure patients", Resuscitation, 72, 280-285, 2007

[11] J. McKinlay, G. Chapman, S. Elliot, and A. Mallick, "Pre-emptive Novalung-assist carbon dioxide removal in a patient with chest, head and abdominal injury",

Anaesthesia, 63, 767-770, 2008

[12] T.J. Hewitt, B.G. Hattler, and W.J. Federspiel, “A Mathematical Model of Gas Exchange in an Intravenous Membrane Oxygenator”, Annals of Biomedical Engineering, 26, 166-178, 1998

[13] B.G. Hattler, L.W. Lund, J. Golob, H. Russian, M.F. Lann, T.L. Merrill, B. Frankowski, and W.J. Federspiel, “A respiratory gas exchange cather: In vitro and in vivo tests in large animals”, J Thorac Cardiovasc Surg, 124, 520-530, 2002

[14] H.J. Eash, B.J. Frankowski, K. Litwak, W.R. Wagner, B.G. Hattler, and W.J. Federspiel, “Acute in vivo Testing of a Respiratory Assist Catheter: Implants in Calves Versus Sheep”, ASAIO J., 49(4), 370-377, 2003

[15] T.A. Snyder, H.J. Eash, K.N. Litwak, B.J. Frankowski, B.G. Hattler, W.J. Federspiel, and W.R. Wagner, “Blood Biocompatibility Assessment of an Intravenous Gas Exchange Device”, Artificial Organs, 30(9), 657-664, 2006

[16] W.R. Lynch, J.P. Montoya, D.O. Brant, R.J. Schreiner, M.D. Iannettoni, and R.H. Bartlett, “Hemodynamic Effect of a Low-Resistance Artificial Lung in Series with the Native Lungs of Sheep”, Ann Thorac Surg, 69, 351-356, 2000

[17] J.W. Haft, P. Montoya, O. Alnjjar, S.R. Posner, J.L. Bull, M.D. Iannettoni, R.H. Bartlett, and R.B. Hirschl, “An artificial lung reduces pulmonary impedance and improves right ventricular efficiency in pulmonary hypertension”, J Thorac Cardiovasc Surg, 122, 1094-1100, 2001

[18] S.D. Lick, J.B. Zwischenberger, D. Wang, D.J. Deyo, S.K. Alpard, and S.D. Chambers, “Improved Right Heart Function with a Compliant Inflow Artificial Lung in Series with the Pulmonary Circulation”, Ann Thorac Surg, 72, 899-904, 2001]

[19] S.D. Lick, J.B. Zwischenberger, S.K. Alpard, S.A. Witt, D.M. Deyo, and S.I. Merz, “Development of an Ambulatory Artificial Lung in an Ovine Survival Model”, ASAIO J., 47, 486-491, 2001

[20] J.B. Zwischenberger, D.Wang, S.D. Lick, D.J. Deyo, S.K. Alpard, and S.D. Chambers, “The Paracorporeal Artificial Lung Improves 5-Day Outcomes From Lethal Smoke/Burn-Induced Acute Respiratory Distress Syndrome in Sheep”, Ann Thorac Surg, 74, 1011-1018, 2002

[21] J.W. Haft, O. Alnajjar, J.L. Bull, R.H. Bartlett, and R.B. Hirschl, “Effect of Artificial Lung Compliance on Right Ventricular Load”, ASAIO J., 51, 769-772, 2005

[22] H. Sato, G.W. Griffith, C.M. Hall, J.M. Toomasian, R.B. Hirschl, R.H. Bartlett, and K.E. Cook, “Seven-Day Artificial Lung Testing in an In-Parallel Configuration”, Ann Thorac Surg, 84, 988-994, 2007

[23] H. Sato, C.M. Hall, N.G. Lafayette, J.R. Pohlmann, N. Padiyar, J.M. Toomasian, J.W. Haft, and K.E. Cook, “Thirty-Day In-Parallel Artificial Lung Testing in Sheep”, Ann Thorac Surg, 84, 1136-1143, 2007

[24] W.J. Federspiel and K.A. Henchir, “Lung, Artificial: Basic Principle and Current Applications”, Encyclopedia of Biomaterals and Biomedical Engineering, 910-921, 2004

[25] J.A. Wegner, “Oxygenator Anatomy and Function”, Journal of Cardiothoracic and Vascular Anesthesia, 11(3), 275-281, 1997

[26] C.D. Murray, “The Physiological Principle of Minimum Work Applied to the Angle of Branching of Arteries”, Proc. Nat. Acad. Sc., xii(207) ,835-841, 1926

[27] W. Huang, R.T.Yen, M. McLaurine, and C. Bledsoe,”Morphometry of the Human Pulmonary Vasculature”, J. Appl. Physiol. 81(5), 2123-2133, 1996

[28] S. Kaihara, J. Borenstein, R Koka, S. Lalan, E.R. Ochoa, M. Ravens, H. Pien, B Cunningham, J.P. Vacanti, “Silicon Micromachining to Tissue Engineer Branched Vascular Channels for Liver Fabrication”, Tissue Engineering, 6, 105-117, 2000

[29] J.T. Borenstein, H. Terai, K.R. King, E.J. Weinberg, M.R. Kaazempur-Mofrad, J.P. Vacanti, “Microfabrication Technology for Vascularized Tissue Engineering”, Biomedical Microdevices, 4:3, 167-175, 2002

[30] C. Fidkowski, M.R. Kaazempur-Mofrad, J. Borenstein, J.P. Vacanti, R. Langer, Y. Wang, “Endothelialized Microvasculature Based on a Biodegradable Elastomer”, Tissue Engineering, 11, 302-309, 2005.

[31] C.J. Bettinger, E.J. Weinberg, K.M. Kulig, J.P. Vacanti, Y. Wang, J.T. Borenstein, R. Langer, “Three-Dimensional Microfluidic Tissue-Engineering Scaffolds Using a Flexible Biodegradable Polymer”, Adv. Mater, 18, 165-169, 2006.

[32] J.C. Mcdonald, and G.M. Whitesides, “Poly(dimethylsiloxane) as a Material for fabricating Microfluidic Devices,” Accounts of Chemical Research 35, 491-499, 2002.

[33] S. Dauer, A. Ehlert, and S. Büttgenbach, “Rapid prototyping of micromechanical devices using a Q-switched Nd:YAG laser with optional frequency doubling,” Sensors and Actuators 76, 381-385, 1999

[34] D. Lim, Y. Kamotani, B. Cho, J. Mazumder, and S. Takayama, “Fabrication of microfluidic mixer and artificial vasculatures using a high-brightness diode-pumped Nd:YAG laser direct write method”, Lab Chip 3, 318-323, 2003

[35] N.H. Rizvi, “Femtosecond laser micromachining: Current status and applications,” RIKEN Review 50, 107-112, 2003

[36] D.J. Hwang, T.Y. Choi, and C.P. Grigoropoulos, “Liquid-assisted femtosecond laser drilling of straight and three-dimentional microchannels in glass”, Appl. Phys. A 79, 605-612, 2004

[37] K. Sugioka, M. Masuda, T. Hongo, Y. Cheng, K. Shihoyama, and K. Midorikawa, “Three-dimensional microfluidic structure embedded in photostructurable glass by femtosecond laser for lab-on-chip applications”, Appl. Phys. A 79, 815-817, 2004

[38] M.S. Giridhar, K. Seong, A. Schülzgen, P. Khulbe, N. Peyghambarian, and M. Mansuripur, “Femtosecond pulsed laser micromachining of glass substrates with application to microfluidic devices”, Appl. Optics 43, 4584-4589 (2004).

[39] H. Ho, J.S. Aitchison, S. Eaton, P.R. Herman, and J. Li, “F2-laser microfabrication for integration optical circuits with microfluidic biochips”, in Proceedings of SPIE: Lab-on-a-Chip, Bellingham, Washington, USA, 96-103, 2004

[40] H. Klank, J.P. Kutter, and O. Geschke, “CO2-laser micromachining and back-end processing for rapid production of PMMA-based microfluidic systems”, Lab Chip, 2, 242-246, 2002

[41] B.C. Stuart, M.D. Feit, S. Herman, A.M. Rubenchik, B.W. Shore, and M.D. Perry, “Nanosecond-to-Femtosecond laser-induced breakdown in dielectrics”, Physical Review B, 53(4), 1749-1761, 1996

[42] B.N. Chichkov, C. Momma, S. Nolte, F. von Alvensleben, and A. Tünnermann, “Femtosecond, picoseconds, and nanosecond laser ablation of solids”, Appl Phys A, 63, 109-115, 1996

[43] K. Sugioka, Y. Cheng, and K. Midorikawa, “Three-dimensional micromachining of glass using femtosecond laser for lab-on-a-chip device manufacture”, Appl Phys A, 81, 1-10, 2005

[44] M.S. Amer, M.A. El-Sshry, L.R. Dosser, K.E. Hix, J.F. Maguire, and B. Irwin “Femtosecond versus nanosecond laser machining: comparison of induced stresses and structural changes in silicon wafers,” Applied Surface Science 242, 162-167, 2005.

[45] D.M. Karnakis, G. Rutterford, and M.R.H. Knowles, “High power DPSS laser micromachining of silicon and stainless steel,” in Proceedings of ICALEO, Miami, USA, 2005.

[46] X. Zeng, X. Mao, R. Greif, and R.E. Russo, “Experimental investigation of ablation efficiency and plasma expansion during femtosecond and nanosecond laser ablation of silicon,” Appl. Phys. A 80, 237-241, 2005.

[47] M. Müllenborn, H. Dirac, J.W. Retersen, and S. Bouwstra, “Fast 3D laser micromachining of silicon for micromechanical and microfluidic applications,” in proceedings of Transducers’95 • Eurosensors □, Stockholm, Sweden, 166-169, 1995.

[48] D. von der Linde, K. Sokolowski-Tinten and J. Bialkowski, “Laser-solid interaction in the femtosecond time regime”, Applied Surface Science, 109/110, 1-10, 1997

[49] D.B. Wolfe, J.B. Ashcom, J.C. Hwang, C.B. Schaffer, E. Mazur, and G.M. Whitesides, “Customization of Poly(dimethylsiloxane) Stamps by Micromachining Using a Femtosecond-Pulsed Laser”, Adv. Mater. 2003, 15, No.1, Jan. 3

[50] J.M. Liu, “Simple technique for measurements of pulsed Gaussian-beam spot sizes,” Optics Letters, 47(5), 196-198, 1982

[51] H. Ki and J. Mazumder, “Numerical simulation of femtosecond laser interaction with silicon”, JLA, 17(2), 110-117, 2005

[52] H. Li and H. Ki, “Effect of ionization on femtosecond laser pulse interaction with silicon”, J. App. Phy. 100, 104907, 2006

[53] P.P. Pronko, P.A. VanPompay, R.K. Singh, F.Qian, D. Du and X. Liu, “Laser Induced Avalanche Ionization and Electron-Lattice Heating of Silicon with intense IR Femtosecond Pulses”, Mat. Res. Soc. Symp. Proc. vol. 397, 45-51, 1996

[54] P.P. Pronko, P.A. VanRompay, C. Horvath, F. Loesel, T. Juhasz, X. Liu and G. Mourou, “Avalche ionization and dielectric breakdown in silicon with ultrafast laser pulses”, Phy. Rev. B, 38(5), 2387-2390, 1998

[55] K. Sokolowski-Tinten and D. von der Linde, “Generation of dense electron-hole plasmas in silicon”, Phy. Rev. B, 61(4), 2643-2650, 2000.

[56] D.P. Korfiatis, K.-A. Th. Thoma and J.C. Vardaxoglou, “Numerical modeling of ultrashort-pulse laser ablation of silicon”, Applied Surface Science, 255, 7605-7609, 2009

[57] D.J. Hwang, C.P. Grigoropoulos and T.Y. Choi, “Efficiency of silicon micromachining by femtosecond laser pulses in ambient air”, J. Appl. Phys. 99, 083101, 2006

[58] L. Jiang and H.L. Tsai, “Prediction of crater shape in femtosecond laser ablation of dielectrics”, J. Phys. D: Appl. Phys. 37, 1492-1496, 2004

[59] E.G. Gamely, A.V. Rode and B. Luther-Davies, “Ablation of solids by femtosecond lasers: Ablation mechanism and ablation thresholds for metal and dielectrics”, Phys. Plasmas, 9(3), 949-957, 2002

[60] B. Rethfeld, A. Kaiser, M. Vicanek and G. Simon, “Ultrafast dynamics of nonequilibrium electrons in metals under femtosecond laser irradiation”, Physical Review B, 65, 214303, 2002

[61] P.B. Corkum, F. Brunel, N.K. Sherman and T. Srinivasan-Rao, “Thermal

Response of Metals to Ultrashort-Pulse Laser Excitation", Physical Review Letter, 61(25), 2886-2889, 1988

[62] Z. Lin and L.V. Zhigilei, "Electron-phonon coupling and electron heat capacity of metals under conditions of strong electron-phonon nonequilibrium", Physical Review B, 77, 075133, 2008

[63] J. Hohlfeld, S.-S. Wellershoff, J. Güdde, U. Conrad, V. Jähnke and E. Matthias, "Electron and lattice dynamics following optical excitation of metals", Chemical Physics, 251, 237-258, 2000

[64] S.-S. Wellershoff, J. Hohlfeld, J. Güdde and E. Matthias, "The role of electron-phonon coupling in femtosecond laser damage of metals", Appl. Phys. A, 69, S99-S107, 1999

[65] W. Kütt, A. Esser, K. Seibert, U. Lemmer, and H. Kurz,"Femtosecond studies of plasma formation in crystalline and amorphous silicon", Proc. SPIE 1268, 154–165, 1990.

[66] M.I. Kaganov, I.M. Lifshitz, and L.V. Tanatarov, "Relaxation between electrons and the crystalline lattice", Sov. Phys. JETP, 4, 173-178, 1957

[67] R. Guenther, "Modern Optics", ISBN 0-47-60538-7, 1990

[68] D.K. Cheng, "Field and Wave Electromagnetics 2nd ", ISBN 0-201-12819-5, 1989

[69] C. Tsironis, T. Samaras, "Scattered-Field FDTD Algorithm for Hot Anisotropic Plasma with Application to EC Heating", IEEE Transactions on Antennas and Propagation, 56(9), 2988-2994, 2008

[70] W.A. Challener, I.K. Sendur, and C. Peng, "Scattered field formulation of finite difference time domain for a focused light beam in dense media with lossy materials", Optics Express, 11(23), 3160-3170, 2003

[71] K.S. Kunz and R.J. Luebbers, "The Finite Difference Time Domain Method for Electromagnetics", CRC Press, Boca Raton, 1993

[72] G. Mur, "Absorbing boundary conditions for the finite-difference approximation of the time-domain electromagnetic-field equations", IEEE Tans. Electromag. Compat., 23, 377-382, 1981

[73] R.J. Zollweg and R.W. Liebermann, "Electrical conductivity of nonideal plasmas", J. Appl. Phys. 62(9), 3621-3627, 1987

[74] Hillman, Robert S.; Ault, Kenneth A.; Rinder, Henry M. (2005), "Hematology in Clinical Practice: A Guide to Diagnosis and Management (4 ed.)", McGraw-Hill Professional, p. 1, ISBN 0071440356

[75] F.P. Incropera and D.P. DeWitt, “Introduction to Heat Transfer (3rd)”, WILEY, p.389, ISBN 0-471-30458-1

[76] D.A. Baker, J.E. Holte, and S.V. Patankar, “Computationally two-dimensional finite-difference model for hollow-fiber blood-gas exchange devices”, Med. & Biol. Eng. & Comput., 29, 482-488, 1991

[77] T.I. Marx, W.E. Snyder, A.D. ST. John and C.E. Moeller, “Diffusion of oxygen into a film of whole blood”, J. Appl. Physiol. 15(6), 1123-1129, 1960

[78] Y Liu, W.K. Liu, “Rheology of red blood cell aggregation by computer simulation”, J. of Computational Physics, 220, 139-154, 2006

[79] R.G. Owens, “A new microstructure-based constitutive model for human blood”, J. Non-Newtonian Fluid Mech., 140, 57-70, 2006

[80] B.M. Johnston, P.R. Johnston, S. Corney and D. Kilpatrick, “Non-Newtonian blood flow in human right coronary arteries: steady state simulations”, Journal of Biomechanics, 37, 709-720, 2004

[81] S. O’Callaghan, M. Walsh and T. McGloughlin, “Numerical modeling of Newtonian and non-Newtonian representation of blood in a distal end-to-side vascular bypass graft anastomosis”, Medical Engineering & Physics, 28, 70-74, 2006

[82] Y.I. Cho, K.R. Kensey, “Effects of the non-Newtonian viscosity of blood on flows in a diseased arterial vessel. Part 1. Steady flows”, Biorheology, 28, 241-262, 1991

[83] A.V. Hill, “The possible effects of the aggregation of the molecules of haemoglobin on its dissociation curves”, J. Physiol., 40, 4-7, 1910

[84] A. Zwart, G. Kwant, B. Oesburg, and W.G. Zulstra, “Oxygen dissociation curve for whole blood, recorded with an instrument that continuously measures PO2 and SO2 independently at constant T, PCO2, and pH”, Clin. Chem., 28, 1287-1292, 1982

[85] C. Lenfant, J.D. Torrance and C.A. Finch, “The regulation of hemoglobin affinity for oxygen in man”,Trans. Assn. Amer. Physicians, 85, 121-128, 1969

[86] www.lungusa.org